Additive Manufacturing of Mechanoresponsive Polymers

Bo Cao

A dissertation

submitted in partial fulfillment of the

requirements for the degree of

Doctor of Philosophy

University of Washington

2019

Reading Committee:

Andrew J. Boydston, Chair

Alshakim Nelson

Julia A. Kovacs

Program Authorized to Offer Degree:

Department of Chemistry

University of Washington

Abstract

Additive Manufacturing of Mechanoresponsive Polymers

Bo Cao

Chair of the Supervisory Committee:
Professor Andrew J. Boydston
Department of Chemistry

Polymer mechanochemistry has been investigated for the mechanism of mechanical force-induced chemical reactivity within polymers. Many efforts have been made to fine tune the mechanoresponsiveness of the polymeric materials both in molecular and macroscopic level to broaden the applications of this kind of stimuli-responsive material in engineering field. Additive manufacturing, as an emerging and versatile technology, is widely utilized to create objects with very complex geometries, which makes the study for the effect of geometries on polymer mechanochemistry possible. This dissertation describes the research on additive manufacturing of mechanophore-containing polymers and characterizing the dependence of mechanochemical reactivities of the functional moieties with geometries. Chapter 1 is an introduction to additive manufacturing, polymer mechanochemistry, and the precedent work on combining these two fields. The study of Chapter 2 represents our work on additive manufacturing of a “flex-activated” mechanophore, oxanorbornadiene, with photocurable resins by using vat photopolymerization

printing. The characterization of the released small molecules after activation and the influence of the printed geometry are also depicted. Chapter 3 focuses on printing with polymers containing mechanochromic mechanophore, spiropyran, into complex geometries. The areas with the highest localized strain in those geometries can be detected easily by the color change. Chapter 4 introduces the fabrication and characterization of mechanochromic elastomeric sheets that enable the real-time, on-site, dynamic mapping of strain field distribution on objects with hierarchical patterns. Chapter 5 discusses the experimental and computational study on achieving the early onset activation of the mechanophore at much lower global strains in comparison with materials lacking judicious geometric design by tuning the microstructural geometry of the periodic mechanoreponsive polymeric materials.

TABLE OF CONTENTS

List of Figures

List of Tables

ACKNOWLEDGEMENTS

First and foremost, I would like to thank my advisor, Dr. AJ Boydston, for his generous help and kind guidance during my graduate school life at University of Washington. Studying aboard as an international student is not always an easy thing, but AJ's incredible support on my research and life makes it an enjoyable and fruitful process. Besides chemistry, he also provided me the opportunities to work on interdisciplinary projects and cooperate with excellent scientists and engineers in other departments or universities. I believe the knowledge, the ways to analyze and solve problems, the approach to collaborate with others, and the presentation skills I learned during my Phd study in US will benefit my whole life.

Also, I would like to thank other group members in Boydston lab. Johanna Schwartz, Carl Thrasher, and Johanna Vandenbrande are all great team players and worked with me to push forward the science behind additive manufacturing. Dr. Chang-Uk Lee, Dr. Derek Church, Dr. Laura Murphy, Pengtao Lu, Tori Kensy, and Brock Lynde also provided me insightful suggestions on my research and liberal encouragements in my daily life.

Additionally, I am indebted to the professors who gave me helpful suggestions and discussions during my exams and on my research projects, including all my committee members, Dr. Alshakim Nelson, Dr. Julie Kovacs, and Dr. Duane Storti. I would also like to thank Dr. Mark Ganter, Dr. Nicholas Boechler (UCSD), and Dr. Stephen Craig (Duke) for their guidance through the years.

Finally, I would like to express my deep gratefulness for the unconditional love and enthusiastic support from my parents. They are always there when I encounter ups and downs in my study and life. None of this would be possible without them.

DEDICATION

To my parents

Chapter 1. Introduction to additive manufacturing and polymer mechanochemistry[1]

1.1 Introduction to additive manufacturing

Additive manufacturing (AM), also called three-dimensional printing (3DP), has been an emerging technology that is continuing making contributions to manufacturing industries. After its first commercialization in 1980s, it has drawn intense interests from industry and academia and significant advances have been made since then.[1] The AM differs from the traditional manufacturing techniques in the way that it fabricates the objects through a build-up, or additive, process in a layer-by-layer fashion. Unlike traditional manufacturing techniques, such as injection molding and machining, no unique tools or molds are required for the fabrication process, which not only enables to ability to directly fabricate an object from a computer-aided design (CAD) file, but also endows the freedom for designing and creating objects with very complex geometries that are not easily realized by conventional techniques, such as hollow structures and lattice frameworks. Importantly, modifications to digital objects are facile and readily translated into iterated manufactured parts through AM which also makes AM a process of "rapid prototyping".[2] After decades of development, AM has been widely applied in numerous filed, including biomedical filed for tissue engineering and patient-specific implants[3,4], automotive manufacturing industry for customized parts and on-demand manufacturing[5], buildings for automated constructions and light-weight structures[6], and so on. The speed, versatility, and capability of

[1] Partially adapted with permission from Boydston, A. J., Cao, B., Nelson, A., Ono, R. J., Saha, A., Schwartz, J. J., & Thrasher, C. J. (2018). Additive manufacturing with stimuli-responsive materials. *Journal of Materials Chemistry A*, 6(42), 20621-20645. Copyright 2018 The Royal Society of Chemistry.

advanced AM techniques have expanded its uses beyond simple prototyping and many consider it "the third industrial revolution"[7].

There are many types of AM which utilize different inputs, such as light, heat, and pressure, to enable the chemical or physical transformation of the material to create objects. The most widely used AM technique is melt material extrusion (MME) (also known as fused deposition modelling, or FDM) 3DP.[8,9] This 3DP process works by heating the thermoplastic filaments above their glass transition temperature (Tg) or melting temperature (Tm) so that the heated material can be extruded through the nozzle in a layer-by-layer fashion. After one layer is deposited, the build plate on the 3D printer is moved upward and deposit another layer. This process is repeated until the desired 3D object is formed. To date, many thermoplastic materials have been developed into MME filaments with different materials properties, including toughness, stiffness, and elasticity, for various applications. Various MME filaments are commercially available, including acrylonitrile butadiene styrene (ABS), high-density polyethylene (HDPE), high impact polystyrene (HIPS), polylactide (PLA), and polycaprolactone (PCL).[10] The most important parameters needed to be adjusted to ensure successful printing during MME printing are the extruder temperature and the print bed temperature. To ensure the thermoplastics are fully molten during the printing process, the extruder temperature should be set well above the Tg or Tm of the filaments. Some filaments experience wrapping issue when deposited onto the build plate or delaminated between different layers upon rapid cooling, leading to the failure of the printing or poor mechanical properties of the printed objects.[11] Therefore, the print bed temperature should also be tuned for different filaments. The easiness of fabrication and non-toxic nature of this printing technique make it consumer-friendly and widely used in both industrial and academic areas.

Another fast-developing AM technology is vat photopolymerization which applies light as a stimulus to trigger the photopolymerization of the liquid resins. The typical composition of the liquid resins is the photoinitiator that generates radicals or photoacids to initiate the reaction, the monomers including acrylates, methylacrylates, acrylamides, epoxides, and the crosslinkers which are bi- or multi- functionalized.[12–14] The printing process works by irradiating light in a pattern-wise manner onto the bottom of a transparent container with photosensitive liquid resins. Polymer networks form in the exposed regions. After one layer is cured, the build plate moves upwards for the distance of layer thickness and cures another layer. The three-dimensional object is formed

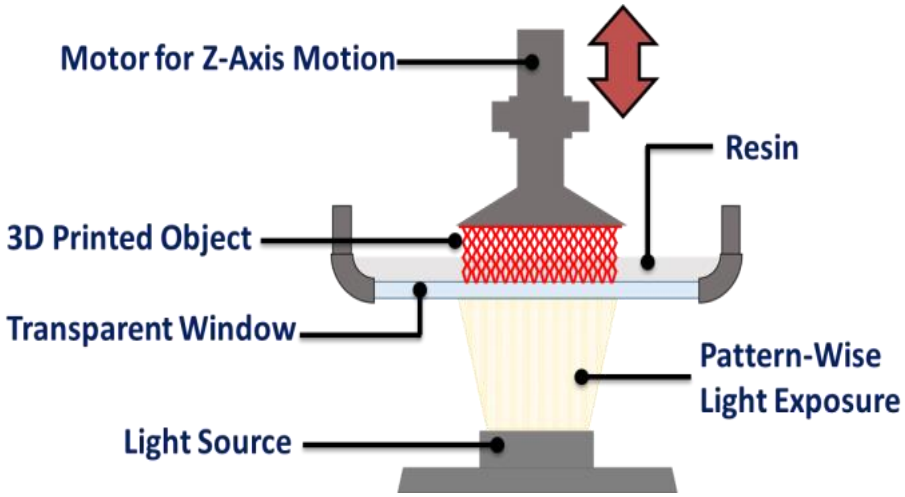

Figure 1.1 Schematic illustration of vat photopolymerization.

layer-by-layer after sequential exposure of the resins to patterned light. The schematic of the vat photopolymerization process is shown in Fig.1.1. This printing technique has the advantages of transferring the liquid monomers directly to solid networks, which is cost efficient compared to the filamentization process in MME printing. Additionally, the liquid form of the monomers provides much more flexibility for incorporating functional molecules and performing chemical modifications to the precursors. Last but not least, this technique is a room temperature process, enabling chemicals that are unstable at high temperatures to be 3D printed.

1.2 Introduction to polymer mechanochemistry

The chain-like structures, formed by connection of chemical bonds, in polymer molecules give polymeric materials special mechanical properties, enabling wide range of applications of these materials. These molecular chains can respond to the external mechanical perturbation applied on polymer materials, resulting in the scission or reconfiguration of the bonds. Polymer mechanochemistry is to investigate the response of the polymer chains to mechanical forces, as well as the mechanism of this behavior. [15] The study of polymer mechanochemistry can be tracked back to 1930s when Staudinger and coworkers found out the reduction of molecular weight of natural rubbers by mastication. [16] In 1980s, Sohma and coworkers confirmed the homolytic bond scission along polymer backbones experimentally.[17] The intuition of polymer mechanochemistry is "destructive", resulting in bond cleavage, degradation of polymer materials or compromising their mechanical properties.[18] However, the discovery of mechanophores successfully transforms polymer mechanochemistry from "destructive" to "productive".[19] Mechanophores are functional chemical moieties that can be embedded into polymer chains and the weak bonds on the mechanophores can be broken in response to external mechanical forces. The force applied on polymeric materials leads to the transduction of macroscopic mechanical force into molecular levels of strain along a segment of a polymer backbone or network. This strain dictates geometric distortions in mechanophore and modifies the potential energy surface to facilitate a chemical reaction. Various mechanism of responsive behavior of mechanophores were studied, including the cleavage of covalent bonds or metal-ligand bonds[20,21], cycloreversion[22], and electrocyclic ring opening[23] (Fig.1.2). Therefore, the mechanophore-containing polymers transforms the mechanical input to outputs in other productive forms, such as color change[24], catalyst generation[25], acid releasing[26], and so on.

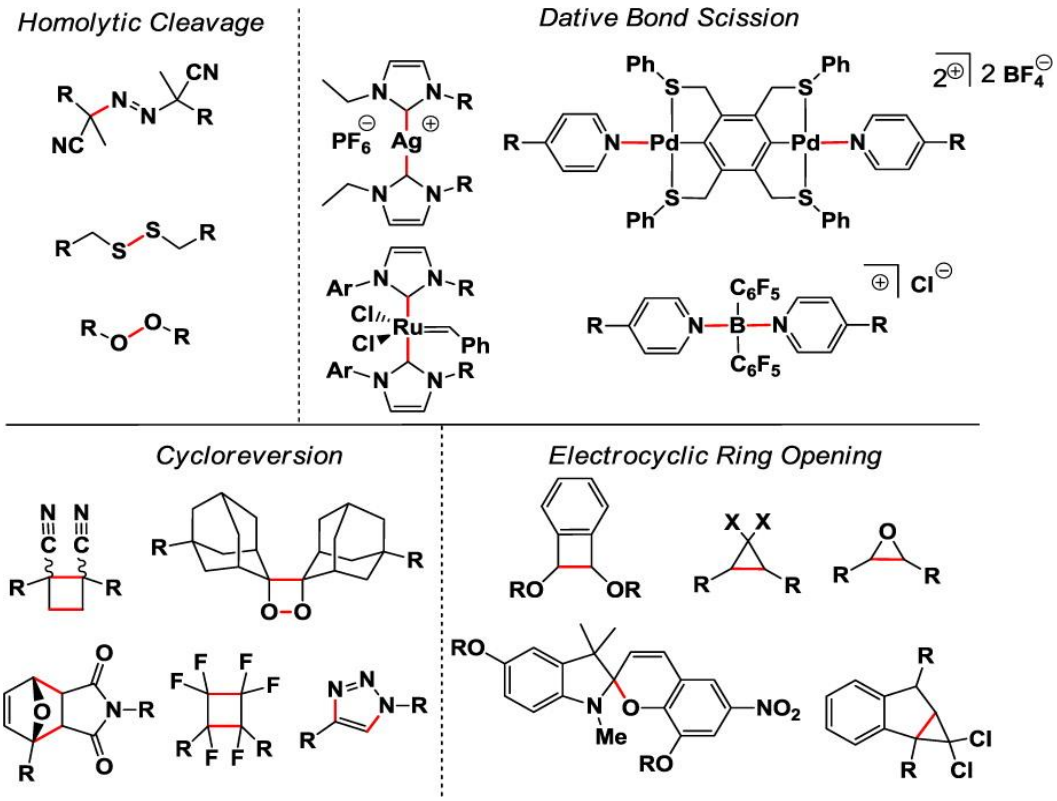

Figure 1.2 Generalized examples of moieties capable of mechanochemical activation, with the scissile bond(s) highlighted in red. R = site of polymer attachment; X = F, Cl. Reprinted with permission ref. 22. Copyright (2013) American Chemical Society.

As a burgeoning field itself, there have been a few examples of integration of mechanochemistry with other disciplines, such as the fast-developing AM technology. Recently, Boydston and co-workers have demonstrated the MME printing of mechanochromic objects.[27] They investigated a 3D printable custom PCL filament that contained mechanochromic spiropyran units in each polymer chain. When printed test specimens were mechanically strained (e.g., through tensile elongation or torsion), the molecular-level response was a force-driven conversion of the spiropyran mechanophores into a highly colored merocyanine isomer. Spiropyran, one of the more academically studied photochromic molecules, is also capable of having a color changing isomerization upon radiation with ultraviolet (UV) light, as well as photo-relaxation with subsequent exposure to visible light or heat. Notably, the custom filament required very little

spiropyran to cause a visible color change upon activation. Specifically, filaments with as little as 0.25 wt % spiropyran (ca. 1 spiropyran unit each, in one-tenth of the polymer chains) was found to give intense color changes in most test specimens. In one demonstration of multimaterial printing, the authors used dual extrusion to fabricate a series of force sensors that contained multiple mechanochromic PCL regions throughout the gauge region of the specimen. These PCL regions could be activated in a predictable fashion, with sequential activation requiring increased peak mechanical load. This work demonstrated that 3D printing custom mechanochromic materials provides an easy way to fabricate prototypes with variable geometries and spatially-defined mechanochromic regions. Interestingly, the modular nature of the spiropyran moiety has enabled dually and selectively responsive systems involving photochromism and the previously described mechanochromism.[27] Printed specimens with segregated photochromic and mechanochromic regions were fabricated by alternating deposition of the two stimuli-responsive materials with a multi-material MME printer. AM provided an easily obtainable and highly customizable way to fabricate photo- and mechano- dual responsive materials that could be selectively activated by UV irradiation in the photochromic regions or mechanical load in the mechanochromic regions, as shown in Figure 1.3. This level of spatial control and rapid prototyping with multi-material compositions would be challenging without integration of the materials with AM technology.

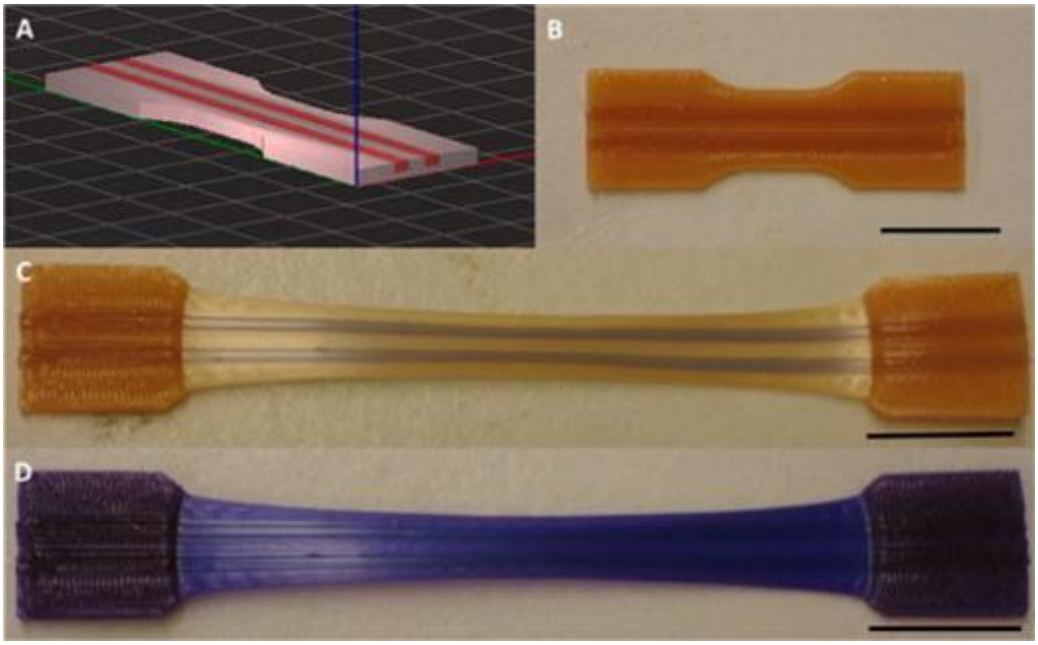

Figure 1.3 (A) CAD representation of a multicomponent tensile test specimen, with red stripes indicating the location of the mechano-responsive filament (specimen body comprised of photochromic filament), (B) test specimen pre-elongation, (C) test specimen postelongation showing the mechanochromic response of the center lines, and (D) test specimen postelongation after 365 nm UV irradiation showing activation of both regions. Scale bars = 20 mm. Reprinted with permission ref. 27. Copyright (2014) American Chemical Society.

This initial report on integrated mechanochemistry and AM highlighted several parameters that may be key to realizing other mechanoresponsive AM build materials. For example, the authors did not observe activation of the spiropyran during extrusion, neither in the filamentation nor printing. Although this would not have been detrimental since the spiropyran activates reversibly, other mechanophores may activate under demanding extrusion conditions. [28] Additionally, the thermal stability of mechanophores must be considered when melt material extrusion is the targeted printing technique. For example, the authors specifically selected PCL for its low processing and printing temperatures. Finally, the high molar absorptivity of the merocyanine form (activated spiropyran) allowed for low (0.25 wt%) concentrations of

mechanophore to be used. This caused essentially no changes in the physical properties of the PCL print material, which is an advantage that may not be enjoyed if higher concentrations of mechanophores are required. That is, printing with non-traditional polymer filaments is expected to require additional optimization. To further explore the interface between polymer mechanochemistry and additive manufacturing, we printed mechanoresponsive polymers by using different AM technologies and characterized the mechanochemical reactivity in both quantitative and qualitative ways. The progress in these fields and the potential applications are discussed herein.

1.3 References

(1) Ford, S. L. N.; Scheme, P.; Team, A. S. D. C.; Details, B.; Investigator, P.; Stratasys Strategic Consulting; Hague, R.; Reeves, P.; Jones, S.; Gao, W.; Zhang, Y.; Ramanujan, D.; Ramani, K.; Chen, Y.; Williams, C. B.; Wang, C. C. L.; Shin, Y. C.; Zhang, S.; Zavattieri, P. D.; Chan, L.-K.; Wu, M.-L.; Bhavar, V.; Kattire, P.; Patil, V.; Khot, S.; Gujar, K.; Singh, R.; European Powder Metallurgy Association; Murugan, S.; Tomlin, M.; Meyer, J.; Manufacturing, A.; Goebner, J.; Mellor, S.; March, E.; Sharma, A.; November, V.; Wohlers, T.; Gornet, T.; Capacity, I.; Geraedts, J.; Doubrovski, E.; Verlinden, J.; Stellingwerff, M.; Pro, C.; Sætre, E.; Gibson, I.; Rosen, D. W.; Stucker, B.; Vayre, B.; Vignat, F.; Villeneuve, F.; Environments, L.; Jiang, R.; Kleer, R.; Piller, F. T.; Li, J.; Wu, B.; Myant, C.; Slotwinski, J. A.; Garboczi, E. J.; Stutzman, P. E.; Ferraris, C. F.; Watson, S. S.; Peltz, M. A.; Linkyo Insights; Foroozmehr, E.; Lin, D.; Kovacevic, R.; AM-Platform; Wang, L.; Alexander, C. A.; Diegel, O.; Dodabalapur, A.; Arias, A. C.; Frisbie, C. D.; Marks, T. J.; Ponfoort, O.; I. Gibson l D. W. Rosen l B. Stucker; Scott, J.; Gupta, N.; Weber, C.; Newsome, S.; Address, O.; Wong, K. V.; Hernandez, A.; Dunbar, N. E.; Segrin, C.; Xinxiong Wang; Tools, O.; Home, S.; East, A.; Huang, Y.; March, M. C. L.; Sutton, A. T.; Kriewall, C. S.; Leu, M. C.; Newkirk, J. W. Additive Manufacturing : Strategic Research Agenda. *AM-Platform* **2014.**

(2) Conner, B. P.; Manogharan, G. P.; Martof, A. N.; Rodomsky, L. M.; Rodomsky, C. M.; Jordan, D. C.; Limperos, J. W. Making Sense of 3-D Printing: Creating a Map of Additive Manufacturing Products and Services. *Addit. Manuf.* **2014**, *1*, 64-76**.**

(3) Ventola, C. L. Medical Applications for 3D Printing: Current and Projected Uses. *Pharmacy and Therapeutics* **2014**, *39*(10), 704.

(4) Ackland, D. C.; Robinson, D.; Redhead, M.; Lee, P. V. S.; Moskaljuk, A.; Dimitroulis, G. A Personalized 3D-Printed Prosthetic Joint Replacement for the Human Temporomandibular Joint: From Implant Design to Implantation. *J. Mech. Behav. Biomed. Mater.* **2017**, *69*, 404-411.

(5) Khajavi, S. H.; Partanen, J.; Holmström, J. Additive Manufacturing in the Spare Parts Supply Chain. *Comput. Ind.* **2014**, *65*(1), 50-63**.**

(6) Labeaga-Martínez, N.; Sanjurjo-Rivo, M.; Díaz-Álvarez, J.; Martínez-Frías, J. Additive Manufacturing for a Moon Village. *Procedia Manuf.* **2017**, *13*, 794-801**.**

(7) Rifkin, J. The Third Industrial Revolution: How the internet, green electricity, and 3-D printing are ushering in a sustainable era of distributed capitalism. *World Financial Review* **2012**, *1*(1), 4052-4057.

(8) Bikas, H.; Stavropoulos, P.; Chryssolouris, G. Additive Manufacturing Methods and Modeling Approaches: A Critical Review. *Int. J. Adv. Manuf. Technol.* **2016**, *83*(1-4), 389-405**.**

(9) Guo, N.; Leu, M. C. Additive Manufacturing: Technology, Applications and Research Needs. *Frontiers of Mechanical Engineering.* **2013**, *8*(3), 215-243**.**

(10) Ligon, S. C.; Liska, R.; Stampfl, J.; Gurr, M.; Mülhaupt, R. Polymers for 3D Printing and

Customized Additive Manufacturing. *Chemical Reviews.* **2017**, *117*(15), 10212-10290**.**

(11) Shaffer, S.; Yang, K.; Vargas, J.; Di Prima, M. A.; Voit, W. On Reducing Anisotropy in 3D Printed Polymers via Ionizing Radiation. *Polymer (Guildf).* **2014**, *55*(23), 5969-5979**.**

(12) Liska, R.; Schuster, M.; Inführ, R.; Turecek, C.; Fritscher, C.; Seidl, B.; Schmidt, V.; Kuna, L.; Haase, A.; Varga, F.; Lichtenegger, H.; Stampfl, J. Photopolymers for Rapid Prototyping. J. *Coatings Technol. Res.* **2007**, *4*(4), 505-510**.**

(13) Stansbury, J. W.; Idacavage, M. J. 3D Printing with Polymers: Challenges among Expanding Options and Opportunities. *Dental Materials* **2016**, *32*(1), 54-64**.**

(14) Hofmann, M. 3D Printing Gets a Boost and Opportunities with Polymer Materials. *ACS Macro Letters.* **2014**, 382-386**.**

(15) Brantley, J. N.; Wiggins, K. M.; Bielawski, C. W. Polymer Mechanochemistry: The Design and Study of Mechanophores. *Polym. Int.* **2013**, *62*(1), 2–12.

(16) Staudinger, H.; Leupold, E. O. Isoprene and Rubber. XVIII. Viscosity Studies on Balata. *Rubber Chem. Technol.* **1930**, *3*(3), 516-518**.**

(17) Sohma, J. Mechanochemistry of Polymers. *Progress in Polymer Science.* **1989**, *14*(4), 451-596**.**

(18) Li, J.; Nagamani, C.; Moore, J. S. Polymer Mechanochemistry: From Destructive to Productive. *Acc. Chem. Res.* **2015**, *48*(8), 2181–2190.

(19) Berkowski, K. L.; Potisek, S. L.; Hickenboth, C. R.; Moore, J. S. Ultrasound-Induced Site-Specific Cleavage of Azo-Functionalized Poly(Ethylene Glycol). *Macromolecules* **2005**, *38*(22), 8975-8978**.**

(20) Encina, M. V.; Lissi, E.; Sarasúa, M.; Gargallo, L.; Radic, D. Ultrasonic Degradation of Polyvinylpyrrolidone: Effect of Peroxide Linkages. *J. Polym. Sci. Polym. Lett. Ed.* **1980**, *18*(12), 757-760**.**

(21) Park, I.; Sheiko, S. S.; Nese, A.; Matyjaszewski, K. Molecular Tensile Testing Machines: Breaking a Specific Covalent Bond by Adsorption-Induced Tension in Brushlike Macromolecules. *Macromolecules* **2009**, *42*(6), 1805-1807.

(22) Larsen, M. B.; Boydston, A. J. "Flex-Activated" Mechanophores: Using Polymer Mechanochemistry to Direct Bond Bending Activation. *J. Am. Chem. Soc.* **2013**, *135*(22), 8189–8192.

(23) Lee, C. K.; Davis, D. A.; White, S. R.; Moore, J. S.; Sottos, N. R.; Braun, P. V. Force-Induced Redistribution of a Chemical Equilibrium. *J. Am. Chem. Soc.* **2010**, *132*(45), 16107-16111**.**

(24) Robb, M. J.; Kim, T. A.; Halmes, A. J.; White, S. R.; Sottos, N. R.; Moore, J. S. Regioisomer-Specific Mechanochromism of Naphthopyran in Polymeric Materials. *J. Am. Chem. Soc.* **2016**, *138*(38), 12328–12331.

(25) Tennyson, A. G.; Wiggins, K. M.; Bielawski, C. W. Mechanical Activation of Catalysts for C-C Bond Forming and Anionic Polymerization Reactions from a Single Macromolecular

Reagent. *J. Am. Chem. Soc.* **2010**, *132*(46), 16631-16636.

(26) Diesendruck, C. E.; Steinberg, B. D.; Sugai, N.; Silberstein, M. N.; Sottos, N. R.; White, S. R.; Braun, P. V.; Moore, J. S. Proton-Coupled Mechanochemical Transduction: A Mechanogenerated Acid. *J. Am. Chem. Soc.* **2012**, *134*(30), 12446-12449**.**

(27) Peterson, G. I.; Larsen, M. B.; Ganter, M. A.; Storti, D. W.; Boydston, A. J. 3D-Printed Mechanochromic Materials. *ACS Appl. Mater. Interfaces* **2015**, *7*(1), 577-583**.**

(28) Ramirez, A. L. B.; Kean, Z. S.; Orlicki, J. A.; Champhekar, M.; Elsakr, S. M.; Krause, W. E.; Craig, S. L. Mechanochemical Strengthening of a Synthetic Polymer in Response to Typically Destructive Shear Forces. *Nat. Chem.* **2013**, *5*(9), 757**.**

Chapter 2. Additive Manufacturing with a Flex Activated Mechanophore for Nondestructive Assessment of Mechanochemical Reactivity in Complex Object Geometries[2]

2.1 Abstract

We used digital light processing additive manufacturing (DLP-AM) to produce mechanochemically responsive test specimens from custom photoresin formulations, wherein designer, flex activated mechanophores enable quantitative assessment of the total mechanophore activation in the specimen. The manufactured object geometries included an octet truss unit cell, a gyroid lattice, and an "8D" cubic lattice. The mechanophore activation in each test specimen was measured as a function of uniaxial compressive strain applied to the structure. Full shape recovery after compression was exhibited in all cases. These proof-of-concept results signify the potential to use flex activated mechanophore for nondestructive, quantitative volumetric assessment of mechanochemistry in test specimens with complex geometries. Additionally, the integration of DLP-AM with flex activated mechanophore build materials enable the creation of customizable, three-dimensional mechanochemically responsive parts that exhibit small molecule release without undergoing irreversible deformation or fracture.

[2] Reproduced with permission from Cao, B., Boechler, N., & Boydston, A. J. (2018). Additive manufacturing with a flex activated mechanophore for nondestructive assessment of mechanochemical reactivity in complex object geometries. *Polymer*, 152, 4-8. Copyright 2018 Elsevier.

2.2 Introduction

Mechanophores are molecular moieties that respond chemically to external mechanical stimuli[1]. In materials that contain mechanophores, macroscopic strains are translated into molecular-scale deformations at the mechanophore, which augment the potential energy surface toward specific chemical reactivity. To date, mechanophores have been demonstrated in polymers and network materials to achieve behaviors such as color change (mechanochromism)[2-4], enhanced luminescence[5], fluorescence[6], catalysis[7], self-reinforcement[8], polymer backbone structural reconfiguration[9], and small molecule release[10]. Besides molecularly designing new mechanophores that undergo force-induced bond cleavage[11], cycloreversion[12], or electrocyclic ring opening[13], efforts have been made to bridge functional mechanophores with engineering applications. For example, Zhao and coworkers fabricated electro-mechano-chemically responsive elastomeric display systems that were able to generate fluorescent patterns by coupling the mechanochemical isomerization of spiropyran with macroscopic shape deformation caused by applied electric fields[14]. In a demonstration of autonomously self-reinforcing materials, Craig and coworkers explored polymeric materials that contained *gem*-dibromocyclopropane mechanophores, wherein spontaneous nucleophilic substitution resulted in crosslinking and strengthening of the material under otherwise destructive forces[8].

As polymer mechanochemistry continues to develop as an avenue for designing stimuli-responsive materials, one can begin to consider opportunities at the interfaces of mechanochemistry and manufacturing. One of the most rapidly developing manufacturing techniques is additive manufacturing (AM), commonly referred to as "3D printing", which has enabled the production of complex three-dimensional (3D) structures with relative ease[15]. Recently, the fabrication of rapidly customizable mechanochromic devices was achieved through the

integration of custom mechanochromic filaments with melt material extrusion AM[16,17]. These reports signified a potentially exciting opportunity to pair molecular-level strain sensitivity with custom macroscopic object geometries. As an early step toward realizing the potential of AM with mechanochemically responsive build materials, we sought a mechanophore that could quantitatively "report" activation throughout a geometrically complex object.

In many cases, mechanophore activation is assessed through spectroscopic means, which involves either fabrication of test samples that are specific to the method of analysis, or processing of the bulk material in a way that destroys the test specimen (e.g., dissolving the material for solution-based analyses). Mechanochromic responses can help address this challenge, but quantitative assessment is often limited to smooth, flat surfaces that are optically accessible. For instance, lattice and microstructed materials would each present formidable challenge to comprehensive assessment of mechanochromism. We hypothesized that mechanophores capable of releasing extractable, small molecules could provide a means toward quantifying mechanophore reactivity throughout the entire volume of a test specimen without requiring dissolution, digestion, or otherwise destroying the specimen. Flex activated mechanophores, such as oxanorbornadiene (OND), are potentially good candidates for such applications [18]. The OND mechanophore was previously demonstrated in bulk thermoplastics and polyurethane elastomers to release a small molecule (benzyl furfuryl ether) that could be extracted and quantified after mechanical activation (Figure 2.1)[10,18]. One notable caveat is that the efficiency of extraction would be dependent upon the swelling characteristics of the bulk material and the dimensions of the test specimen. In this study, we present the first demonstration, and characterization, of 3D structures with complex object geometries fabricated via AM, which incorporate a flex activated mechanophore that

enables the quantitative assessment of mechanophore activation within mechanically reversible regimes.

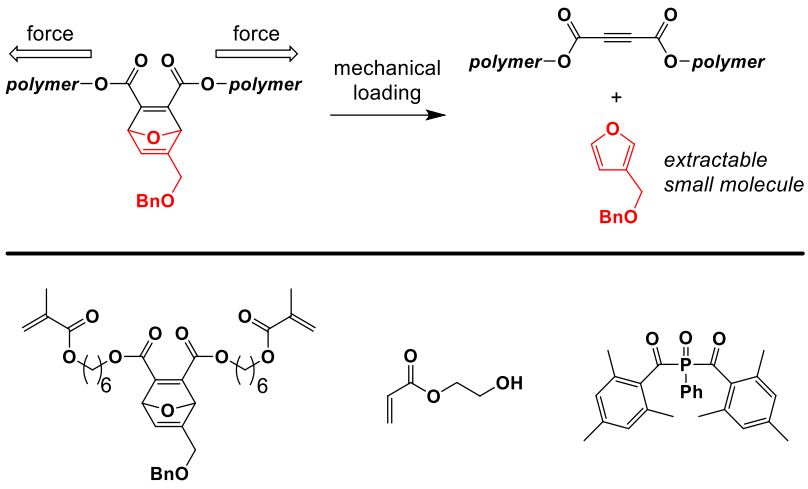

Figure 2.1 Top: Generalized depiction of mechanochemical flex activation of an oxanorbornadiene under mechanical load. Bottom: Chemical structures of components of the photoresin formulation used in this study; left-to-right: OND mechanophore, 2-hydroxyethyl acrylate (HEA), Irgacure 819.

2.3 Results and Discussion

We first selected an appropriate AM method based on the intended target geometries of our test specimens (e.g. lattice materials) and the inherent reactivity of the OND mechanophore. The desire to have overhangs and void spaces within lattice designs prompted the use of vat photopolymerization[19]. Moreover, the general thermal instability of OND substrates was likely to preclude melt material extrusion. As a subset of vat photopolymerization, we applied digital light processing additive manufacturing (DLP-AM) in our studies to enable efficient printing with visible light[20], therefore also avoiding photochemical degradation of the OND that occurs upon exposure to UV light[21]. Previous success with customizable photoresins for DLP-AM, including the production of elastomeric and graded materials, encouraged the possibility of incorporating an

appropriately functionalized OND mechanophore[22,23]. The stability of the OND moiety within the DLP-AM process was examined by irradiating an OND-diol in deuterated chloroform ($CDCl_3$) solution with white light from the projector used during the AM process. After 2 h of exposure to the projector light, the NMR spectrum (Figure S2.4) showed no changes in comparison with the pristine OND-diol. This result suggested that the AM conditions would not cause photochemical degradation of the OND moiety.

To incorporate oxanorbornadiene chemically into crosslinked polymer networks during the DLP-AM process, we prepared an oxanorbornadiene-dimethacrylate (OND-DMA) as previously described[10]. This structure enables crosslinking during photocuring with the mechanophore positioned within the bridging network segment, such that the mechanical strain can be transduced into chemical potential. The complete photoresin was comprised of 98.52 wt % of 2-hydroxyethyl acrylate (HEA), 0.49 wt % of Irgacure 819 as photointiator, and 0.99 wt % of OND-DMA. Additionally, 0.01 wt % of Nile Red was added to the resin as a light absorber to decrease the outgrowth during AM. The DLP-AM setup is diagramed in Figure S2.5 and the schematic of the layer-by-layer printing process is shown in Figure S2.6, illustrating the direct formation of the mechanophore-containing polymer networks from liquid resins.

To investigate the printability of the resin and characterize the mechanical properties of the printed material, dogbone tensile test specimens (dimensions: 63.50 mm × 9.53 mm × 3.20 mm) were printed and evaluated via uniaxial tension tests. We first investigated the effects of layer cure time on the printed material's mechanical properties by the measuring the load as a function of monotonically increasing strain until the point of specimen fracture. As presented in Figure 2.2a, the stress-strain curves of test specimens printed with layer cure times ranging from 5 s to 11 s showed similar mechanical behavior. The tests specimens also demonstrated a significant

elongation at break, with strains (defined here as ΔL/L, where ΔL is the increase of distance, and L is the original distance, between the tensile tester grips) ranging from 156% to 188% (Figure 2.2b, elongation measured by tracking two marks, made within the specimen's gage region, using a video extensometer). The calculated Young's moduli (Fig. 2.3a) were in the range of 0.61 MPa to 0.77 MPa, indicating the low stiffness of the printed material which can be used for deformation with full shape recovery upon removing the loads. The viscoelasticity of the material was revealed by the storage modulus and loss modulus shown in Fig.2.3b. The material response became nonlinear with the decrease of the storage modulus at high oscillation strain may result from the rupturing of the hydrogen bonding in HEA. The gel fraction of a representative disc-shaped sample was determined by performing Soxhlet extraction (detailed procedures in Supporting Information) and found to be 97.7%, suggesting high efficiency of crosslinking during the printing process. These results are consistent with our previous investigations of HEA-based photoresins for DLP-AM[22].

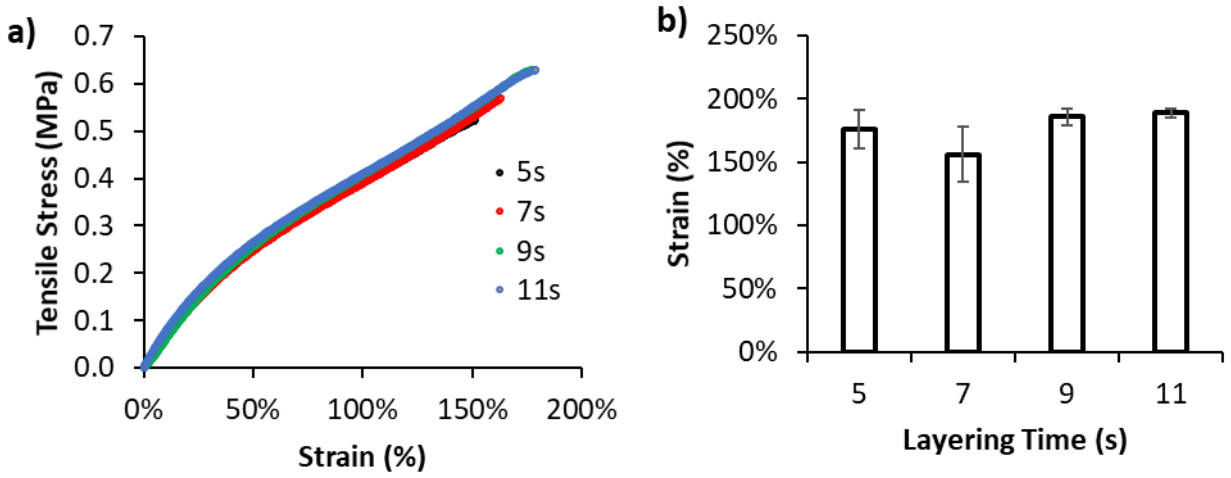

Figure 2.2 a) Representative tensile test results for printed specimens (ASTM D638 Type V, strain rate = 20 mm/min, gauge length = 9.53 mm) at different layering time (5s, 7s, 9s, and 11s), b) Strain at break for printed specimens at different layering times. Error bars represent standard deviation over three samples.

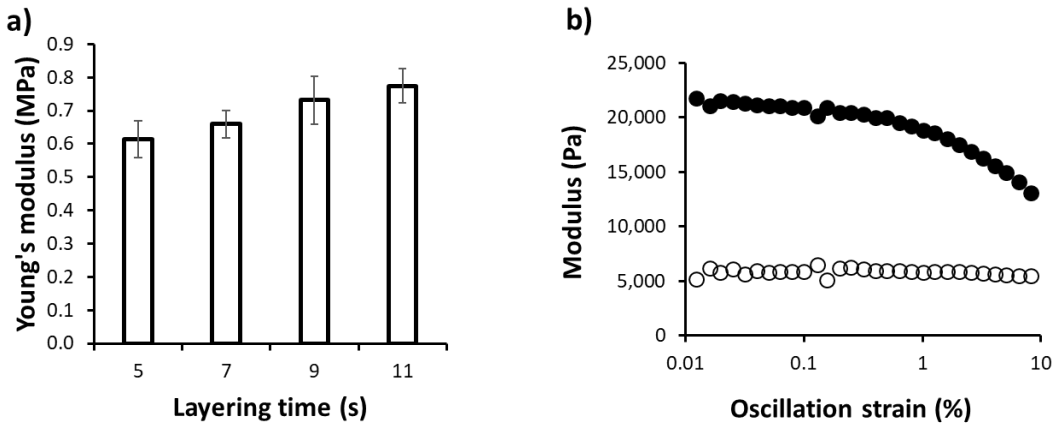

Figure 2.3 a) Young's modulus for printed specimens at different layering time, b) Rheometrical characterization of printed cylinders at 25 °C. The storage modulus (G′) is represented by solid circles, the loss modulus (G″) is represented by hollow circles. Error bars represent standard deviation over three samples.

The persistence of the mechanochemical reactivity after additive manufacturing was investigated by printing thin slabs (dimensions: 29.32 mm × 29.32 mm × 1.00 mm) using the prepared resins. The slabs were cut into small pieces, placed into a die set, and then compressed uniaxially using an Instron 5585H Universal Testing System. Bulk compression at sustained pressures, as indicated in Figure 2.4, was held for 1 min. The samples were then soaked in hexane for 24 h to extract the released benzyl furfuryl ether. During extraction, the samples were found to swell and remain intact. The extract was then analyzed by gas chromatography mass-spectrometry (GC-MS) using an internal standard. The percent activation of the flex-activated mechanophore was calculated based on the amount of released small molecules versus the initial feed ratio of the OND-DMA in the resin[18]. As can be seen in Figure 2.4, the 3D printed slabs showed a low amount of background activation (ca. 0.52%) without compression. A monotonic increase in the activation, up to ca. 2.47%, was observed with applied pressure of up to 125 MPa. The observed mechanochemical profile of these materials are similar to those previously reported, and consistent with mechanical impetus as the driving force for the reaction[10,18]. Moreover, the OND

mechanophore does not give false positive results during the applied GC-MS protocol, consistent with our previous studies of this system[10,18].

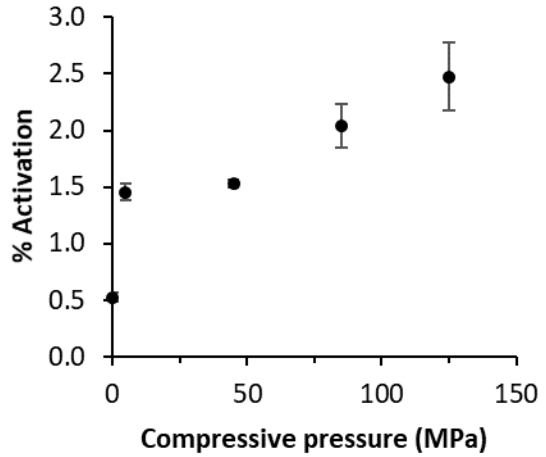

Figure 2.4 Plot of % mechanophore activation in a printed specimen (cut, printed slabs) versus applied pressure, as judged by GC-MS analysis of extract solutions after compression. Error bars represent the standard deviation over three samples.

Having successfully confirmed the mechanochemical reactivity of the mechanoresponsive materials after DLP-AM, we targeted more complex object geometries for the test specimens. Specifically, we investigated an octet truss unit cell (exterior dimensions: 14.66 mm × 14.66 mm ×14.66 mm)[24], an "8D cubic lattice" (exterior dimensions: 17.74 mm × 17.74 mm ×18.75 mm) , and a gyroid lattice (exterior dimensions: 14.91 mm × 14.91 mm × 12.34 mm) architecture[25]; representative printed specimens are depicted in Figure 2.5. The printed samples were uniaxially compressed in the Instron load frame to 20%, 40%, 60%, and 80% global strain (compression details and images are shown in the Supporting Information), where the definition of "global strain" is the compression of the entire structure divided by the original height. The octet truss unit cell and 8D cubic lattice specimens buckled during the course of compression, however each of the

samples fully recovered to their original shape without visibly observable fracture or failure of any structural components.

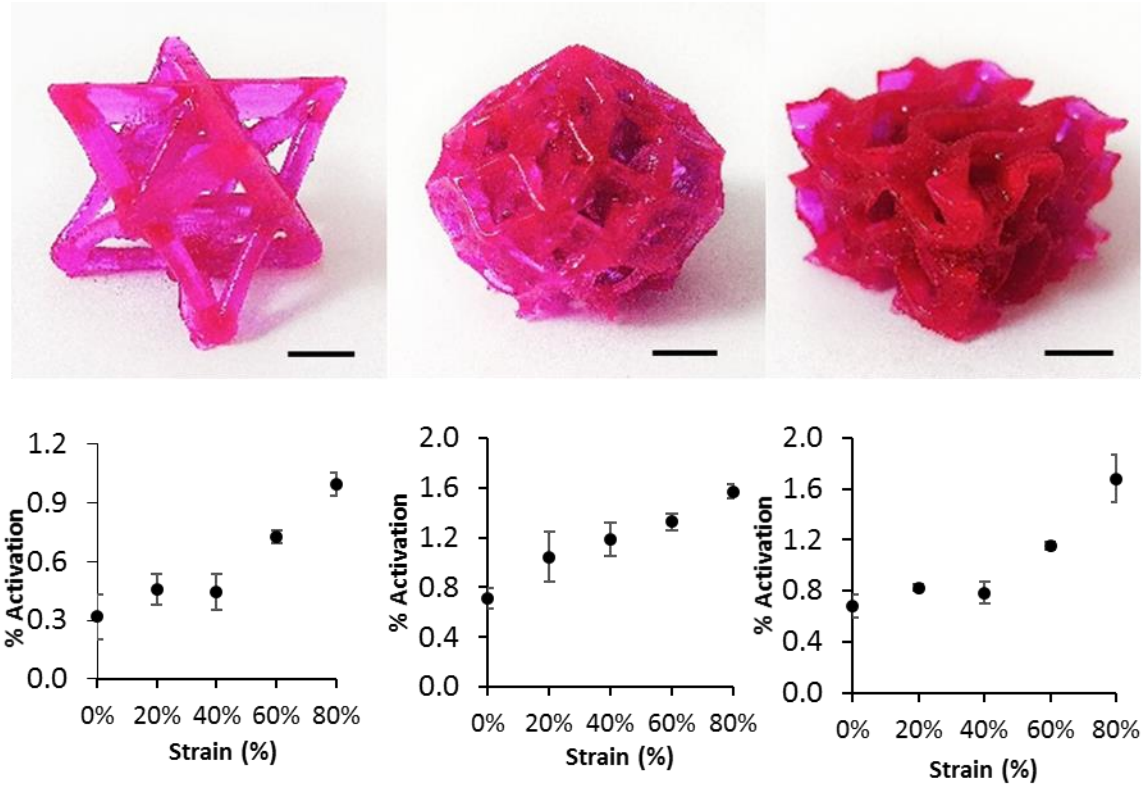

Figure 2.5 Top: Left-to-right: As printed octet truss unit cell, 8D cubic lattice, and gyroid lattice. Bottom: Left-to-right: plot of % activation of mechanophore after compression of octet truss unit cell specimens, 8D cubic lattice specimens, and gyroid lattice specimens. Error bars represent standard deviation over three samples. Scale bars = 5 mm.

As in the case of the cut, printed slabs, without compression, each specimen type displayed relatively low mechanophore activation. While the activation of the cut slabs might be attributed to the deformation induced by cutting the slabs, this effect would not be present in the specimens shown in Figure 2.5, and as such, we suggest this baseline activation may be ascribed to thermal activation during printing or solvent-induced swelling during the extraction protocol. Upon uniaxial compression, the mechanophore-containing objects revealed increasing levels of mechanophore activation with increasing applied global strain (Figure 2.5). Specifically,

mechanophore activation in octet truss unit cells increased from 0.32% to 0.99% when the global strain was increased from 0 to 80%. The 8D cubic lattice and gyroid lattice samples each displayed slightly greater maximum activation (1.57% and 1.68%, respectively) in comparison with the octet truss unit cell. Notably, the octet truss unit cell and gyroid lattice displayed similar activation-strain profiles, with steep increases near 60% to 80% strain. These observations are consistent with the applied force profiles measured for each object geometry (Figures S2.8 and S2.10), which exhibit a stiffening within this strain region that would be consistent with densification of, and the onset of self-contact within, the lattice (Figure S2.11). However, it is thus far unclear within the context of this explanation as to why the 8D cubic lattice does not exhibit a similar increase in mechanophore activation slope, particularly given the similar applied force profiles (Figure S2.9). These results highlight the sensitivity of the mechanophores to behave as local, molecular-level strain probes that respond to different local strains generated as a result of the object's unique geometry and mechanical behavior.

2.4 Conclusions

In summary, we have confirmed the compatibility of a flex activated OND mechanophore with DLP-AM techniques. To our knowledge, this is the first demonstration of AM with a flex activated mechanophore. The OND mechanophore was incorporated into an elastomer photocurable resin that resulted in good printing characteristics for a series of micro-structured test specimens. This enabled investigation of the force-induced small molecule release characteristics of the printed material by bulk compression studies. Moreover, the differing extents of mechanophore activation observed for several complex geometries created by DLP-AM opens a

new avenue for using this mechanophore to explore the strain distribution in sophisticated 3D architectures and the tailoring of mechanochemical activation via designed object geometry.

2.5 Experimental

2.5.1 Materials and Equipment

Dimethylformamide (DMF) and tetrahydrofuran (THF) were obtained from an in-house designed solvent purification system. The synthesis and characterization procedure of oxanorbornadiene dimethacrylate (OND-DMA) were as reported below. ^{1}H NMR spectra were obtained from the Burke AVance 301 MHz or 500 MHz spectrometers. GC-MS analysis was performed with a combined Hewlett Packard 5973 Mass Selective Detector and HP 6890 Series GC System using an Agilent 7683 Series Injector. The thermal profile was optimized so as to preclude thermal activation of residual oxonorbornadiene upon injection and/or chromatographic separation. GC/MS was accomplished with injection temperature of 150 °C, injection volumes of 1 μL, an initial oven temperature of 60 °C held for 1 min, ramped from 15 °C/min to 250 °C and held for 3 min. Light intensity of the projector used for 3D printing was measured using an Extech Instruments light meter (model HD450). Compression tests and tensile tests were conducted by an Instron 5585H Universal Testing System at a rate of 20 mm/min and Bluehill 3.0 software. An Instron 2663-821 Advanced Video Extensometer was used to measure strain, by tracking the position of two marks made within the specimen's gage region, during elongation on the ASTM D638 type V specimen samples. Rheology measurements were taken on a TA Instruments Discovery HR-2 hybrid rheometer using a stainless steel 20 mm Peltier plate. Data were collected from a strain sweep test from 10 to 50 000 Pa at 25 °C and an angular frequency of 6.28 rad/s. 2-Hydroxyethyl acrylate (HEA) was purchased from ACROS Organics. Bis(2,4,6-trimethylbenzoyl)-phenylphosphineoxide (Irgacure 819) was purchased from Sigma-Aldrich. Nile Red was purchased from TCI America. All chemicals were used as received without additional purification.

2.5.2 Synthesis procedure of small molecule components

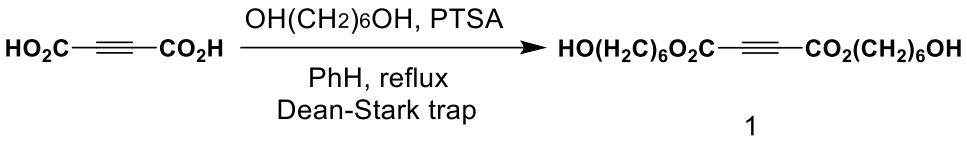

1

Preparation of 1. Dissolve acetylene dicarboxylic acid (43.8mmol), 1,6-hexanediol (219mmol), hexanol (438mmol) into 70mL benzene. Then p-toluenesulfonic acid monohydrate(4.38mmol) was added into the system as catalyst. Dean-stark trap was installed and the reaction was heated to reflux for 20 hours. The solution was diluted with diethyl ether and the solution was cooled in freezer for 3 hours to cause precipitate. The decanted solution was washed successively with saturated sodium bicarbonate for 2 times, DI water for 4 times, and brine for 1 time. The solution was dried over $MgSO_4$, filtered through a pad of Celite and then concentrated under reduced pressure to yield pale yellow oil.

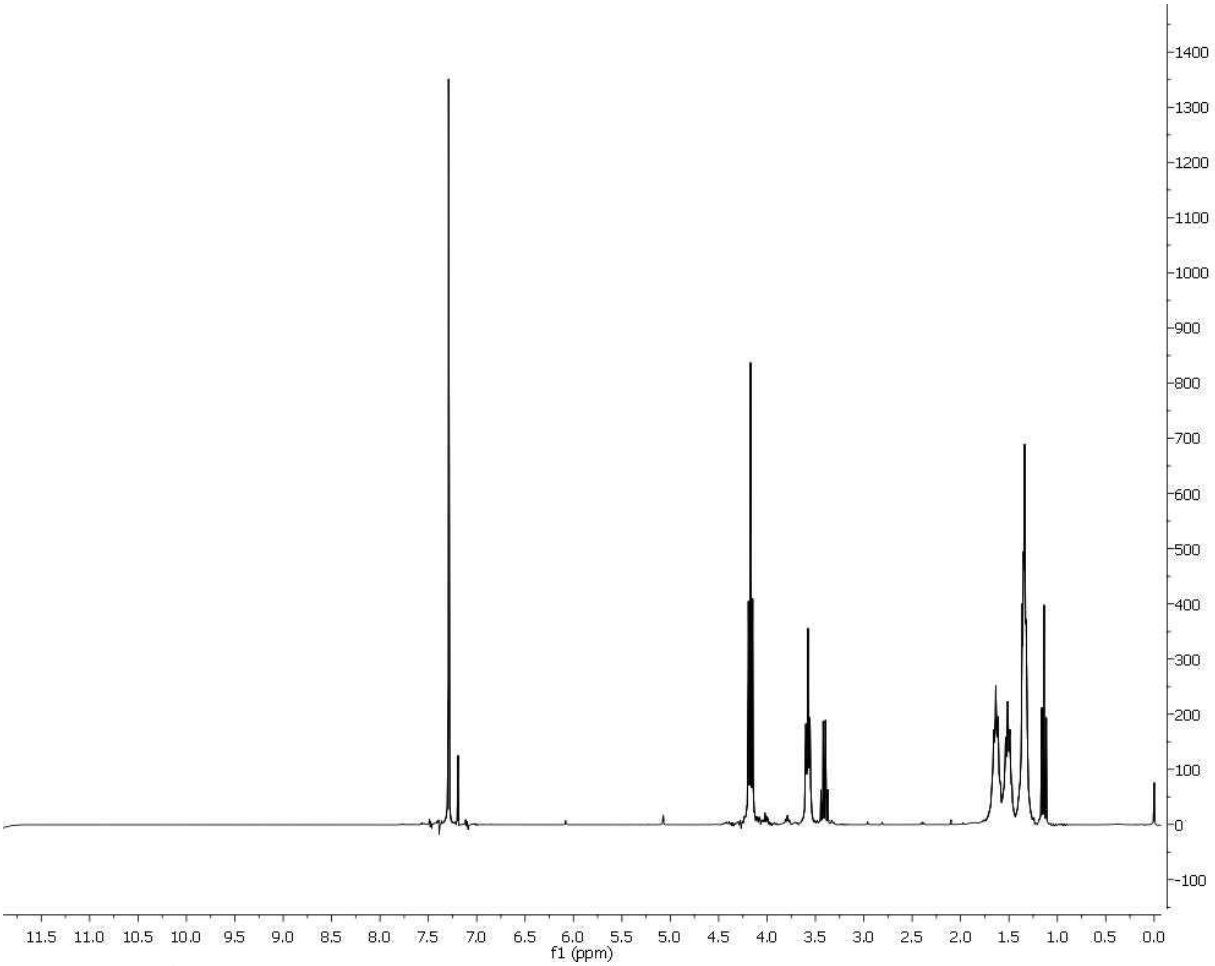

Figure S2.1 ^{1}H NMR spectrum of compound 1 (solvent=$CDCl_3$).

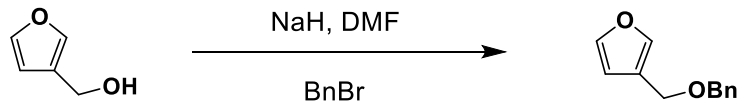

2

Preparation of 2. In the glove box, add sodium hydride (31.6mmol) into the solution of 3-furfuryl alcohol (21.1mmol) in dry DMF. After 30 minutes, benzyl bromide (23.2mmol) was added into the system. The reaction was taken out of the glove box and stirred at room temperature for 6 hours. Then excess sodium hydride was consumed by adding 50mL water dropwise. The solution was extracted with hexanes for 4 times, rinsed with brine, dried over $MgSO_4$, and concentrated under

reduced pressure. The crude product was purified by eluting through a silica plug with 15% ethyl acetate/hexanes to yield orange oil.

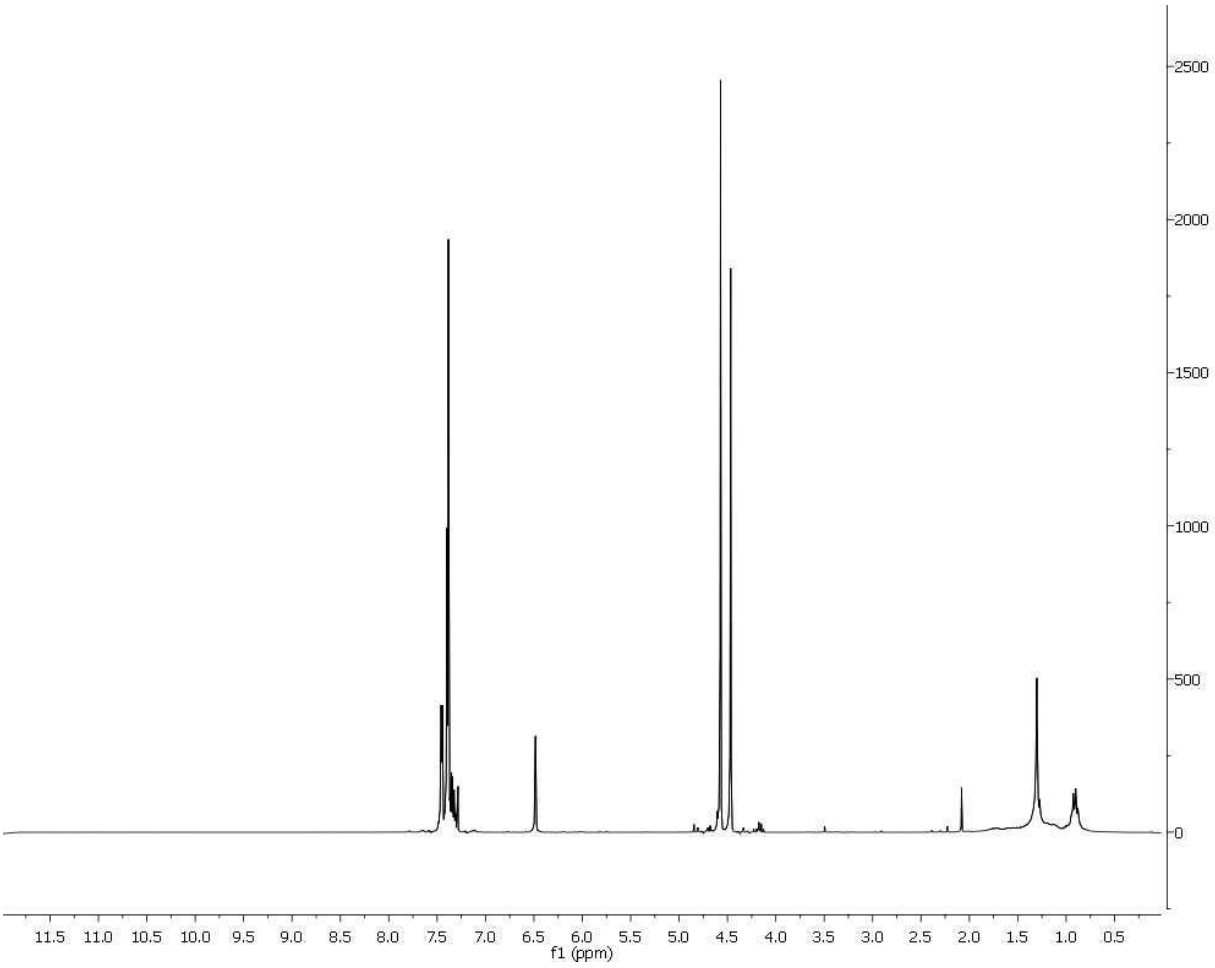

Figure S2.2 ^{1}H NMR spectrum of compound 2 (solvent=$CDCl_3$).

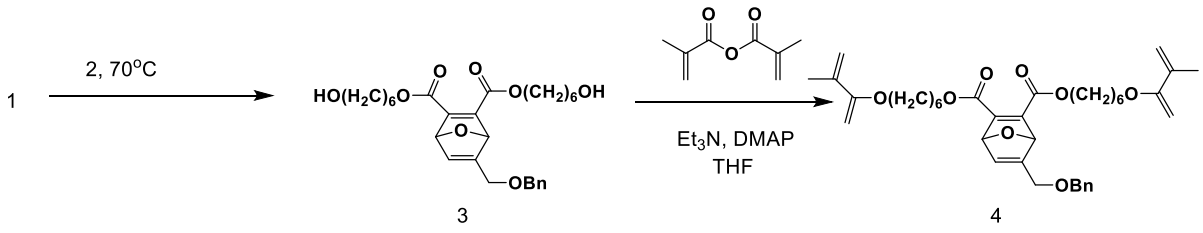

Preparation of 3. React 1 and 2 in a screw cap vial. The vial was sealed and heated at 70 ^{o}C for 18 hours. The crude product was titrated by hexanes and concentrated down to yield orange oil.

Preparation of 4. 3 and DMAP were dissolved in the mixture of anhydrous THF/Et_3N. Methacrylic anhydride was added dropwise into the solution and the reaction was monitored by TLC (80% ethyl acetate/hexanes). The reaction was diluted with 120mL diethyl ether, rinsed with water for 2 times, saturated sodium bicarbonate for 3 times, brine for 1 time, dried over $MgSO_4$ and concentrated under reduced pressure. The crude product was purified by eluting through a silica plug with 50% ethyl acetate/hexanes to yield yellow oil.

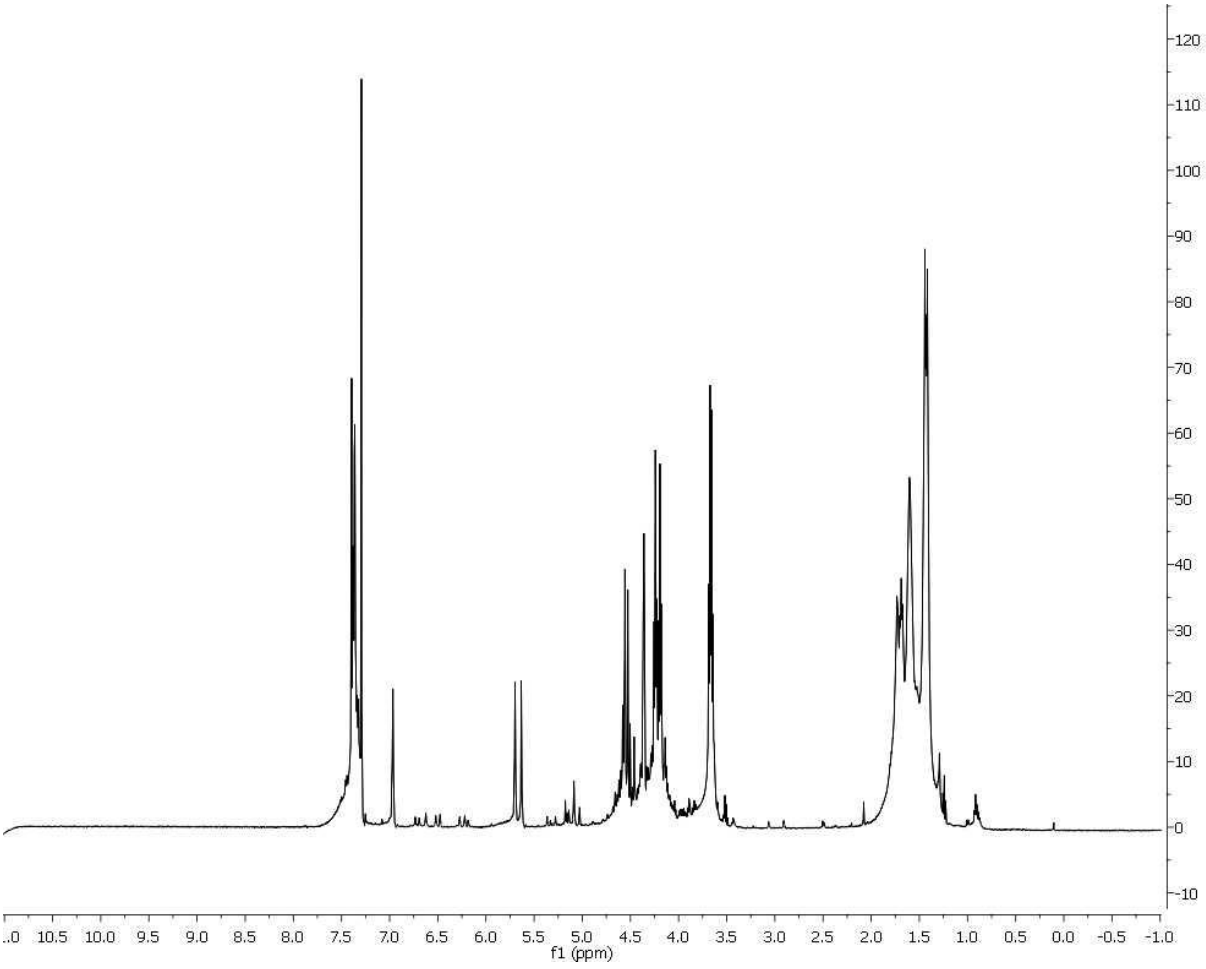

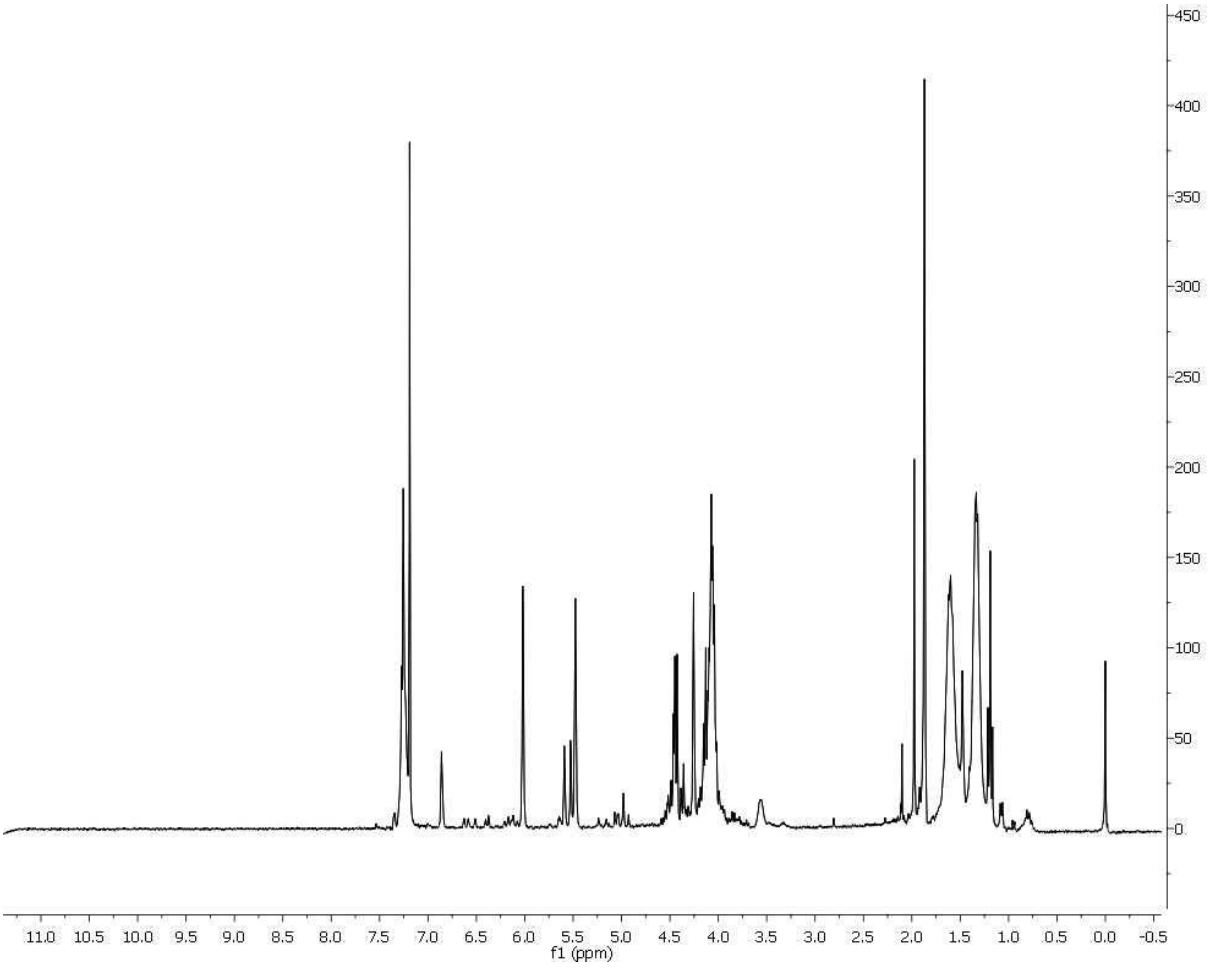

Figure S2.3 ^{1}H NMR spectra of compound 3 (top) and compound 4 (bottom) (solvent=$CDCl_3$).

2.5.3 Stability of the mechanophore under projector light

Oxanorbornadiene-diol (molecular structure shown below) was dissolved in deuterated chloroform ($CDCl_3$). NMR spectra were taken before and after irradiating the projector light (light intensity described as above) used for the 3D printing process onto the NMR tube for 2 hours.

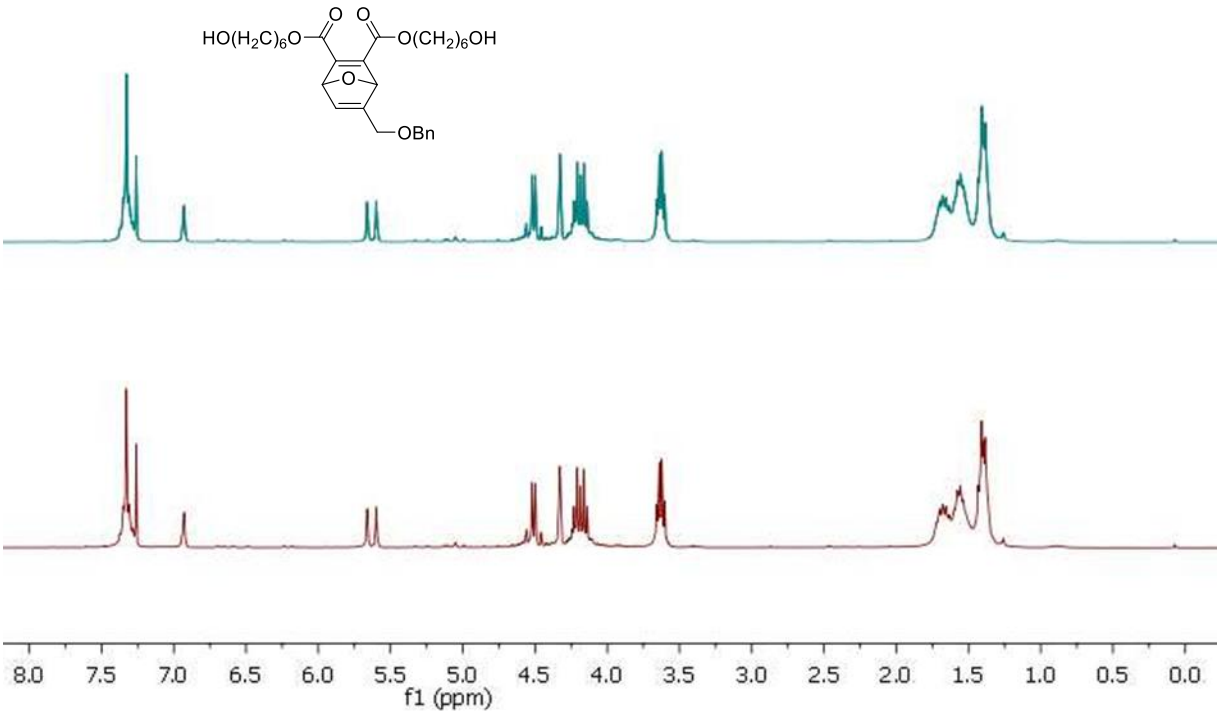

Figure S2.4 ^{1}H NMR spectra of oxanorbornadiene-diol (OND-diol) before (top) and after (bottom) being irradiated by the light from the projector for 2 h.

2.5.4 Preparation of photocurable resins

The photoresins were prepared by mixing 20 g of HEA, 0.2 g of OND-DMA, 0.1 g of Irgacure 819 as photoinitiator, and 2 mg of Nile red as dye in a 20 mL screw cap vial. The resins were sonicated by Branson 1510 sonicator for 30 s before use.

2.5.5 Digital light processing additive manufacturing

General procedure.

The 3D printing was performed using the SeeMeCNC Droplit Kit Digital light processing (DLP) printer (the build and vat plates were modified to accommodate leveling, as described previously) and the Optoma HD20 projector with light intensity decreased to 40%. The printer settings for

each photoresin were shown below. Layer cure times were chosen to provide objects with visibly good printability, without under-cure, overgrowth, or adhesion issues to the build vat. The printer and projector were controlled by Creation Workshop (version 1.0.0.75) software. This software was also used to covert the 3D files (STL format) into image stacks (CWS format) for printing. The build vat consisted of a Pyrex petri-dish (d=90 mm) with a layer of elastomer (ca. 11 g of silicone applied to dish) or a 150 mL Pyrex beaker (ca. 6 g of silicone applied to dish). Prints were performed by repeating the process of projecting an image into the resin followed by raising the z-stage (Fig.S2.5 and S2.6).

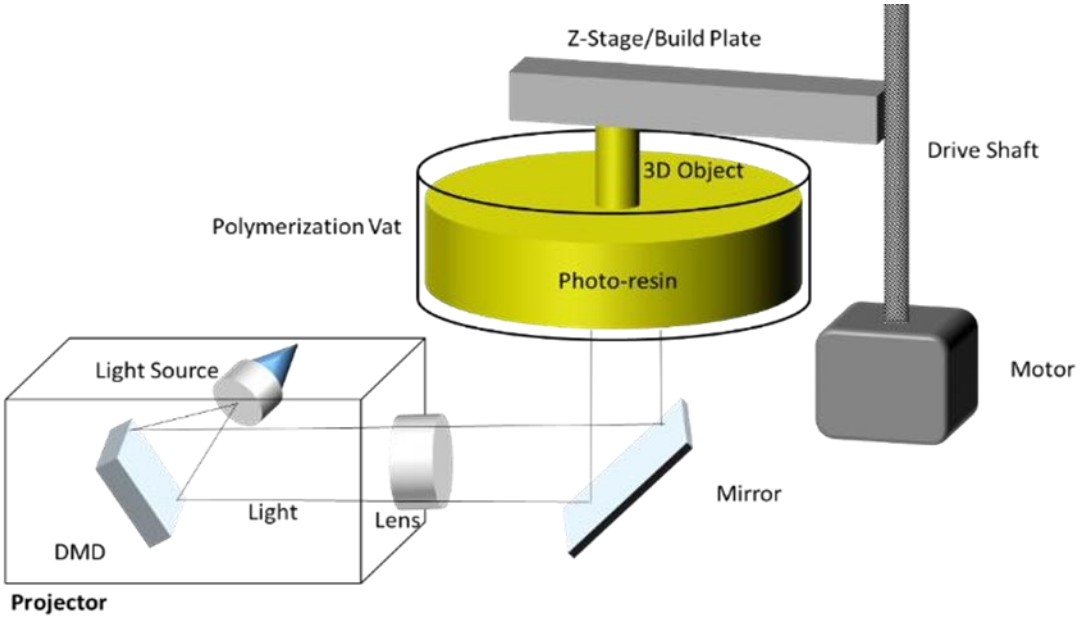

Figure S2.5 Schematic of a DLP 3D printer. In typical DLP systems, 3D model files are sectioned into thin slices, or layers, which are represented by a series of black and white images. Objects are printed by sequential projection of each image into the resin while raising the z-stage between each image.

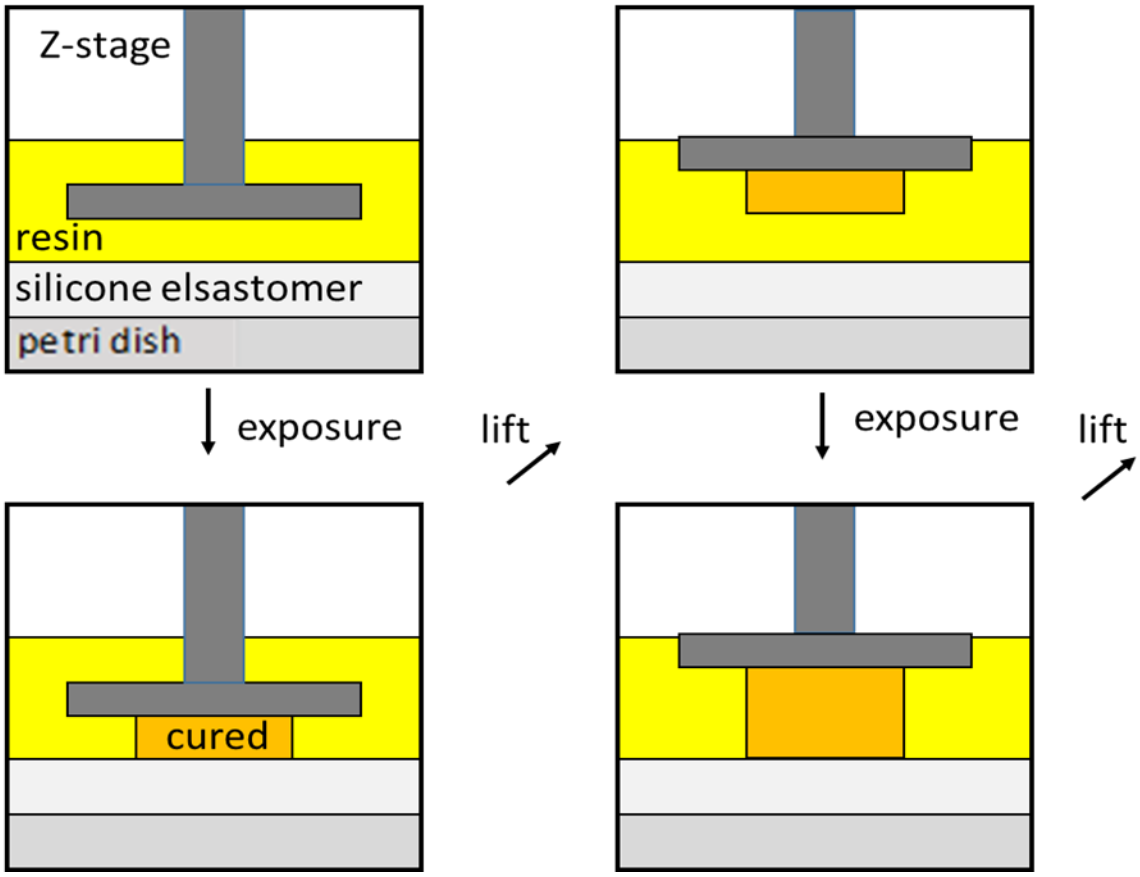

Figure S2.6 Schematic of the iterative additive manufacturing process. Objects are printed by projecting an image into the resin and raising the z-stage (to give the desired layer height) repeatedly until the whole object has printed.

3D printing parameters.

Light intensity: 60 klux

Layer thickness: 0.1 mm

Number of bottom layer: 3

Lift and Sequence time: 9000 ms

Z lift distance: 3 mm

Z lift speed: 100 mm/min

Z bottom speed: 100 mm/min

Z retract speed: 100 mm/min

Exposure time: 7000 ms for thin slabs, octet truss unit cell, gyroid lattice, and cylinder specimens for rheology tests. 9000 ms for 8D cubic lattice. 5000 ms, 7000 ms, 9000ms, or 11000 ms for specimens for tensile tests.

Bottom exposure time: 7000 ms for thin slabs, octet truss unit cell, gyroid lattice, and cylinder specimens for rheology tests. 9000 ms for 8D cubic lattice. 5000 ms, 7000 ms, 9000ms, or 11000 ms for specimens for tensile tests.

Post-cure procedure: All printed samples (including tensile specimens, samples for bulk compression, and objects with complex geometries) were bathed in excess white light at 60 klux intensity for 30 seconds per side to polymerize unreacted monomer and remove effects of under-curing that may come from the printing process.

2.5.6 Determination of gel fraction of printed sample

A printed disc (r = 10 mm, h = 1 mm) was weighed before extraction. It was then placed in a Supelco small Soxhlet extraction apparatus (50 mL extractor capacity, extractor I.D. 30 mm, 125 mL flask capacity, glass thimble), and successive extractions were carried out over 7 h with CH_2Cl_2. The disc was placed under reduced pressure at 40 °C for 15 h to remove the residual solvent. The mass of the dried disc was recorded afterwards. The gel fraction was calculated by the following equation:

$$\text{Gel fraction} = \left(\frac{Wd}{Wi}\right) \times 100$$

Where the Wi is the initial weight of the dried sample and Wd is the weight of the insoluble part of the sample after dried under reduced pressure.

2.5.7 General Procedure for bulk compression studies

3D printed thin slabs were cut to small pieces and loaded into a die set. The sample was compressed at the desired pressure (calculated by dividing the measured load by area of the pellet press surface, 6.34 mm radius) by Instron for 1 min. After compression, the sample was transferred to a vial and soaked in hexane for 24 hours. The soak solution was then analyzed by GC-MS with known amount of 1,3,5-trimethoxybenzene as internal standard and the % activation was determined by dividing the observed furan by the total amount present in the polymer sample.

2.5.8 General Procedure for compression on octet truss unit cells, 8D cubic lattice, and gyroid lattice

The 3D printed objects were compressed by Instron to desired global strain at a rate of 20 mm/min. The specimens were held at the strain for 1 min. Specifically, the largest side length was chosen to be the z direction during the compression for the gyroid lattice samples, as shown in Fig. S2.8. The compressed objects were soaked in hexane for 24 hours. The GC-MS analysis was conducted as described above. Samples were not soaked in solvent prior to compression. The % activation increase of the mechanophore was observed by the comparison with the uncompressed sample as a control. Representative GC-MS data for gyroid lattice was shown in Fig.S2.7.

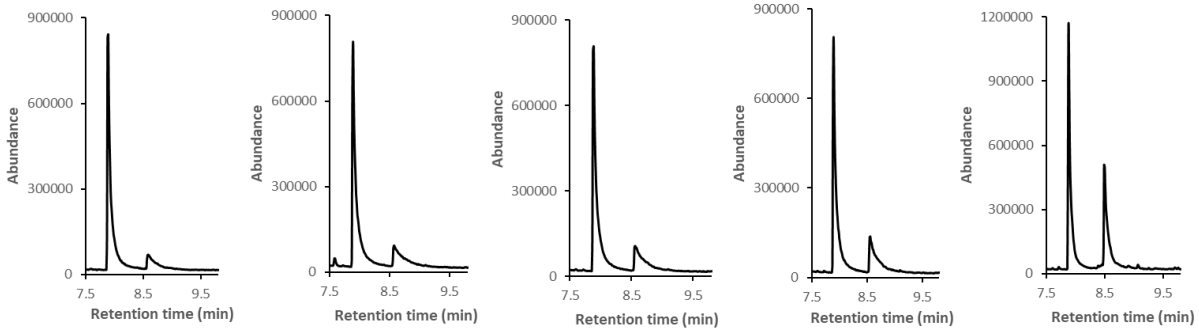

Figure S2.7 Left-to-right: representative GC-MS data for the soak solution of gyroid lattice compressed to 0%, 20%, 40%, 60%, 80% global strain. The peak of 1,3,5-trimethoxybenzene has the retention time at 7.888 min. The peak of the benzyl furfuryl ether has the retention time at 8.504 min.

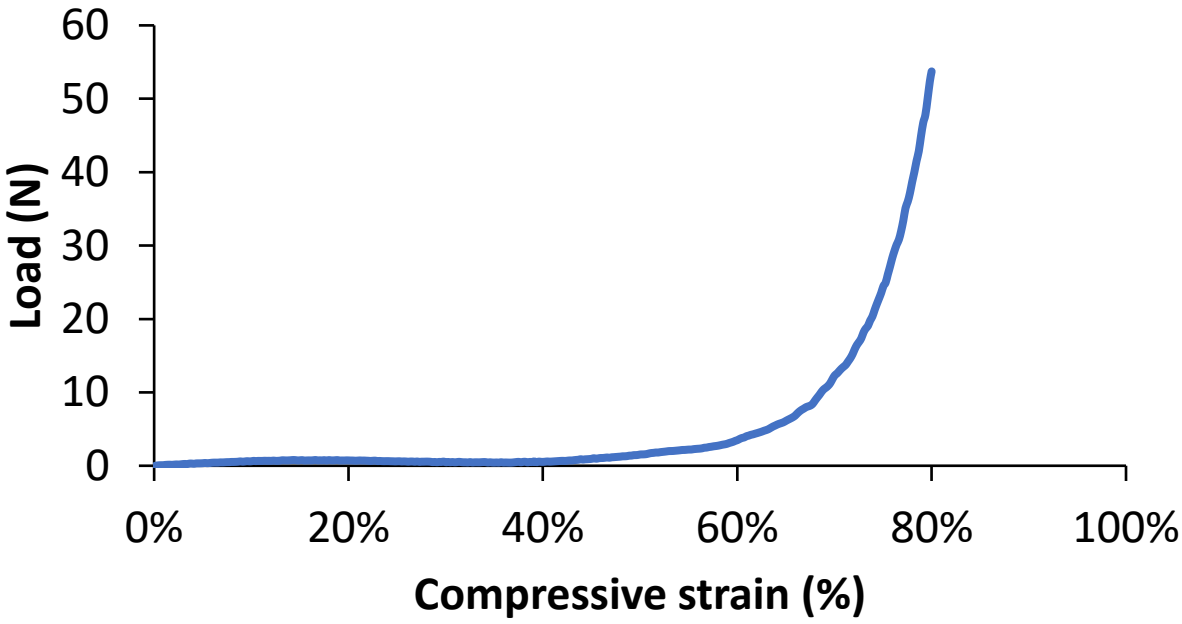

Figure S2.8 Representative load-strain curve for compression of 3D printed octet truss unit cell to 80% global strain

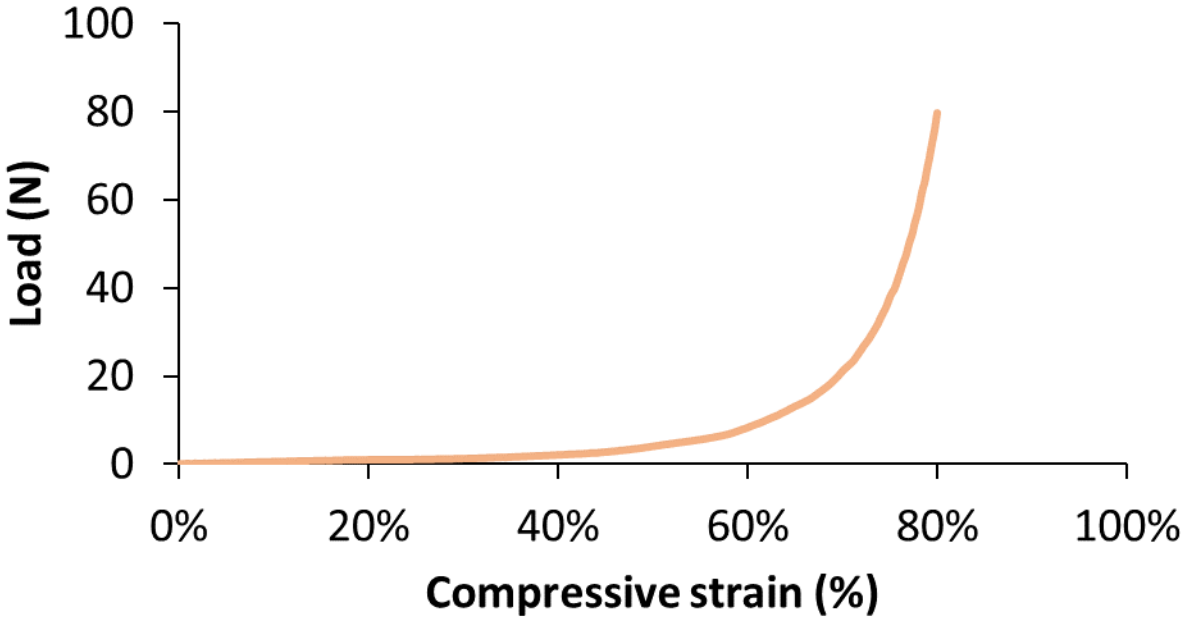

Figure S2.9 Representative load-strain curve for compression of 3D printed 8D cubic lattice to 80% global strain

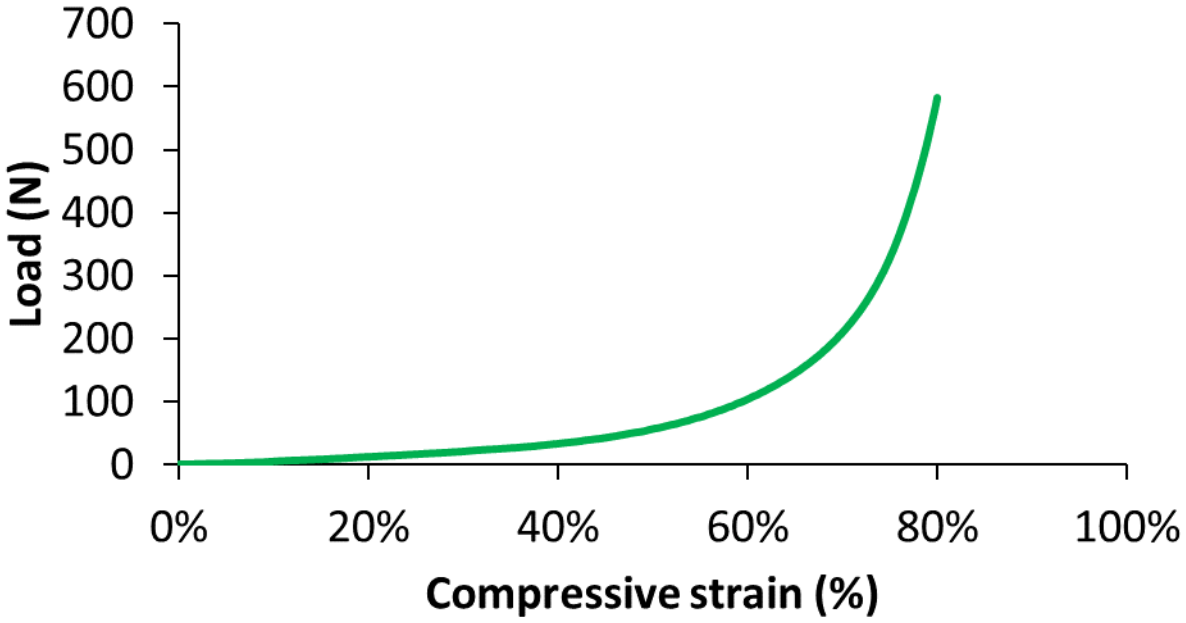

Figure S2.10 Representative load-strain curve for compression of 3D printed gyroid lattice to 80% global strain

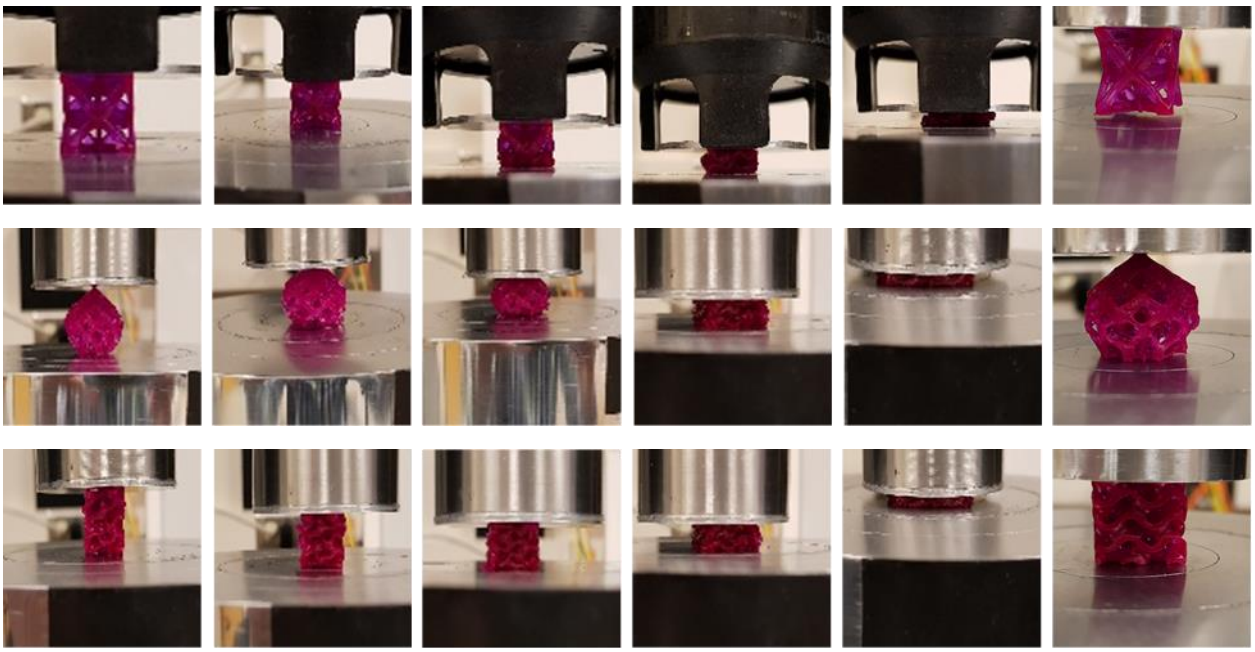

Figure S2.11 Top row: octet truss unit cell. Middle row: 8D cubic lattice. Bottom row: Gyroid lattice. Left-to-right within each row: 0%, 20%, 40%, 60%, 80%, 0% (post compression) global strain.

2.6 References

(1) Li, J.; Nagamani, C.; Moore, J. S. Polymer Mechanochemistry: From Destructive to Productive. *Acc. Chem. Res.* **2015**, *48*(8), 2181–2190.

(2) Davis, D. A.; Hamilton, A.; Yang, J.; Cremar, L. D.; Van Gough, D.; Potisek, S. L.; Ong, M. T.; Braun, P. V.; Martínez, T. J.; White, S. R.; Moore, J. S.; Sottos, N. R. Force-Induced Activation of Covalent Bonds in Mechanoresponsive Polymeric Materials. *Nature* **2009**, *459*(7243), 68–72.

(3) Robb, M. J.; Kim, T. A.; Halmes, A. J.; White, S. R.; Sottos, N. R.; Moore, J. S. Regioisomer-Specific Mechanochromism of Naphthopyran in Polymeric Materials. *J. Am. Chem. Soc.* **2016**, *138*(38), 12328–12331.

(4) Imato, K.; Irie, A.; Kosuge, T.; Ohishi, T.; Nishihara, M.; Takahara, A.; Otsuka, H. Mechanophores with a Reversible Radical System and Freezing-Induced Mechanochemistry in Polymer Solutions and Gels. *Angew. Chemie Int. Ed.* **2015**, *54*(21), 6168–6172.

(5) Chen, Y.; Spiering, A. J. H.; Karthikeyan, S.; Peters, G. W. M.; Meijer, E. W.; Sijbesma, R. P. Mechanically Induced Chemiluminescence from Polymers Incorporating a 1,2-Dioxetane Unit in the Main Chain. *Nat. Chem.* **2012**, *4*(7), 559–562.

(6) Gossweiler, G. R.; Hewage, G. B.; Soriano, G.; Wang, Q.; Welshofer, G. W.; Zhao, X.; Craig, S. L. Mechanochemical Activation of Covalent Bonds in Polymers with Full and Repeatable Macroscopic Shape Recovery. *ACS Macro Lett.* **2014**, *3*(3), 216–219.

(7) Piermattei, A.; Karthikeyan, S.; Sijbesma, R. P. Activating Catalysts with Mechanical Force. *Nat Chem* **2009**, *1*(2), 133–137.

(8) Ramirez, A. L. B.; Kean, Z. S.; Orlicki, J. A.; Champhekar, M.; Elsakr, S. M.; Krause, W. E.; Craig, S. L. Mechanochemical Strengthening of a Synthetic Polymer in Response to Typically Destructive Shear Forces. *Nat. Chem.* **2013**, 5(9), 757.

(9) Chen, Z.; Mercer, J. A. M.; Zhu, X.; Romaniuk, J. A. H.; Pfattner, R.; Cegelski, L.; Martinez, T. J.; Burns, N. Z.; Xia, Y. Mechanochemical Unzipping of Insulating Polyladderene to Semiconducting Polyacetylene. *Science* (80) **2017**, *357*(6350), 475–479.

(10) Larsen, M. B.; Boydston, A. J. "Flex-Activated" Mechanophores: Using Polymer Mechanochemistry to Direct Bond Bending Activation. *J. Am. Chem. Soc.* **2013**, *135*(22), 8189–8192.

(11) Park, I.; Sheiko, S. S.; Nese, A.; Matyjaszewski, K. Molecular Tensile Testing Machines: Breaking a Specific Covalent Bond by Adsorption-Induced Tension in Brushlike Macromolecules. *Macromolecules*. **2009**, *42*(6), 1805–1807.

(12) Klukovich, H. M.; Kean, Z. S.; Iacono, S. T.; Craig, S. L. Mechanically Induced Scission and Subsequent Thermal Remending of Perfluorocyclobutane Polymers. *J. Am. Chem. Soc.* **2011**, *133*(44), 17882–17888.

(13) Lee, C. K.; Davis, D. A.; White, S. R.; Moore, J. S.; Sottos, N. R.; Braun, P. V. Force-Induced Redistribution of a Chemical Equilibrium. *J. Am. Chem. Soc.* **2010**, *132*(45), 16107–16111.

(14) Wang, Q.; Gossweiler, G. R.; Craig, S. L.; Zhao, X. Cephalopod-Inspired Design of Electro-Mechano-Chemically Responsive Elastomers for on-Demand Fluorescent Patterning. *Nat. Commun.* **2014**, *5* (May), 4899.

(15) Hofmann, M. 3D Printing Gets a Boost and Opportunities with Polymer Materials. *ACS Macro Lett.* **2014**, *3* (4), 382–386.

(16) Peterson, G. I.; Larsen, M. B.; Ganter, M. A.; Storti, D. W.; Boydston, A. J. 3D-Printed Mechanochromic Materials. *ACS Appl. Mater. Interfaces* **2015**, *7*(1), 577-583.

(17) Peterson, G. I.; Yurtoglu, M.; Larsen, M. B.; Craig, S. L.; Ganter, M. A.; Storti, D. W.; Boydston, A. J. Additive Manufacturing of Mechanochromic Polycaprolactone on Entry-Level Systems. *Rapid Prototyp. J.* **2015**, *21*(5), 520–527.

(18) Larsen, M. B.; Boydston, A. J. Successive Mechanochemical Activation and Small Molecule Release in an Elastomeric Material. *J. Am. Chem. Soc.* **2014**, *136*(4), 1276–1279.

(19) Lee, J.-Y.; An, J.; Chua, C. K. Fundamentals and Applications of 3D Printing for Novel Materials. *Appl. Mater. Today* **2017**, *7*, 120–133.

(20) Wallace, J.; Wang, M. O.; Thompson, P.; Busso, M.; Belle, V.; Mammoser, N.; Kim, K.; Fisher, J. P.; Siblani, A.; Xu, Y.; Welter, J. F.; Lennon, D. P.; Sun, J.; Caplan, A. I.; Dean, D. Validating Continuous Digital Light Processing (CDLP) Additive Manufacturing Accuracy and Tissue Engineering Utility of a Dye-Initiator Package. *Biofabrication* **2014**, *6*(1), 015003.

(21) Bohle, M.; Borzilleri, R. M.; Döpp, D.; Döpp, H.; Herr, R. J. Science of Synthesis: Houben-Weyl Methods of Molecular Transformations. *Georg Thieme Verlag*., **2014**.

(22) Thrasher, C. J.; Schwartz, J. J.; Boydston, A. J. Modular Elastomer Photoresins for Digital Light Processing Additive Manufacturing. *ACS Appl. Mater. Interfaces* **2017**, *9*(45), 39708-39716.

(23) Peterson, G. I.; Schwartz, J. J.; Zhang, D.; Weiss, B. M.; Ganter, M. A.; Storti, D. W.; Boydston, A. J. Production of Materials with Spatially-Controlled Cross-Link Density via Vat Photopolymerization. *ACS Appl. Mater. Interfaces* **2016**, *8*(42), 29037–29043.

(24) Deshpande, V. S.; Fleck, N. A.; Ashby, M. F. Effective Properties of the Octet-Truss Lattice Material. *J. Mech. Phys. Solids* **2001**, *49*(8), 1747-1769.

(25) Schoen, A. H. Infinite Periodic Minimal Surfaces without Self-Intersections. *Nasa* **1970**.

Chapter 3. Additive Manufacturing with Mechanochromic Spiropyran for Strain Sensing in Complex Three-dimensional Geometries

3.1 Introduction

Spiropyran (SP) was found to be photochromic in 1960s and has been widely used in light-responsive dynamic materials, which have the potential to be used as photoswitches or for chemical sensing[1]. By irradiating the UV light on it, the SP can undergo the ring opening process to its colored form merocyanine. This photochromic behavior is reversible and the purple colored merocyannie can switch back to SP under visible light. Moore group found its mechanochromic behavior in 2009 by applying tensile force on the polymeric material with SP covalently bonded to isomerize the molecule, presenting purple color in response to forces[2]. The mechanism for this process is that when applying forces on polymers with SP incorporated, the mechanical loads is transmitted along the polymer chains to reach the site of SP and break the liable spiro C-O bond to trigger the isomerization. This unique mechanochemical reactivity of SP makes it the star mechanophore which is most widely studied in this field, including the fundamental mechanism of the mechanoactivation[3], the methods to enhance the activation of the mechanophore or realize early onset activation of the mechanophore[4], their applications for force-sensing and damage reporting[5], and so on. Our group previously studied the possibility of filamentizing polycaprolactone (PCL) with SP and utilized the functional filaments for melt material extrusion (MME) 3DP[6]. The capability of 3DP enables the rapid fabrication of the prototypes that can be impossible or difficult to make by traditional manufacturing techniques. By combining the photo-

and mechano- responsiveness of SP and advanced 3DP technique, we fabricated samples that were dually responsive systems involving the previously described photochromism and mechanochromism. Printed specimens with segregated photochromic and mechanochromic regions were fabricated by alternating deposition of the two stimuli-responsive materials with a multi-material MME printer. The spatially controlled regions can be activated by UV light or mechanical impetus selectively.

However, making filaments is a time-consuming process involved in MME 3DP, which contains high temperature process that may cause the degradation of SP. Additionally, it is hard to manufacture complex geometries with fine structures and high resolutions by using MME 3DP. Therefore, we consider using a more versatile and easily accessible 3DP technique, digital light processing (DLP) 3DP, to photochemically incorporate mechanochemical moieties by mixing liquid photocurable resins and methacrylate-functionalized SP together. During the crosslinking process induced by visible light irradiation, the SP moiety can be covalently bonded to acrylate monomers to form polymer networks. In this way, the SP can be used as a qualitative strain probe to transfer the invisible localized strain distribution information to visible signals on the 3D printed complex geometries, which is critical in manufacturing industry. It also provides the advantages over the regular computer modelling on the strain field simulation in complex structures by showing the in-situ color change precisely.

3.2 Results and Discussion

2-hydroxyethyl acrylate (HEA) and butyl acrylate (BA) were chosen to be photocurable resins for DLP printing since our previous study showed the superb mechanical properties of these materials and their excellent 3D printability. Spiropyran dimethacrylate (SP-DMA) was

synthesized and mixed with HEA and BA monomers at certain ratio. To confirm printability of the mixture, we printed dogbone tensile test specimens (dimensions: 63.50 mm × 9.53 mm × 3.20 mm) with the following weight ratios of HEA/BA: 20/80, 35/65, 50/50, 65/35, 80/20. 0.3 wt% SP-DMA as crosslinker and 0.5 wt% irgacure 819 as photoinitiator was added into each system. The mechanical properties of the printed specimens were tested by Instron 5585H Universal Testing System. As shown in Fig.3.1, all of the printed samples have elongation at break over 400% elongation, indicating great ductility of the material. Additionally, the samples can recover back to their original shapes after the force was removed, showing the potential to be used for strain mapping from the mechanochemical reactivity of SP. Young's modulus was calculated and shown in Fig.3.1, exhibiting that the modulus was increased with the HEA amount in the system. The glass transition temperatures (Tg) of the 3D printed materials were measured by Differential Scanning Calorimetry (DSC). As shown in table 3.1, the Tg of the polymer networks with different composition are all below room temperature (25 ^{o}C), which is consistent with the stress-strain curves showing the elastomeric properties of the materials. And the Tg increased from -61.77 ^{o}C to -3.87 ^{o}C as the HEA amount in the system increased from 0 wt% to 100 wt%. This enhancement of Tg might result from the high polarity of HEA due to the hydroxy group and the hydrogen bondings formed between HEA molecules.

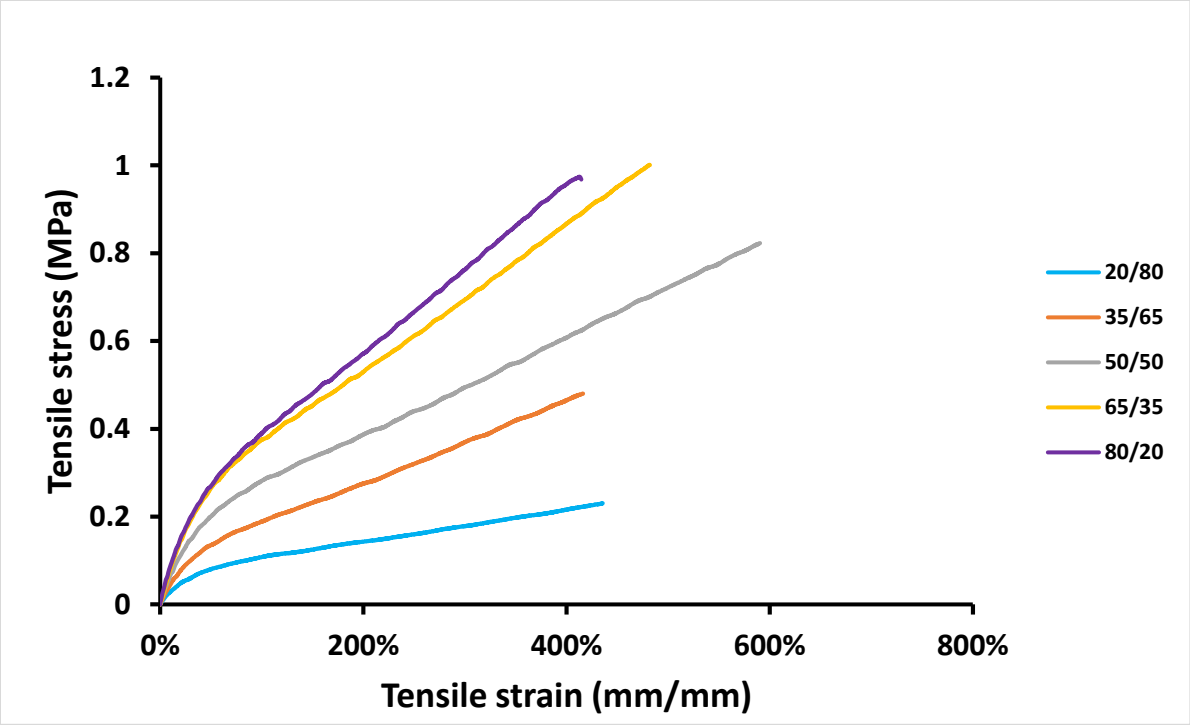

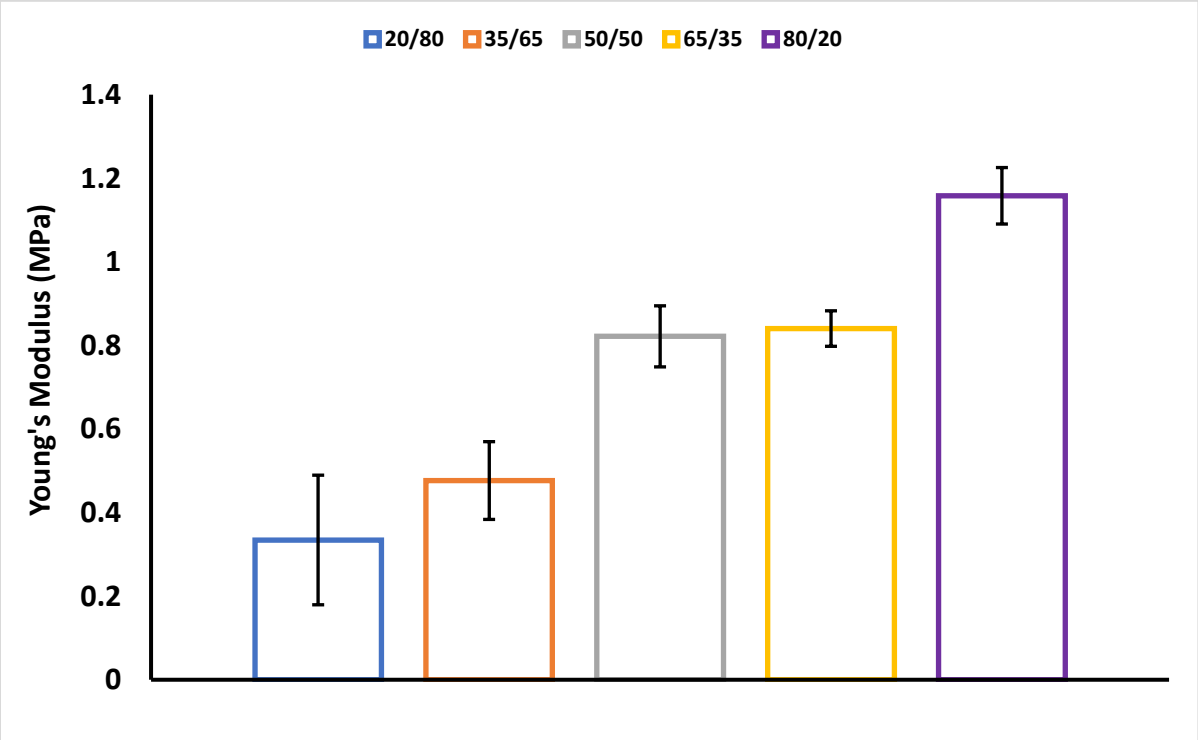

Figure 3.1 Top: tensile stress-strain curves for HEA/BA/SP systems; Bottom: Calculated Young's modulus for HEA/BA/SP systems; Ratios indicate the weight ratio of HEA and BA; Error bars represent standard deviation over three samples.

Table 3.1 Glass transition temperature for HEA/BA/SP systems; Ratios indicate the weight ratio of HEA and BA; SP-MA amount is 0.3 wt% in each system.

Composition (HEA/BA)	0/100	20/80	35/65	50/50	65/35	80/20	100/0
Tg (°C)	-61.77	-38.55	-33.41	-29.28	-21.59	-15.57	-3.87

Unfortunately, there was no color change observed during the tensile test of the dogbone samples. Therefore, 3D printed complex geometries that can be compressed by load frame was made for testing the mechanochromic effect since compression can generate force in all directions rather than uniaxial force in tensile tests. Octet truss unit cells (exterior dimensions: 14.66 mm × 14.66 mm ×14.66 mm) were printed at 14000ms layer cure time for each HEA/BA/SP system. Printed octet truss unit cells with low amount of HEA experienced some structural weakness as shown in Fig.3.2. This structural weakness decreased with the increase of HEA component in the system, which is in consistence with the mechanical properties of different resin formulations. This results from the fact that HEA contains around 9 wt% oligo (ethylene glycol) diacrylates as crosslinker[5]. In addition, the intensive hydrogen bondings in HEA also contribute to the printing quality of the octet truss.

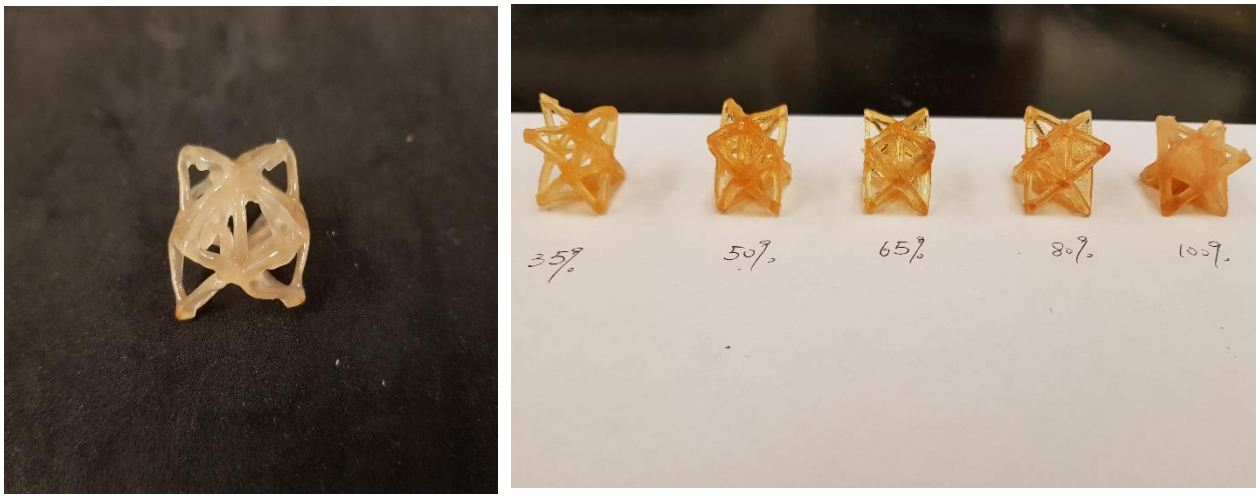

Figure 3.2 Left: Octet truss unit cell printed with HEA/BA 20/80 system; Right: Printed octet truss unit cells. Percentage indicates the weight percent of HEA in the resins.

By mechanically loading the printed octet truss unit cells (HEA/BA 35/65) to certain strain, slight color deepening was observed in the compressed objects, indicating the activation of SP happening during this process. Further increasing the compressive strain to more than 90%, the samples could recover back to their original shape within several minutes with the purple color on the joints and junctions after the load was removed, as shown in Fig.3.3. This is because the joints and connections experience higher localized strain when compressing the structs together than other areas, which leads to the activation of SP. Similar results were also observed in printed gyroid lattice (Fig.3.4). SP in certain areas was activated, suggesting high localized strain distributed in those areas. We then compressed the octet truss unit cell with different compositions (HEA/BA 35/65, 65/35, and 80/20) to maximum strain (near 100%) and found out the best color change happened in the samples with 35 wt % HEA, as shown in Fig.3.5. One possible reason for this is that the polarity of HEA opens the ring of SP partially in samples with high HEA content. Therefore, the ring opening resulted from mechanical load is not very obvious compared to the system with lower HEA amount. The capability of this mechanochromic photocurable system

gives them the potential to be used as force sensors to exhibit localized stress/strain distribution as an easily visible signal in sophisticated structures which may be hard to characterize or simulate.

Figure 3.3 Left: Octet truss unit cell printed with HEA/BA 35/65 system; Right: Compressed octet truss unit cell.

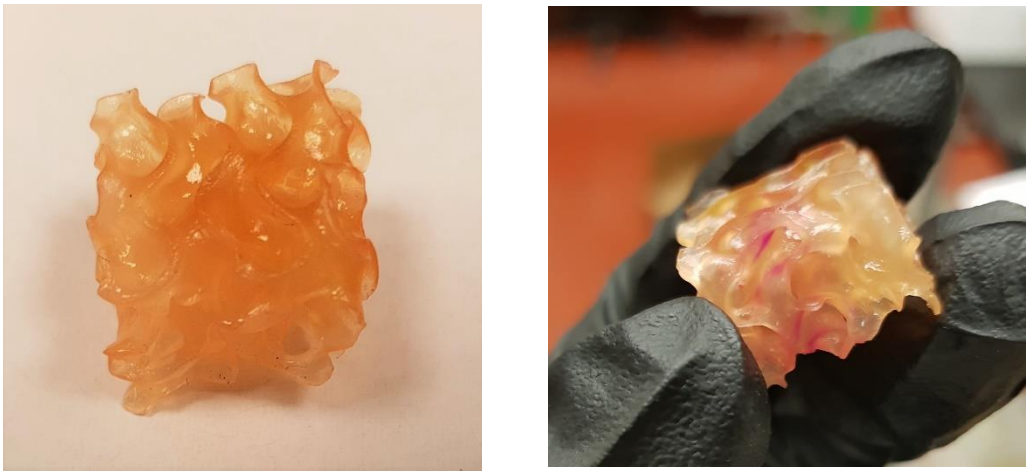

Figure 3.4 Left: Gyroid lattice printed with HEA/BA 35/65 system; Right: Compressed gyroid lattice.

Figure 3.5 Left: Compressed octet truss unit cell printed with HEA/BA 35/65 system to near 100% strain; Right: Compressed octet truss unit cell printed with HEA/BA 65/35 system (left) and HEA/BA 80/20 system (right) to near 100% strain.

3.3 Conclusion

In conclusion, we prepared DLP printable photoresins that can be 3D printed successfully to mechanochromic objects. The tensile tests on printed dogbone samples showed good mechanical properties of the material with the increased Young's modulus as the amount of HEA increased in the system. DSC analysis also showed the increased Tg with HEA content. Complex geometries such as octet truss unit cells and gyroid lattice were printed and compressed. Joints and connections on octet truss unit cells exhibited purple color due to the concentration of localized strain in those areas. This method opens a new way to directly "read" the localized strain in a qualitative manner, which provides insights to assess the force distribution on complex structures.

3.4 Experimental

3.4.1 Materials and Equipment

The synthesis and characterization procedure of spiropyran-dimethacrylates (SP-DMA) was as reported below. ^{1}H NMR spectra were obtained from the Burke AVance 301 MHz or 500 MHz spectrometers. Light intensity of the projector used for 3D printing was measured using an Extech Instruments light meter (model HD450). Thermogravimetric analysis (TGA) was performed on a TA TGA Q50 under nitrogen from room temperature to 600 °C at a rate of 5 °C/min. Differential Scanning Calorimetry (DSC) was performed on a TA DSC Q250 calorimeter under nitrogen. Heat flow as watts from the second heating was recorded and reported after normalizing by mass of the sample (W/g). The thermal profile for DSC is as follows: the sample was heated from -90°C to 100°C at a rate of 10°C/min and then cooled to -90°C at a rate of 5°C/min; the second was to heat the sample from -90°C to 50°C at a rate of 10°C/min and then cooled to -90°C at a rate of 5°C/min; the final ramp was to heat the sample to 50°C at a rate of 5°C/min. Compression tests and tensile tests were conducted by an Instron 5585H Universal Testing System at a rate of 20 mm/min and Bluehill 3.0 software. An Instron 2663-821 Advanced Video Extensometer was used to measure strain, by tracking the position of two marks made within the specimen's gage region, during elongation on the ASTM D638 type V specimen samples. 2-Hydroxyethyl acrylate (HEA) and butyl acrylate (BA) were purchased from ACROS Organics. Bis(2,4,6-trimethylbenzoyl)-phenylphosphineoxide (Irgacure 819) was purchased from Sigma-Aldrich. All chemicals were used as received without additional purification.

3.4.2 Synthesis procedure of spiropyran-dimethacrylate (SP-DMA)

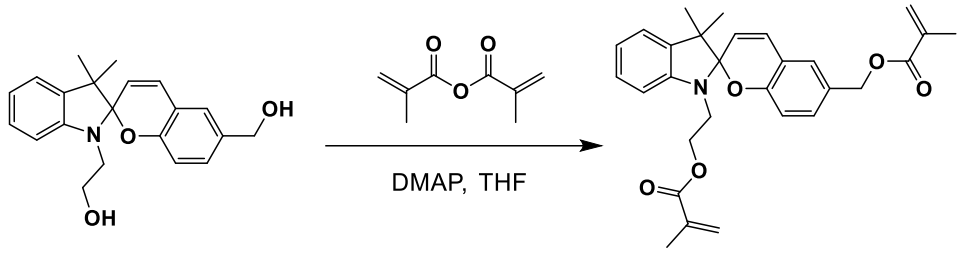

Spiropyran-diol (synthetic procedure reported previously) (1.49 mmol) was added into anhydrous THF with 4-dimethylaminopyridine (DMAP) (1.63 mmol). The mixture was stirred for 15 min. Methacrylic anhydride (3.86 mmol) was then added to the system dropwise. The reaction proceeded for 5 hours and monitored by TLC. The crude product was plugged with basic alumina and washed with DCM. The solution was then rinsed successively with saturated ammonia chloride for 2 times, sodium bicarbonate for 2 times, DI water for 4 times, and brine for 1 time. The solution was dried over $MgSO_4$, filtered and then concentrated under reduced pressure to yield purple oil.

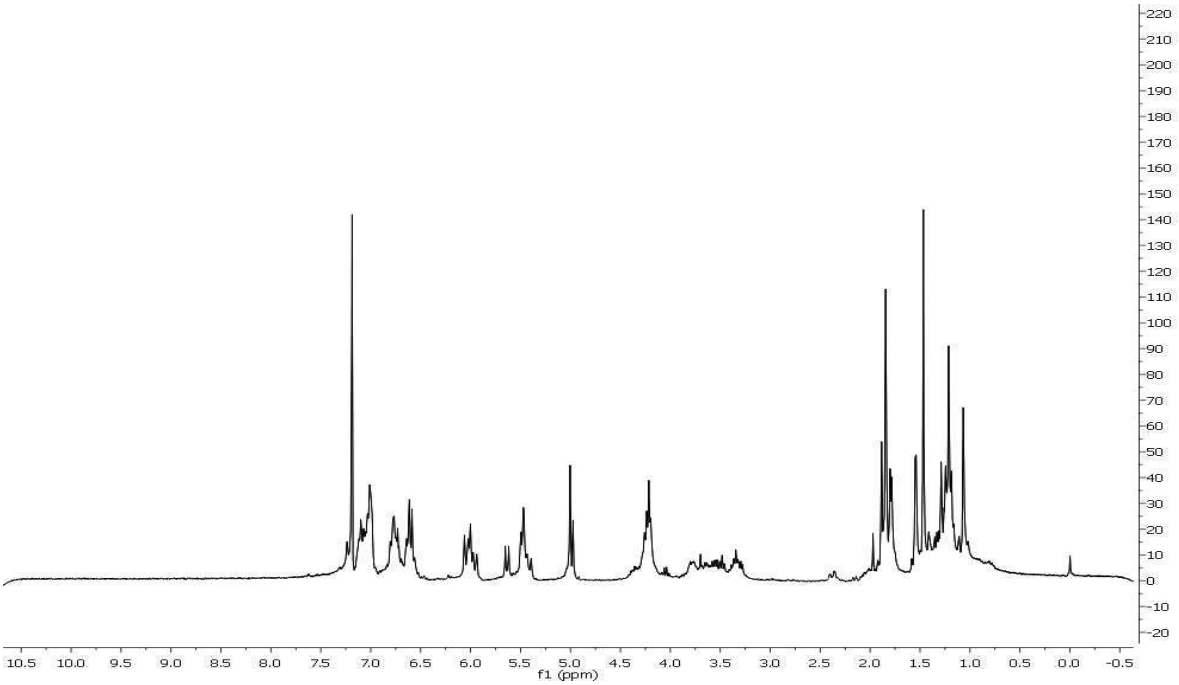

Figure S3.1 ^{1}H NMR spectrum of SP-DMA (solvent=$CDCl_3$).

3.4.3 Preparation of mechanochromic photoresins

The photoresins were prepared by mixing HEA and BA at certain weight ratios (20/80, 35/65, 50/50, 65/35, 80/20) with the total mass of 20 g. 0.06 g of SP-DMA as functional component and 0.1 g of Irgacure 819 as photoinitiator were added into the system in a 20 mL screw cap vial. The resins were sonicated by Branson 1510 sonicator for 30 s before use.

3.4.4 Representative Differential scanning calorimetry (DSC) data

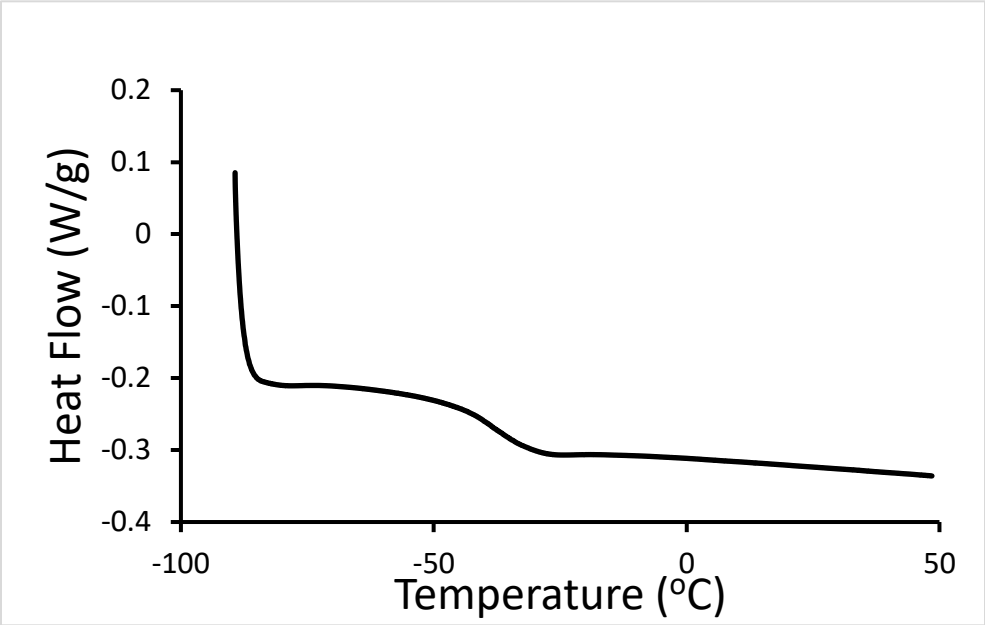

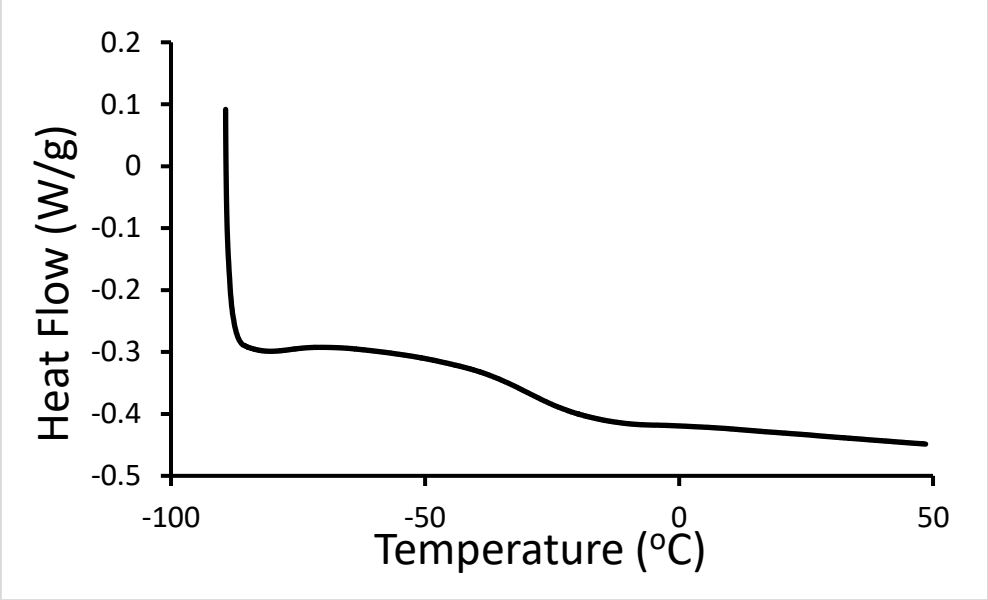

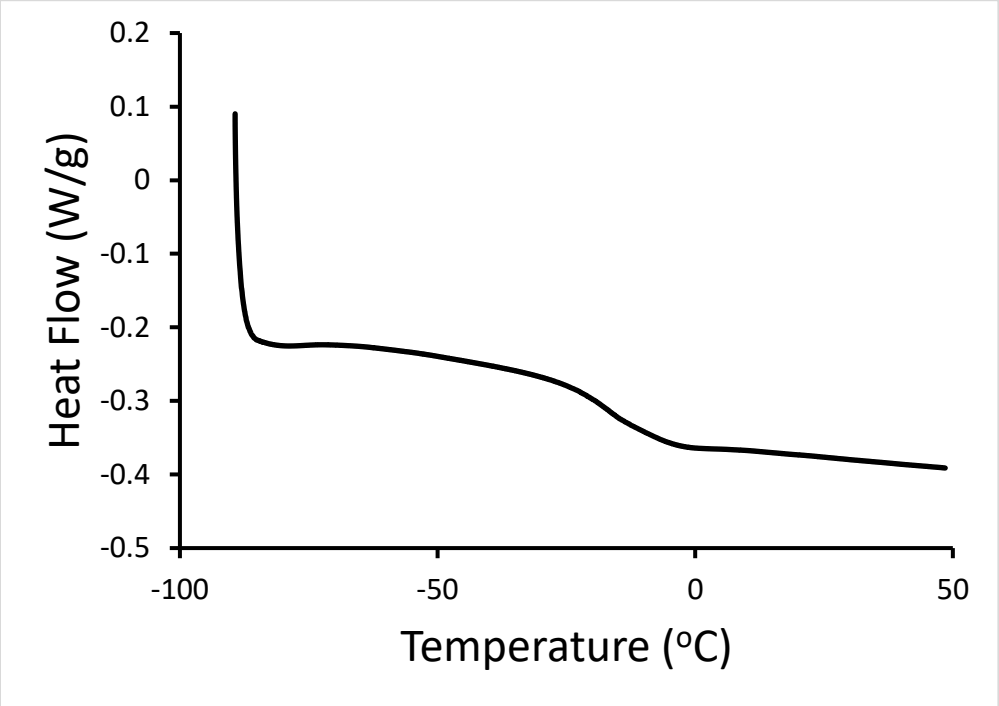

Figure S3.2 DSC data for HEA/BA systems: 35/65 (top), 50/50 (middle), 65/35(bottom). Only the heating cycles from -90°C to 50 °C at a ramp rate of 10 °C/min were shown.

3.5 References

(1) Klajn, R. Spiropyran-Based Dynamic Materials. *Chemical Society Reviews*. **2014**, *43*(1), 148-184**.**

(2) Lin, Y.; Barbee, M. H.; Chang, C. C.; Craig, S. L. Regiochemical Effects on Mechanophore Activation in Bulk Materials. *J. Am. Chem. Soc.* **2018**, *140*(46), 15969-15975.

(3) Li, J.; Shiraki, T.; Hu, B.; Wright, R. A. E.; Zhao, B.; Moore, J. S. Mechanophore Activation at Heterointerfaces. *J. Am. Chem. Soc.* **2014**, *136*(45), 15925-15928.

(4) Zhang, H.; Chen, Y.; Lin, Y.; Fang, X.; Xu, Y.; Ruan, Y.; Weng, W. Spiropyran as a Mechanochromic Probe in Dual Cross-Linked Elastomers. *Macromolecules* **2014**, *47*(19), 6783-6790.

(5) Thrasher, C. J.; Schwartz, J. J.; Boydston, A. J. Modular Elastomer Photoresins for Digital Light Processing Additive Manufacturing. *ACS Appl. Mater. Interfaces* **2017**, *9*(45), 39708-39716.

(6) Peterson, G. I.; Larsen, M. B.; Ganter, M. A.; Storti, D. W.; Boydston, A. J. 3D-Printed Mechanochromic Materials. *ACS Appl. Mater. Interfaces* **2015**, *7*(1), 577-583.

Chapter 4. Mechanochromic PDMS for Visualizable Strain Mapping in Complex Geometries

4.1 Introduction

Stress and strain are critically important in manufacturing industry and our daily life since the stress/strain distribution in objects can affect the lifetime of the material and is crucial for the design of the object geometries to enhance the mechanical properties. Many methods have been used to monitor the stress/strain distribution, including experimental detection and theoretical simulation. However, theoretical modeling is limited when simulating the very complex geometries and predicting the mechanical behavior in flawed material in real life. In addition, most experimental methods are indirect which transform the stress/strain distribution to signals of other forms. For example, magnetic flux leakage and pulsed eddy current coupled with piezoelectric elements transform the internal stress/strain distribution in objects to electric signals[1], which cannot provide direct visualization. Digital image correlation (DIC) is also a fast-developing experimental technique that measures the displacement field and estimates the strain field by comparing the digital images of the deformed samples with the undeformed ones, associated with numerical computing[2]. However, this method is only suitable for objects in two dimension and has very high requirement of the image quality and computer performance. Therefore, it is rarely used on heterogeneous samples. Recently, Tang et al. developed a fluorescent mapping method providing dynamic and direct visualization of stress/strain distribution on metal specimens[3]. Basically, the team applied organic mechanoresponsive luminogen which has high fluorescence contrast in crystalline state and amorphous state as film on metal samples. When stretching the metal sample with the luminogen coated, the crystals of the luminogen were broken to form the

amorphous state that can emit strong green fluorescence. The emission is positively correlated with localized strain so that it can be used as an indicator for strain mapping. However, this method requires high quality charge-coupled device camera (CCD) to capture the fluorescent images and the stress/strain distribution is not directly visible by naked eyes. Additionally, this technique has the limitations in mapping complex geometries and objects in three-dimensions.

Spiropyran (SP) as a widely studied mechano-chromphore has recently been incorporated into polydimethylsiloxane (PDMS) to make mechanochromic elastomers[4]. Inspired by the great ability of recovery and obvious color change when stressed, we considered to use the SP-PDMS system for strain mapping in which case the localized strain can be correlated to the intensity of blue color during stretching. Because of the easiness of fabrication, the SP-PDMS can be manufactured to highly complex geometries by taking advantage of sophisticated 3D printing technique. In this way, the localized stress/strain distribution for the complex geometries that is very difficult to be simulated or detected can be seen directly by naked eyes.

4.2 Results and Discussion

Before fabricating complex geometries with SP-PDMS system, we first examined the compatibility of SP in PDMS matrix. The SP-diol molecules were functionalized with 4-pentenoic anhydride (procedure in SI) and then covalently bonded into P-60 PDMS. To find the best material system with both excellent mechanochromic behavior and mechanical properties that are suitable for further strain mapping study, we screened three SP-PDMS systems with weight ratios of SP to be 0 wt%, 0.6 wt%, 1.2 wt% respectively. SP was mixed with P-60 and its curing agent (20:1 w:w) together and then cured at 60 ^{o}C for 30 min. The resulting crosslinked material was tested by rheometer for its storage modulus and loss modulus. As shown in Fig.4.1, the storage modulus and

loss modulus of the SP-PDMS systems decreased from 0.431MPa to 0.0865MPa at 0.01% oscillation strain as the SP amount increased from 0 wt% to 1.2 wt%, which is in consistence with the fact the material felt soft and sticky with high SP concentration. The tensile stress-strain curves (Fig.4.1) also showed the decreased modulus in 0.6 wt% and 1.2 wt% SP systems compared with pure PDMS. Further increasing the SP amount in PDMS will lead to the undercured material with poor mechanical properties. Therefore, we chose 0.6 wt% system for our study since this system showed good color change when stressed as well as good mechanical properties.

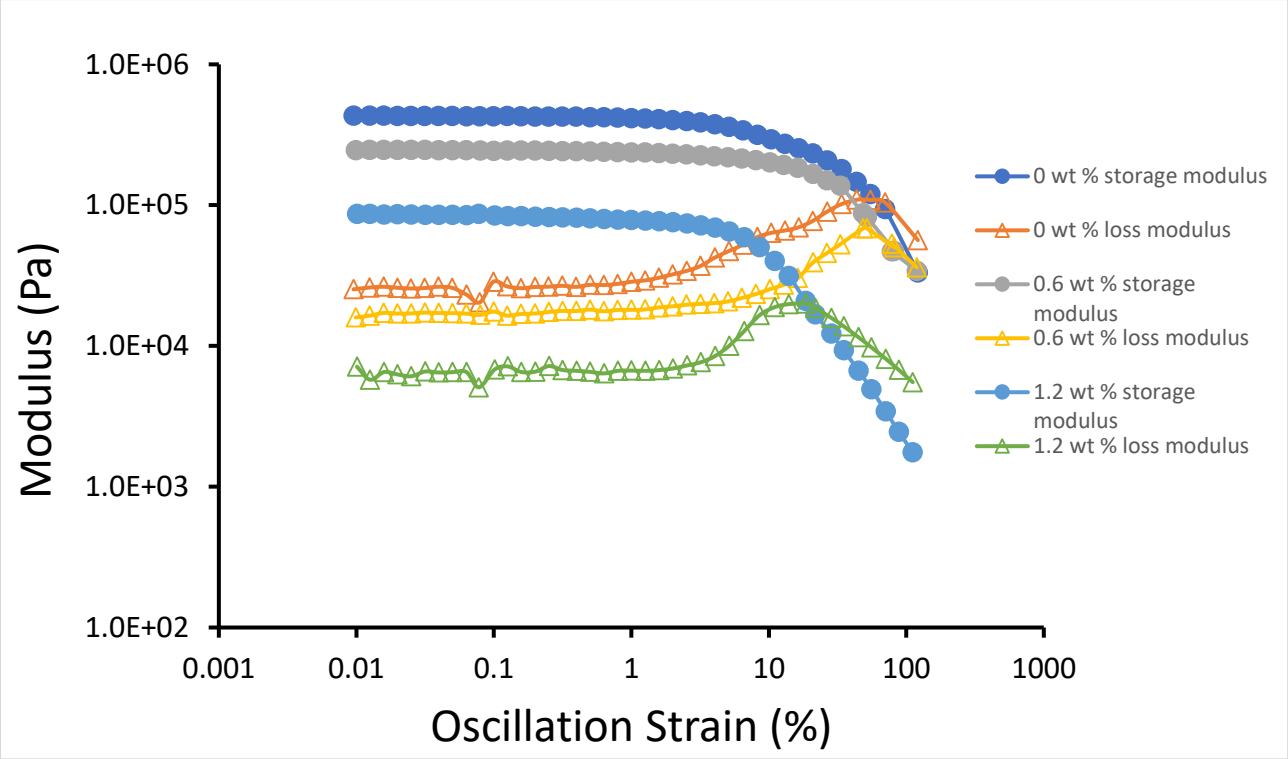

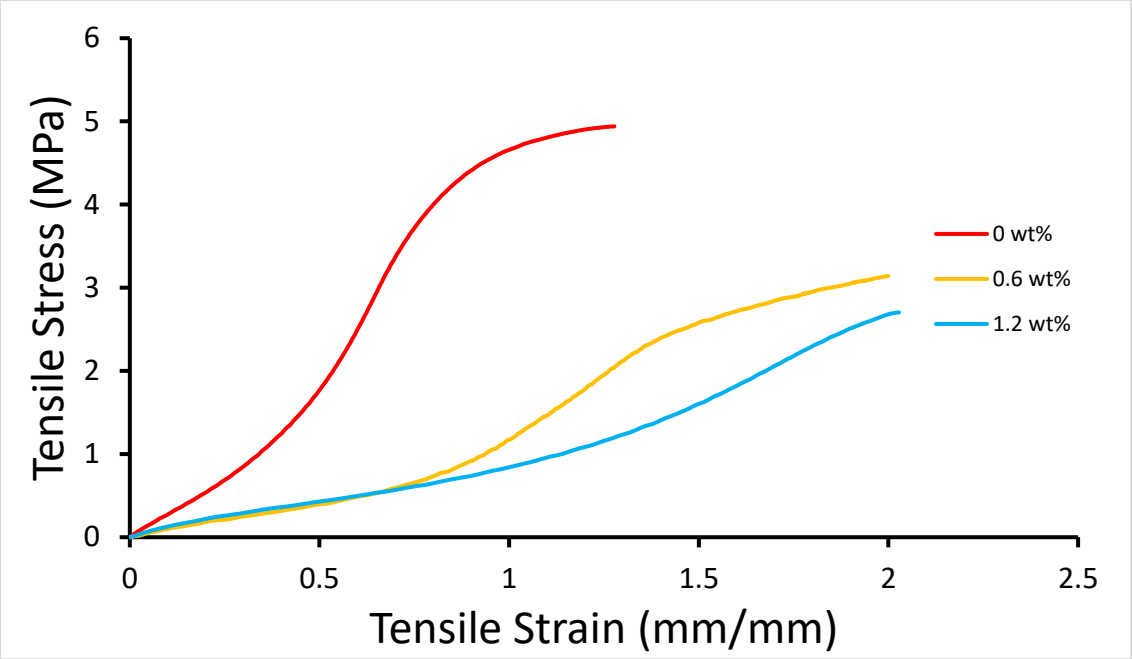

Figure 4.1 Top: Storage modulus and loss modulus for SP-PDMS system with different SP content; Bottom: Stress-strain curves for SP-PDMS system with different SP content. Strain rate: 7mm/min.

3D printing technology was used to create Acrylonitrile Butadiene Styrene (ABS) molds with different patterns by using a commercially available melt material extrusion (MME) printer. The SP, PDMS base and curing agent were mixed together and poured onto the 3D printed molds to form lattice structure with complex geometries at elevated temperature. The SP-PDMS sheets were then stretched by using an Instron 5585H Universal Testing System at a speed of 7mm/min. Images were captured by a digital single-lens reflex (DSLR) camera at an interval of 4s. Fig.4.2 exhibits the images of prepared sheet with a hole in the middle. The left image in Fig.4.2 is the unstretched sheet clamped by the grippers. By stretching it to around 120% global strain, clear blue color (originated from the high energy merocyanine) was observed on the sheet (Fig.4.2 middle), suggesting the activation of SP in the material system. Specifically, the areas around the hole in the horizontal direction showed the most intense blue color while the areas around the hole

in the vertical direction did not have much color change. This difference was resulted from the different local strain distribution. The area with more accumulated localized strain could active more SP. Therefore, more intense blue corresponds to higher localized strain.

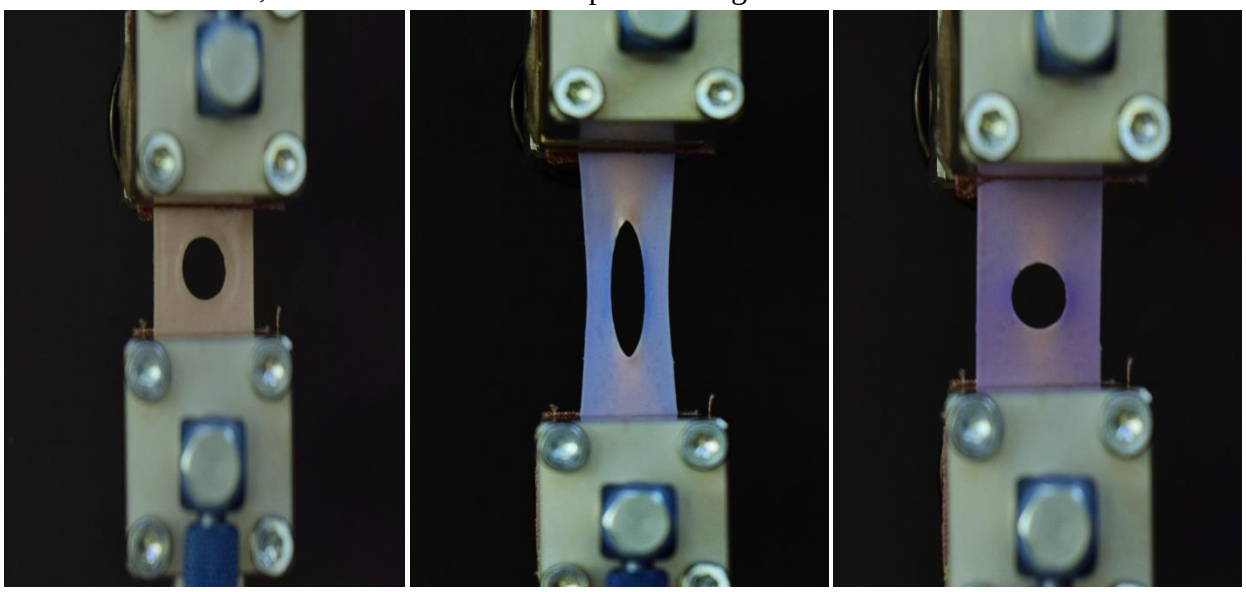

Figure 4.2 Images for tensile tests on SP-PDMS hole lattice. Left: unstretched state; Middle: stretched state at 120% global strain; Right: relaxed state.

In this way, the invisible stress/strain distribution is transformed to visible signals that can be detected by naked eyes. After removing the force, the sheet can recover back to its original shape with the blue color turned to purple (originated from low energy merocyanine). The intensity of the purple marks on the sheet was consistent with the blue color in stretched state and could be used for further investigations on the recoverable elastomers.

By taking advantage of the capability of the SP-PDMS composite for mapping localized strain, we fabricated some geometries with sharp corners to study their strain distribution. As can be seen in Fig.4.3, after stretching the triangular pattern to around 120% global strain, very intense blue color was shown at the location of two base angles, indicating high localized strain in these

areas. Similarly, the star pattern exhibited intense blue color at sharp corners too, especially at the top two angles. These results suggested that the strain accumulated mostly around sharp corners in the patterns, which might lead to fracture in those areas if stretched more.

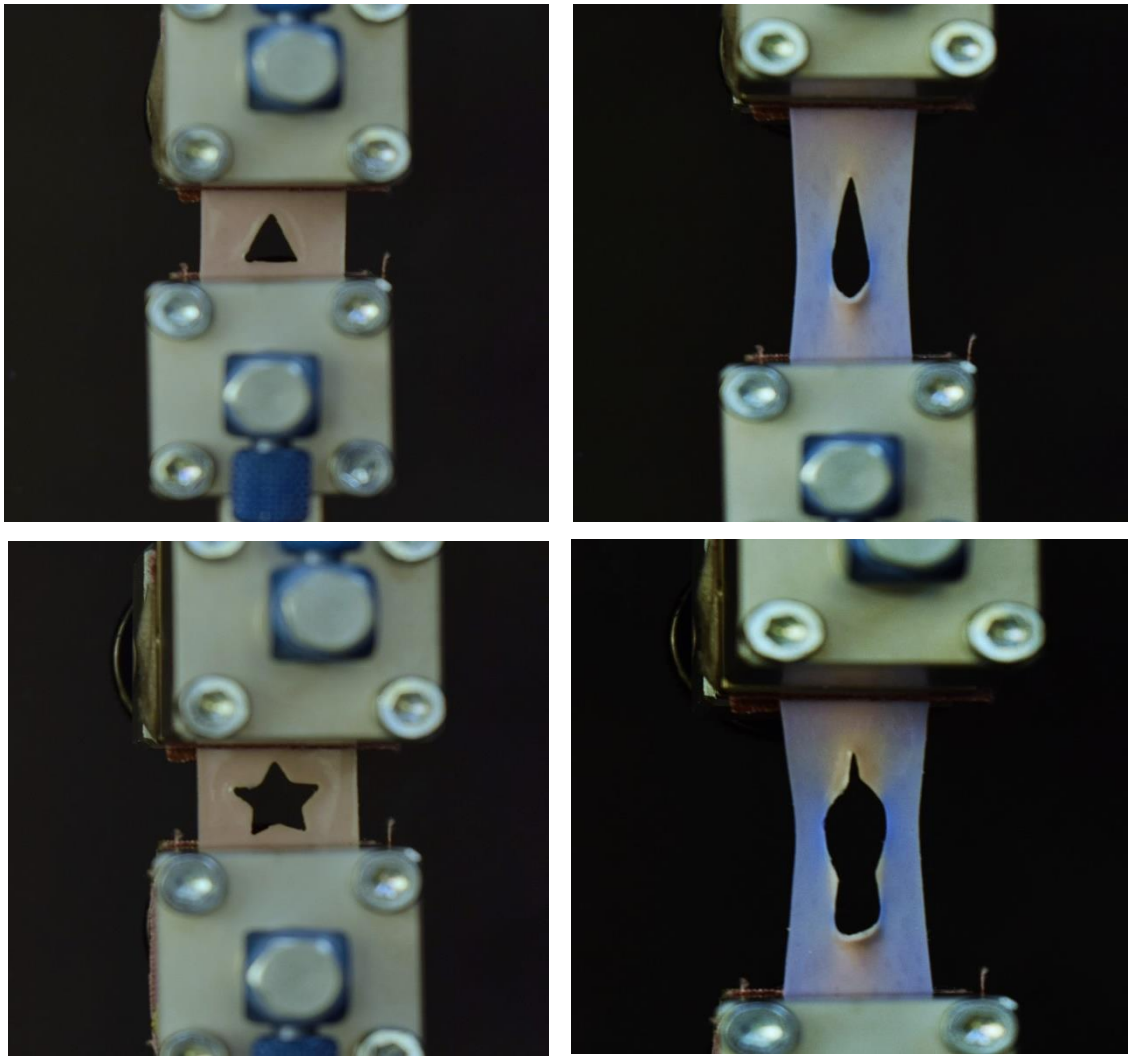

Figure 4.3 Top: images for tensile tests on SP-PDMS triangle lattice. Left: unstretched state; Right: stretched state at around 120% global strain. Bottom: images for tensile tests on SP-PDMS star lattice. Left: unstretched state; Right: stretched state at around 140% global strain.

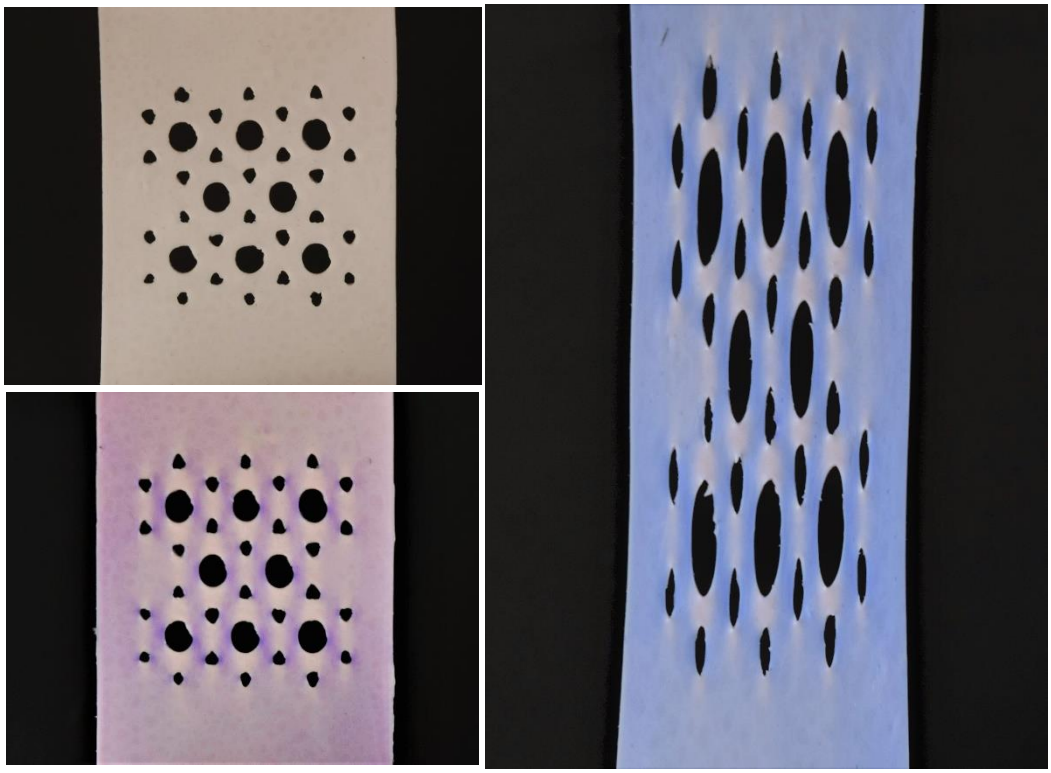

Figure 4.4 Left: Top: complex lattice in unstretched state. Bottom: complex lattice in relaxed state; Right: complex lattice in stretched state at around 110% global strain.

The strain distribution on lattice structures with very complex geometries was also investigated. The lattice structures, including periodic porous structure, kagome lattice, and orthogonal ellipse lattice, were very hard to be fabricated by using conventional manufacturing techniques. However, 3D printing can be used to create molds for these lattice structures by simply arranging the simple structures in the computer model. For example, the complex lattice composed of periodic circles and surrounded triangles was fabricated using SP-PDMS system were stretched as shown in Fig.4.4. The top left image showed the patterned lattice. It was then stretched to around 110% global strain, as indicated in the right image. Similar as the simple structures, the intense blue color distributed around each hole in the horizontal direction, as well as the two base angles

of each triangle. When the force was released, the sheet went back to its original shape, leaving the wave-like purple marks. As shown in the bottom left image, the localized strain distribution of the complex geometries was the assembly of the simple structures, that is the deepest purple color existed in the same locations as in the simple triangles and holes. Additionally, there were synergetic effects observed between the holes and triangles, activating SP in some of the areas that was not activated in the simple structures. Therefore, the SP-PDMS system provided an easily accessible method to measure the localized strain distribution qualitatively.

To get more detailed investigation on the strain field of patterned lattice, we used MATLAB to process the images and employed RGB color space to plot imagemaps in the program. In detail, the B values (blue) on each pixel in the image were extracted and normalized by the light intensity (R+G+B value) and then plotted. As can be seen in Fig.4.5, the middle image is the imagemap of the left image with the color bar shown on the right side of that image. Clearly, the imagemap showed the same results as the original picture where the highest localized strain existed around the holes in the horizontal direction and it provided a more distinguishable color chart for showing the local strain difference. Additionally, this method gave more details than regular computer modeling. As shown in the first two images in Fig.4.5, the area in the purple box has highest localized strain which may result from some defects in the material. By further stretching the PDMS sheet, it actually broke at the area with most strain accumulated, as shown in the right image in Fig.4.5. This method outperforms the computer modeling which has limitation on

simulating tiny defects in the objects because it provides signals on where the crack will happen before the objects are actually failed, which is very critical in manufacturing industry.

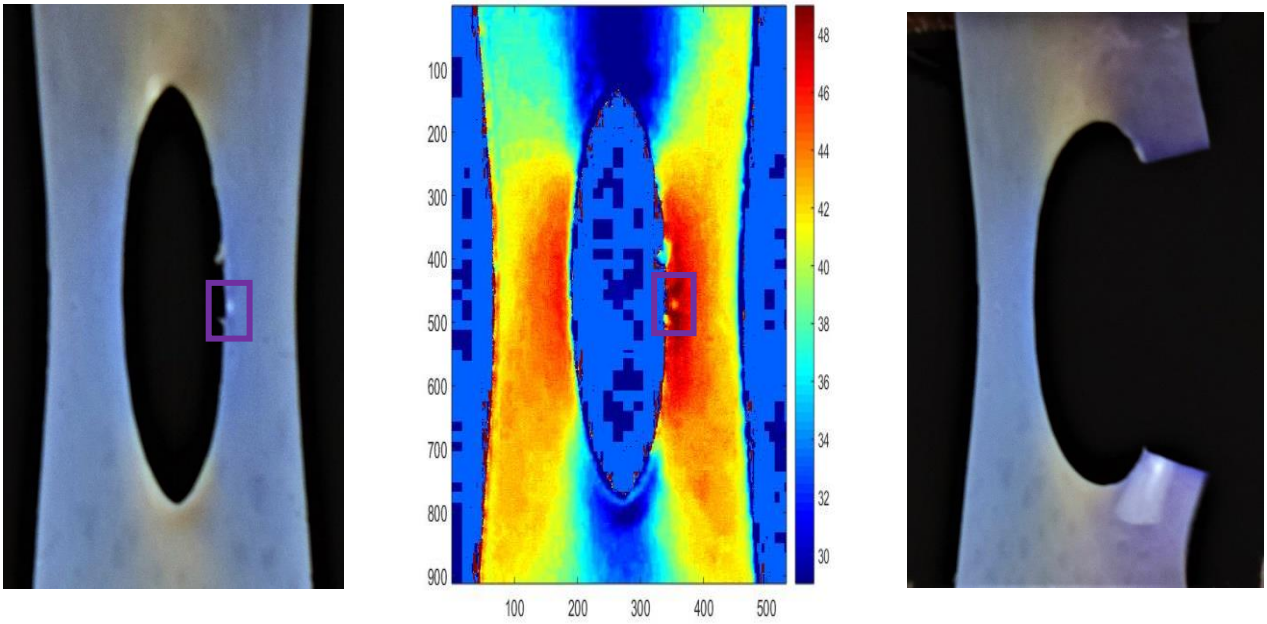

Figure 4.5 Left: Stretched circle lattice just before broken. Middle: Imagemap of the left picture plotted by MATLAB, the bar on the right is color bar; Right: Image of the same circle lattice after broken.

The imagemaps can also be applied on complex geometries to give clear mapping of strain field with better color contrast. The raw image and the plotted imagemap were shown in Fig.4.6. The areas between the holes and triangles exhibited blue color in the imagemap, indicating low localized strain which was in consistence with the white areas in the raw image. On the other hand, the brown area around the holes and triangles in the imagemap corresponds to the deepest blue in the raw image, suggesting high localized strain.

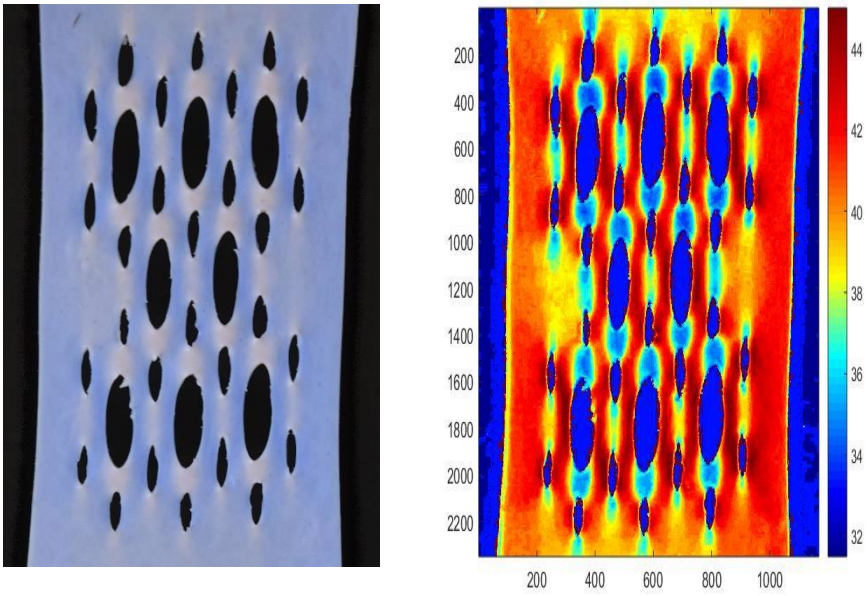

Figure 4.6 Left: Raw image of stretched complex lattice. Right: Imagemap of the left picture plotted by MATLAB, the bar on the right is color bar.

4.3 Conclusion

In summary, we tested the mechanical properties of SP-PDMS system with different SP content and found out the system with 0.6 wt% SP is optimal for great mechanical properties and obvious color change when stressed. We then fabricated SP-PDMS sheets with different lattice structure, from simple to complex, by using 3D printed molds and mechanically stretched them

with images captured. The localized strain distribution was illustrated by the intensity of blue color on the sheet because more SP was activated in high strain areas. All the elastomeric sheets could recover back to their original shape after the force was removed with the purple marks showing the force distribution. The imagemaps were plotted based on the RGB values on each pixel and provided mapping of the strain field with better color contrast. The imagemaps also had more advantages than regular computer modeling on predicting the crack propagation in advance. This mechanochromic elastomer system enables the real-time, on-site, dynamic mapping of strain on objects, which opens a new avenue for evaluating the local strain distribution by naked eyes.

4.4 Experimental

4.4.1 Materials and Equipment

The synthesis and characterization procedure of pentenoate-functionalized spiropyran was as reported below. ^{1}H NMR spectra were obtained from the Burke AVance 301 MHz or 500 MHz spectrometers. Tensile tests were conducted by an Instron 5585H Universal Testing System at a rate of 7 mm/min and Bluehill 3.0 software. Rheology measurements were taken on a TA Instruments Discovery HR-2 hybrid rheometer using a stainless steel 20 mm Peltier plate. Data was collected from a strain sweep test from 10 to 50 000 Pa at 25 °C and an angular frequency of 6.28 rad/s. Melt material extrusion 3D printing was performed on Flashforge Dreamer 3D Printer. P-60 PDMS was purchased from Silicones, Inc. 4-pentenoic anhydride was purchased from Sigma-Aldrich. All chemicals were used as received without additional purification.

4.4.2 Synthesis procedure of pentanoate-functionalized spiropyran

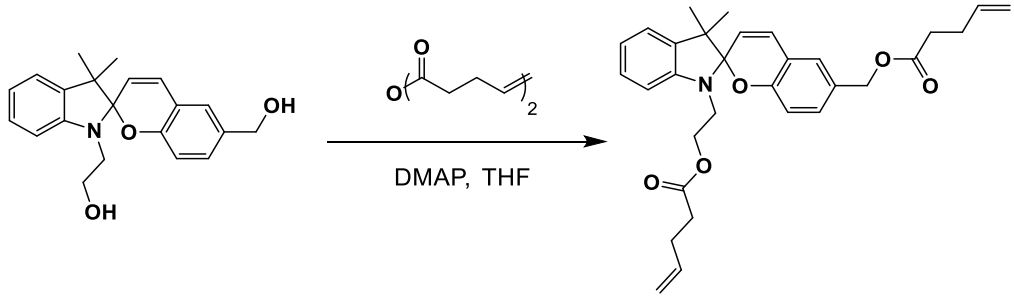

Spiropyran-diol (synthetic procedure reported previously) (0.59 mmol) was added into anhydrous THF with 4-dimethylaminopyridine (DMAP) (1.06 mmol). The mixture was stirred for 15 min. 4-pentenoic anhydride (1.53 mmol) was then added to the system dropwise. The reaction proceeded for 4 hours and then quenched with 0.8 mL methanol. The crude product was put through an alumina plug and washed with dichloromethane. The solution was then washed sequentially with

sodium bicarbonate for three times, water for two times, brine for one time, and dried over magnesium sulfate. The solution was filtered and concentrated under reduced pressure to yield dark purple oil.

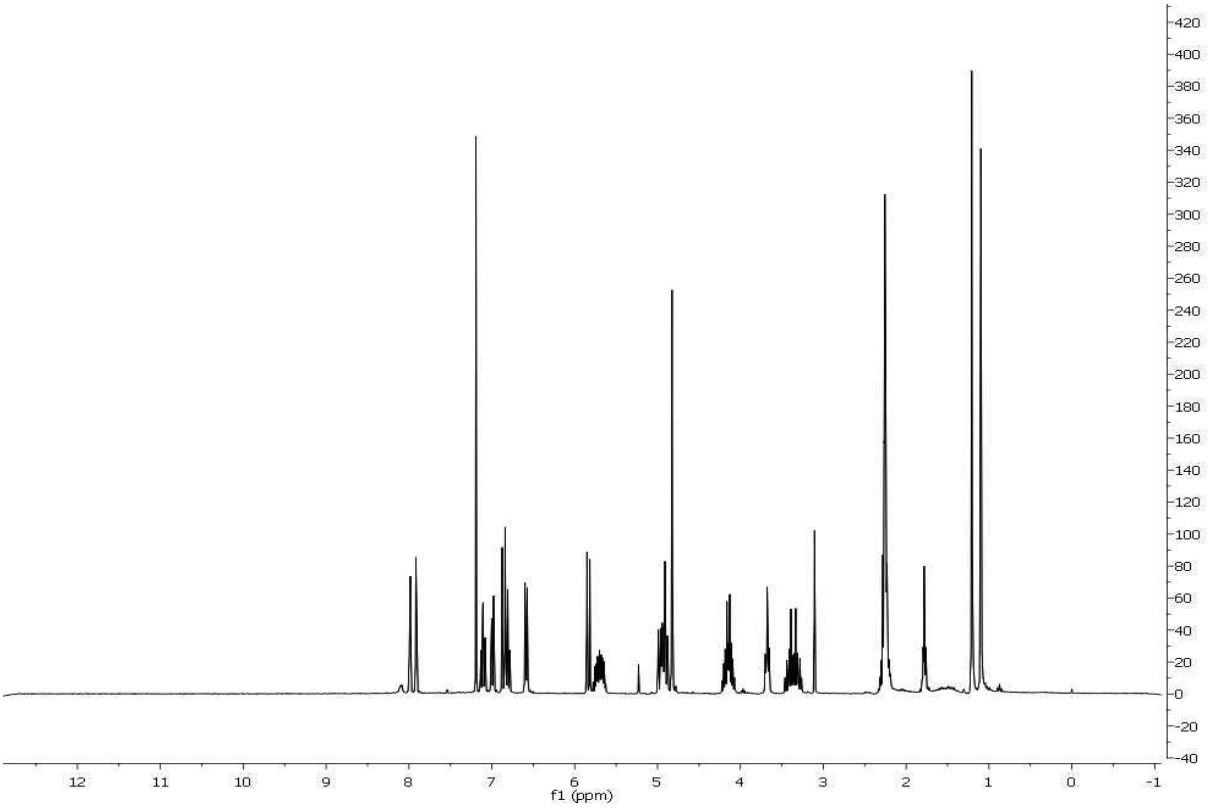

Figure S4.1 ^{1}H NMR spectrum of functionalized SP (solvent=$CDCl_3$).

4.4.3 3D printing of plastic molds with lattice structures

Acrylonitrile Butadiene Styrene (ABS) filaments were used for the melt material extrusion printing on Flashforge Dreamer 3D Printer. The printing parameters were as follows: Extruder temperature: 230 ^{o}C; Platform temperature: 105 ^{o}C; Base print speed: 60mm/s; Travel speed: 80 mm/s; Retraction length: 1.3 mm; Retraction speed: 30 mm/s; Fill density: 100%; Fill pattern: hexangon; Overlap perimeter: 15%.

4.4.4 Fabrication of SP-PDMS sheets

Spiropyran was added with P-60 base and curing agent together (mass ratio of base: curing agent= 20:1) and mechanically mixed thoroughly. The liquid PDMS prepolymer was then poured onto the 3D printed molds and degassed at 35 Torr for 30 min by using a vacuum chamber until no bubbles were visible. Samples were then cured at 60 ^{o}C for 30 min. The PDMS sheets were peeled from the mold and outgrowth was removed with a razor blade.

4.5 Reference

(1) Papaelias, M. P.; Roberts, C.; Davis, C. L. A Review on Non-Destructive Evaluation of Rails: State-of-the-Art and Future Development. *Proceedings of the Institution of Mechanical Engineers, Part F: Journal of Rail and Rapid Transit*. **2008**, *222*(4), 367-384**.**

(2) Pan, B.; Qian, K.; Xie, H.; Asundi, A. Two-Dimensional Digital Image Correlation for in-Plane Displacement and Strain Measurement: A Review. *Meas. Sci. Technol.* **2009**, *20*(6), 062001.

(3) Qiu, Z.; Zhao, W.; Cao, M.; Wang, Y.; Lam, J. W. Y.; Zhang, Z.; Chen, X.; Tang, B. Z. Dynamic Visualization of Stress/Strain Distribution and Fatigue Crack Propagation by an Organic Mechanoresponsive AIE Luminogen. *Adv. Mater.* **2018**, *30*(44), 1803924.

(4) Gossweiler, G. R.; Hewage, G. B.; Soriano, G.; Wang, Q.; Welshofer, G. W.; Zhao, X.; Craig, S. L. Mechanochemical Activation of Covalent Bonds in Polymers with Full and Repeatable Macroscopic Shape Recovery. *ACS Macro Lett.* **2014**, *3* (3), 216–219.

Chapter 5. Geometry-Induced Early Onset of Mechanochemical Activation[3]

5.1 Introduction

Stimuli responsive polymers can alter their chemical or physical properties in response to particular environmental cues.[1,2] Exciting examples include polymeric materials that respond to stimuli such as light,[3,4] heat,[5,6] mechanical force,[7,8] electrical potential,[9,10] magnetic fields,[11,12] and/or pH[13]. A comparatively new class of stimuli-responsive behavior is found in polymer mechanochemistry-the ability to transduce mechanical force along the backbone of a polymer chain to produce a chemical response within the material.[7,8] Generally, the mechanically responsive units (typically referred to as "mechanophores") capable of relieving strain are placed within the polymer backbone.[7] Mechanophores have been developed to produce a wide range of chemical responses, including effects such as stiffening or strengthening of materials under stress,[14,15] production of self-healable or remendable materials,[16–18] small-molecule release,[19–22] rapid depolymerization,[23] catalyst activation,[18,24,25] electrical conductivity changes,[26] and mechanically induced luminescence and color change (mechanochromism).[27,28]

Polymer mechanochemistry is a rapidly growing field, but there are still some significant limitations that hinder its use in practical applications. For solid-state device, large deformations, often exceeding 100% strain, are typically necessary to achieve activation.[28,29] While large deformations are acceptable in some scenarios such as wearable electronics, reliable control over the onset of activation and total percent activation within mechanoresponsive materials is still

[3] Manuscript to be submitted.

difficult.[30] There is a large interest in developing, and much broader application base for, lower-strain and enhanced-activation mechanoresponsive materials. Much of the research to-date toward this goal has focused on a molecular-level, bottom-up approach to improvements in mechanophore activation.[31] To complement chemical-control of mechanochemical activation, we suggest that mesoscopic microstructural geometric tailoring could also be used to enhance mechanochemical activation.

Modulation of the geometric design, and thereby the micro- and macrostructure of a material, may also be a way to achieve lower global strains and enhanced activation. This could enable applications and responses not previously possible.[32,33] Simple changes in a material's microstructural geometry have been shown to enhance the weight specific stiffness- and toughness.[34] This has been shown primarily in lattice framework materials, in which stress and strain are delocalized within the framework through repeated periodic structures. Similarly, we suggest, that microstructural design can be used to locally amplify strain fields in a material, and thus alter the effective mechanophore activation onset for the lattice material. Color changing mechanophores, or mechanochromic materials, are particularly useful in that they enable researchers to visualize the mechanochemical transduction in real-time relative to inputted stress and strain.[35-38]

In this study, we show that through the incorporation of strain concentrating features within the context of a periodically structured material, onset of mechanical activation can be tailored to occur at a much earlier global strain in comparison with materials lacking judicious geometric design. We utilized a calibrated color imaging method to quantify activation within mechanochromic 3D printed and cast materials that leverage a spiropyran mechanophore. In addition, we have developed new numerical models, based on the finite element method (FEM),

which are capable of predicting the mechanochemical response in geometrically complex materials. The developed models are used to identify the underlying constitutive laws, quantify the mechanochemical activation throughout a material, and provide preliminary guidelines for numerical modeling and design optimization of mechanochromic materials. We expect such models will enable the future engineering of mechanochemically activate structured materials through topology optimization.

Based on our preliminary design optimization solution suggestions, different geometric configurations were printed using additive manufacturing (AM) techniques. AM was used to make modifiable molds for bulk cast elastomer mechanochromic materials. By discretely quantifying the activation within these different materials, comparisons of mechanochemical activation in materials with different macroscopic properties were possible. The similar results found between these materials showed that these controlled geometries were a good way to induce onset of mechanophore activation at earlier strains. Our initial design optimization solutions also verified this early onset activation. Ultimately, these tests have given us a framework to be able to model and predict what mechanical activation would look like in future structures and are the first step to achieving structures with designed activation strains.

Mechanochemistry is a unique field of study in which mechanical stress and strain fields can dictate the presence and amount of chemical response within a material. We found this exciting as it means that alteration in the macroscopic geometry could be utilized to dictate chemical responses on the nanoscale level. In order to be able to visualize and quantify the effects of geometry on our structures, we chose to use a well-studied mechanochromic mechanophore, spiropyran.[28,29] Through this visualization of color change, we envisioned that we could

incorporate mechanochromic activation as a constitutive property in numerical modeling of these materials, just like stress and strain.

5.2 Results and discussion

We chose to quantify mechanochromic activation of spiropyran within 3D printed spiropyran-containing polycaprolactone (SP-PCL) and mold-cast polydimethylsiloxane (SP-PDMS) materials, as shown in Fig.5.1. While SP-PDMS materials have been studied well, quantifying the constitutive behavior of thermoplastic elastomers is still challenging due to their complicated response, such as sequential necking under large deformation.[38,39] In these materials, two isomeric configurations of merocyanine result in a high-energy blue coloration visible under tension, and a lower-energy purple coloration visible when relaxed after mechanical activation or when activated by UV irradiation.[29]

We used red-green-blue (RGB) image analysis to quantify the mechanochromic activation in our periodically microstructured materials in response to an applied strain.[38,40] For our chosen materials, we defined the range of activation via the difference between the blue and green color components, as described in Eq (1):

$$\mathrm{BG} = \frac{2(B-G)}{B+G}. \qquad (1)$$

The maximum BG intensity, given in Eq. (1), for an applied strain is obtained by averaging the 100 highest, greatest, largest (maximum implies a single one) BG values (pixels) in the measurement domain. The maximum BG intensity was then scaled by the respective intensities obtained for the images of the sample in the unloaded state, the UV activated unloaded state (corresponding to the maximum possible activation), and the maximum applied strain loaded and

relaxed states. A detailed description of image processing along with the MATLAB function is given in the SI.

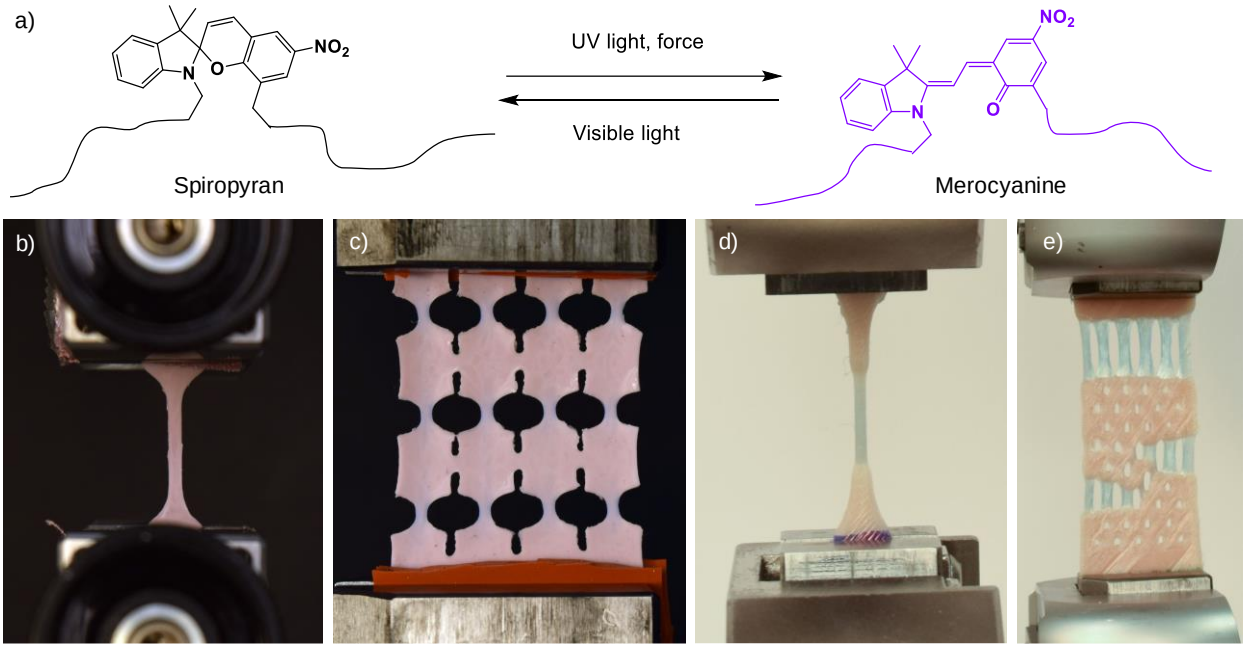

Figure 5.1 a) Generalized depiction of a spiropyran mechanophore activating to become a merocyanine dye b) Spiropyran-containing polydimethylsiloxane (SP-PDMS) dogbone after 50% global engineering strain c) SP-PDMS lattice after 50% global engineering strain d) Spiropyran-containing polycaprolactone (SP-PCL) dogbone at 50% global engineering strain e) SP-PCL lattice at 50% global engineering strain

We stretched the cast SP-PDMS "bulk" samples in the form of "dogbone" mechanical test specimens to 200% global strain (Fig.5.2) and characterized the activation profile as a function of uniaxial strain using the aforementioned mechanochromic activation characterization method. The comparison between the relaxed state from 200% global strain, the UV activated state, and the photobleached state was also shown in Fig.5.2. The activation response can be seen by the blue

line in Fig. 5.3c (up to 100% global strain). To enable earlier mechanochromic activation onset, in the context of uniaxial strain applied to a sample, we introduced strain concentrating elements. Our hypothesis was that arrays of microstructural elements that were as thin and short as possible will trigger early mechanochromic onset. As such, we cast a SP-PDMS sample in a 3D printed mold, as can be seen in Fig. 5.1c and Fig. 5.3a. Comparing Fig. 5.1b and Fig. 5.1c, we can see that for the same externally applied strain, the microstructured sample of Fig. 5.1c showed activation, whereas the bulk sample of Fig. 5.1b, did not. Quantifying the comparative activation over the tested strain range, we saw a sharp increase in activation of the microstructured sample over the bulk sample at ~35% strain. Quantifying onset of activation as values greater than 5% activation, we saw the microstructured sample reached onset approximately two times earlier than the bulk dogbone sample (Figure 5.3c). Similarly, at 70% strain, we saw experimental activations of approximately 23% and 5% for the lattice and dogbone, respectively (Figure 5.3c). To achieve spiropyran activation of 23% in a bulk dogbone sample, global strains over 135% are necessary. We noted that lattice designs have a lower volume ratio than a bulk sample of the same dimensions, however, and included local regions with virtually no strain. As a result, the average overall activation was generally lower, particularly at higher strains.

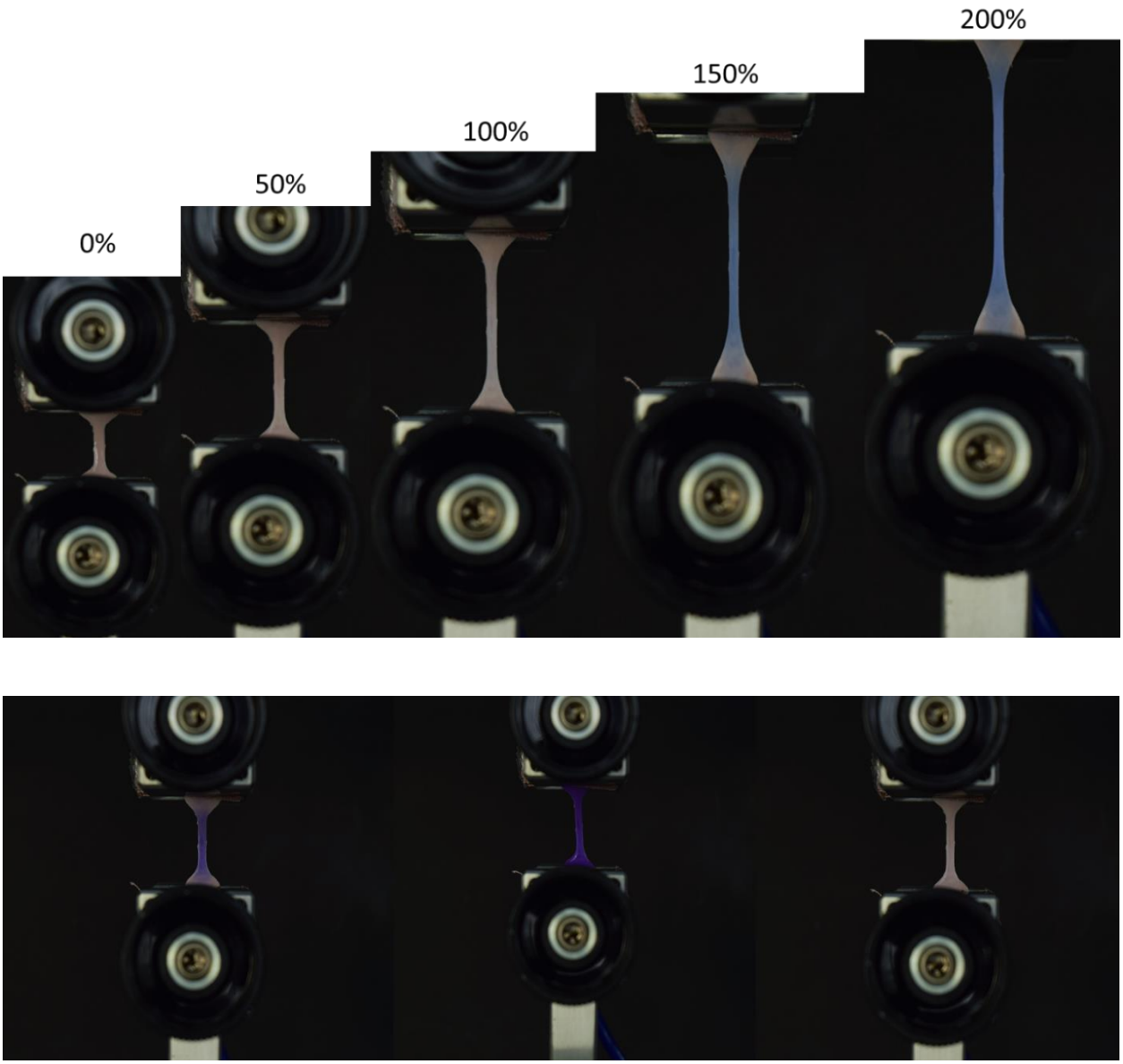

Figure 5.2 Top: uniaxial stretching of SP-PDMS "dogbone" up to 200% global strain. Bottom: left: relaxed state from 200% global strain, middle: UV activated state (100% activation), right: photo-bleached sample (0% activation).

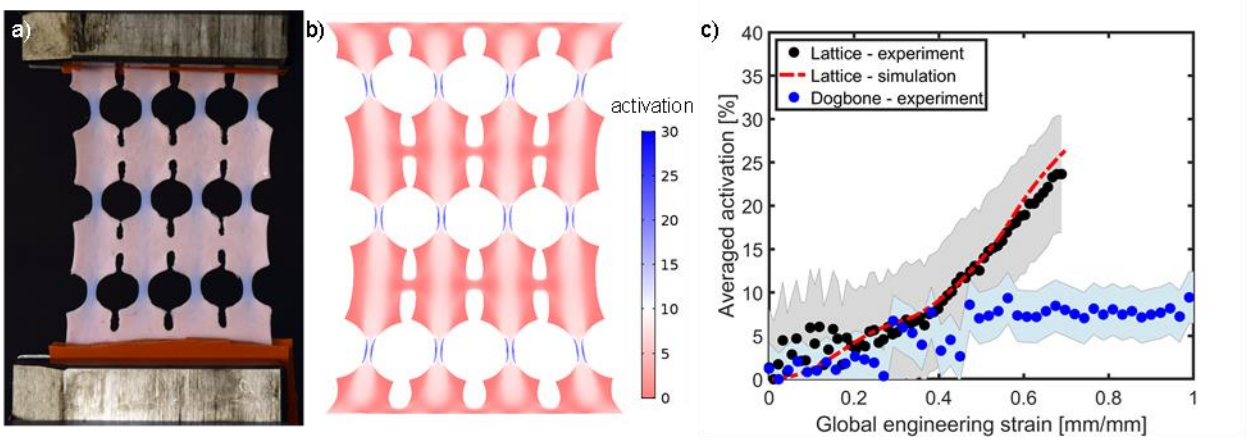

Figure 5.3 a) Experimental image of activation in SP-PDMS lattice at approximately 70% global engineering strain. b) Modelling of the same lattice at approximately 70% elongation. c) SP-PDMS effective activation vs. global strain (curves: experimental lattice, experimental dogbone, simulation lattice). Shaded area: error bar from experiment. b)

These differences were similar in 3D printed SP-PCL lattices, as can be seen in Fig. 5.1 and Fig. 5.4. An onset of 10% average maximum activation was visible in the lattice at approx. 25% strain experimentally, which is 9 times earlier than in a bulk dogbone sample. Based on the lattice simulation however, we do not achieve 10% activation in the lattice until 175% global strain, or 1.3 times earlier. One major difference observed between the SP-PCL and SP-PDMS samples was the SP-PCL samples shown sequential necking due to inelastic deformation (which corresponds to the onset of mechanochromic activation). This behavior can be observed in the step like behavior shown in Fig. 5.4c.

For future use in the design and response prediction of microstructured mechanochemically responsive materials, we developed numerical models based on FEM simulations. For the numerical modeling of SP-PDMS samples, a FEM model is developed using COMSOL Multiphysics considering geometric and material nonlinearities. Hyperelastic Mooney-Rivlin material model, calibrated with the experimental sample as shown in Figure S5.4, is used for

material nonlinearity.[38] For the numerical modeling of SP-PCL samples, finite strain elasto-plasticity is considered. The details on finite element elasto-plasticity are provided in SI. Two nonlinear curve fitting algorithms are developed to extract material properties from the experimentally measured stress-strain curves of the SP-PDMS and SP-PCL dogbone samples.

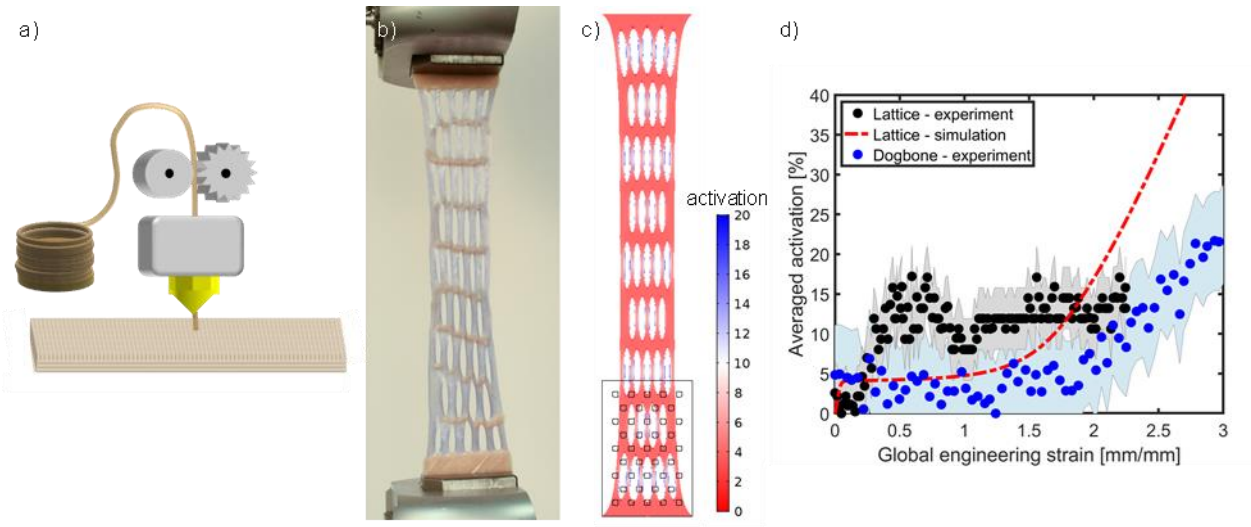

Figure 5.4 a) Schematic of melt material extrusion 3D printing of SP-PCL b) Experimental image of activation in SP-PCL lattice at 225% elongation c) Modeling of the same lattice at 225% global elongation d) SP-PCL Effective activation vs. global strain (curves: experimental lattice, experimental dogbone, simulation lattice)

After matching the mechanical response of the two polymers, we created functions to match the experimentally measured mechanochromic activation intensities, measured in the dogbone "bulk" samples. The activation profiles relative to calculated strains, either first principal strain (in the case of the SP-PCL) or first strain invariant (in the case of the SP-PDMS), are then used as constitutive properties of these two materials in the numerical simulation. For numerical modeling purposes, nonlinear curve fitting is used to develop a continuous and differential local

activation function. The fitted functions and parameters are detailed in the SI. To eliminate numerical mesh dependency and localization effects of the activation on the numerical model, the strain induced local activation is transformed to a smoothed nonlocal activation using the Helmholtz-type differential equation as follows:

$$\bar{A}_{\text{actv}} - \bar{c}_{\text{actv}} \nabla^2 \bar{A}_{\text{actv}} = A_{\text{actv}} \qquad (2)$$

where A¯_actv is the smoothed location activation and c¯_actv is the gradient parameter that controls the smoothness of the activation. Here, we set this parameter to 1.0e-8.

The results of numerical modeling for the SP-PDMS and SP-PCL are shown in Figures 5.3 and 5.4, respectively. Comparison between the experimentally measured and numerically predicted activation of both the bulk and microstructured lattice materials show good agreement. The SP-PCL model does not capture the experimentally observed sequential necking, however future incorporation of disorder could be a way to decrease the discrepancy and improve the numerical prediction.

5.3 Conclusions

In summary, we have shown that by changing the microstructural geometry of periodic mechanoresponsive polymeric materials, we can achieve activation at much lower overall strains. Furthermore, a new computational model was developed capable of predicting the activation response in complex mechanichemically responsive materials, which may be useful for future design optimization, including within 3D, additively manufactured structures. The tailored early onset activation may serve as a means to circumnavigate the existing issues with polymer mechanochemistry (e.g. large required strains) and broaden the utility of such materials to lower-strain engineering applications.

5.4 Experimental

5.4.1 Synthesis, fabrication, and mechanical testing procedures for mechanophore containing samples

Synthesis and fabrication of SP-PDMS samples

The procedures are described in Chapter 4.

Tensile testing for SP-PDMS samples

Tensile testing was conducted on an Instron 5585H load frame with a 50-N load cell. Sample elongations were done at a rate of 7 mm/min, and pictures were taken using a Nikon X camera and an intervalometer. SP-PDMS samples were taken to 70% or 200% elongation. After photographing the samples during elongation in which the blue higher-energy conformation of activated spiropyran-PDMS is visible, samples were kept in the load frame and tension was reduced to view the purple lower-energy conformation. A picture was taken of this relaxed sample as well.

Synthesis and filamentation of PCL-spiropyran-PCL (SP-PCL) samples

Synthesis and filamentation process have been described previously[29]. Filamentation was done through Functionalize, Inc. to produce 10 kg of blended 1:9 SP-PCL: PCL filament in 1 kg spools. These spools were used for 3D printing.

Melt Material Extrusion of SP-PCL

SP-PCL objects were printed using a Flashforge Dreamer with the following settings: Extruder temperature 120 °C, platform temperature 40 °C, base print speed 20 mm/s, travel speed 50 mm/s, minimum speed 5 mm/s, first layer maximum speed 20 mm/s, first layer maximum travel speed 20 mm/s, maximum path overlap 30%, fill density 100%, overlap perimeter 30%, and cooling fan

always on. Blue painter's tape was attached to the build platform prior to printing and wiped with ethanol prior to each print. Prints included ASTM D638 Type V dogbones, as well as square and triangular hole lattices chosen based on COMSOL Multiphysics.

Tensile testing for SP-PCL samples

Tensile testing was conducted on an Instron 5585H load frame with a 2-kN load cell. Sample elongations were done at a rate of 20 mm/min, and pictures were taken using a Nikon X camera and an intervalometer. SP-PCL samples were taken to 250% or 650% elongation. After photographing the samples during elongation in which the blue higher-energy conformation of activated spiropyran-PCL is visible, samples were kept in the load frame and tension was reduced to view the purple lower-energy conformation. A picture was taken of this relaxed sample as well.

Lighting setup and Camera settings

A CameraTrax 24 Color Card was used for white balancing prior to testing, and a Photogenic Light Kit with a softbox was used to create a uniform lighting environment. For SP-PCL samples, a white matte foam poster was placed behind the samples to make the background uniform. For SP-PDMS samples, a black poster board was used. For tensile testing of dogbones, the lighting was kept the same throughout testing for each sample. The lighting setup was modified slightly for tensile testing of lattices to deal with glare from the objects under tension, after which the lighting was kept the same throughout testing. Nikon camera settings: Shutter speed 1/15, F 100, ISO 400, exposure 0, evaluative metering on, image size Raw + F, flash exposure off. The intervalometer was set with a 4 second delay, with pictures taken every 4 seconds.

Quantification of SP activation through tensile testing PCL dogbones

Immediately after elongation of the sample, it was relaxed while still in the grips of the load frame to its purple coloration. A picture of this sample was taken. The sample was left in visible light for 24 hours to induce closing of the spiropyran. The sample was then placed in the same lighting setup and grips, and an image of the reverted sample was taken. The elongated sample was then irradiated with UV from a broad-spectrum Mercury lamp for 5 min to achieve complete spiropyran activation. This UV activated sample was then placed back in the load frame grips, maintaining the same lighting conditions, and a picture was taken. Quantification and numerical analysis can be found below.

5.4.2 Process of image analysis

To extract activation from an experimental image, an image processing algorithm is developed. In this algorithm, the following main steps are performed on every individual experimental image, the UV activated and relaxed images:

1- Preprocessing: to speed-up the image processing time, eliminate noise, and enhance the accuracy, cropping on the original images is performed. The cropping eliminates the process of unnecessary borders/background and narrows the adaptive window that only focuses on the picture of the specimen, see for example Figure S5.1. The adaptive window ensures consideration of the entire parts of the specimen as the size changes;

2- Extracting color channels: to separate the color channels and perform image processing, the red, blue, and green channels are extracted from the cropped images;

3- Background check: to eliminate the background noises, a threshold on the background colors of individual images is applied. In this paper, we apply thresholds on the blue and green channels and identify background for every image;

4- Compute the difference between blue and green channels: the following equation is used to compute the difference between blue and green channels:

$$\mathrm{BG} = \frac{2(B-G)}{B+G}. \qquad (1)$$

For the background parts of the images, the difference is set to zero;

5- Extract the sorted maximum difference from step (4) and compute the user-defined averaged activation;

6- Scale the computed activation based on UV activated, relaxed, and final loading states as follows:

$$\%\ \text{scaled activation} = \frac{(\text{unscaled activation} - \text{min. activation})}{(\text{max. UV activation} - \text{min. activation})} \frac{(\text{max. relaxed activation} - \text{min. activation})}{(\text{final activation} - \text{min. activation})}, \qquad (2)$$

where:

unscaled activation: averaged activation extracted from each image

min. activation: minimum activation of all images

max. UV activation: averaged maximum activation for the UV activated image

max. relaxed activation: averaged maximum activation for the relaxed image

final activation: averaged activation for the final loading state

For more details, the readers are referred to the provided MATLAB function for image analysis "image_analysis_compute_activation.m".

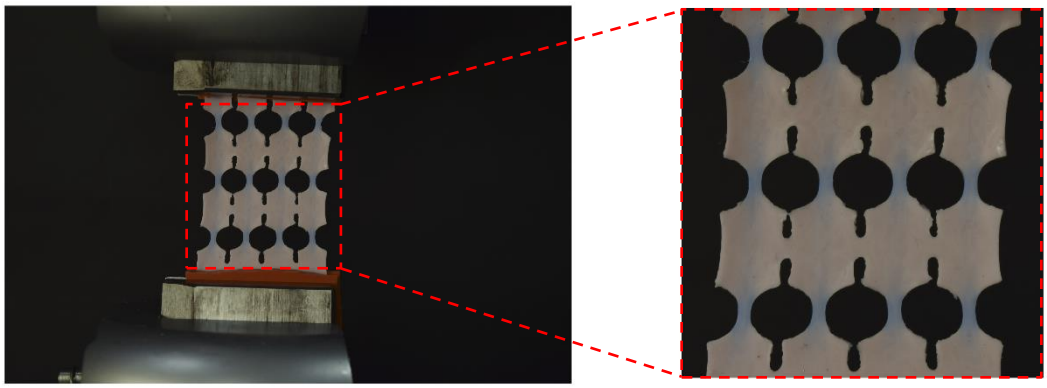

Figure S5.1 Schematic example of cropping of the original image in the image analysis

5.4.3 Activation profiles

Using the image processing algorithm, we extracted the activation profiles used in numerical modeling. To this end, the extracted activation profiles are considered as the local activation, i.e. A_{actv} in Eq. (4). Under uniaxial strain, we hypothesize that the local activation is the function of the first strain invariant and the first local principal strain, for the SP-PDMS samples and the SP-PCL samples, respectively. The curve fitting algorithm is developed to create smooth and differentiable activation profiles appropriate for the numerical modeling.

For the SP-PDMS samples, the extracted local activation from the image analysis is considered as a function of the first strain invariant using the following fitting function and as shown in Fig. S5.2:

$$A_{\text{actv}} = \alpha_1 \frac{\tanh(\beta_1\eta_1) + \tanh\big(\beta_1(I_1 - \eta_1)\big)}{\tanh(\beta_1\eta_1) + \tanh\big(\beta_1(I_1^{max} - \eta_1)\big)} + \alpha_2 \frac{\tanh(\beta_2\eta_2) + \tanh\big(\beta_2(I_1 - \eta_2)\big)}{\tanh(\beta_2\eta_2) + \tanh\big(\beta_2(I_1^{max} - \eta_2)\big)}$$

$$+ \alpha_3 \frac{\tanh(\beta_3\eta_3) + \tanh\big(\beta_3(I_1 - \eta_3)\big)}{\tanh(\beta_3\eta_3) + \tanh\big(\beta_3(I_1^{max} - \eta_3)\big)}, \qquad (3)$$

where I_1 is the first strain invariant. The other parameters extracted through the curve fitting are given as follows:

$$\alpha_1 = 1.4, \beta_1 = 5.0, \eta_1 = 0.0557, \alpha_2 = 6.0, \beta_2 = 5.3285, \eta_2 = 0.3, \alpha_3 = 27.6191, \beta_3 = 3.4783, \eta_3 = 1.4179, I_1^{max} = 10.0.$$

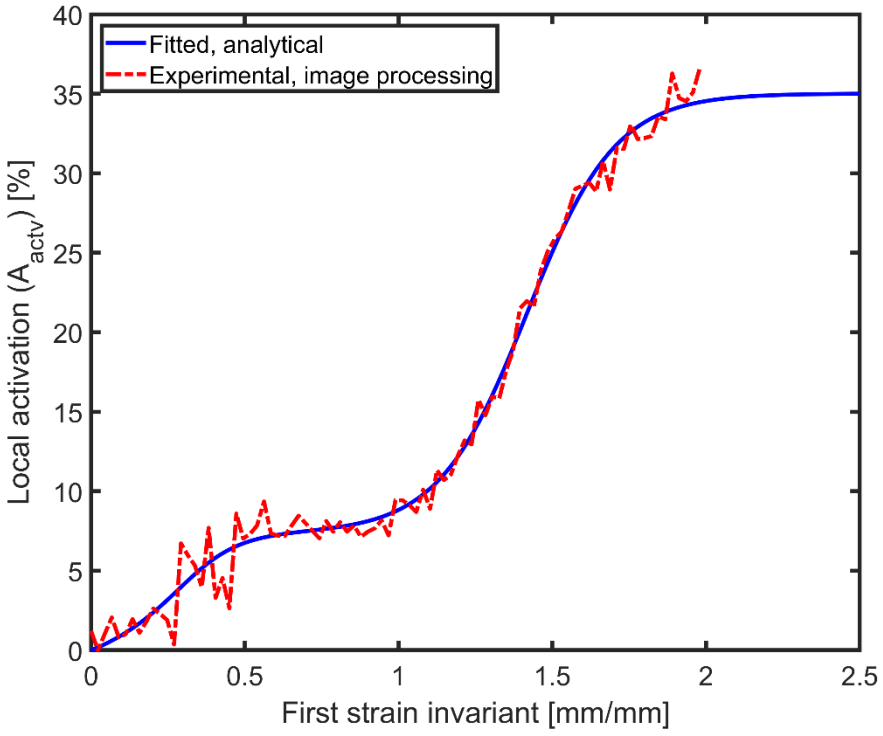

Figure S5.2 Local activation profile for the SP-PDMS samples

Similar to the SP-PDMS samples, we consider the following local activation for the SP-PCL samples, as a function of the first principal strain, see Fig. S5.3:

$$A_{\text{actv}} = \alpha_1 \frac{\tanh(\beta_1\eta_1) + \tanh\big(\beta_1(\epsilon_1 - \eta_1)\big)}{\tanh(\beta_1\eta_1) + \tanh\big(\beta_1(\epsilon_1^{max} - \eta_1)\big)} + \alpha_2 \frac{\tanh(\beta_2\eta_2) + \tanh\big(\beta_2(\epsilon_1 - \eta_2)\big)}{\tanh(\beta_2\eta_2) + \tanh\big(\beta_2(\epsilon_1^{max} - \eta_2)\big)} + \alpha_3 \frac{\tanh(\beta_3\eta_3) + \tanh\big(\beta_3(\epsilon_1 - \eta_3)\big)}{\tanh(\beta_3\eta_3) + \tanh\big(\beta_3(\epsilon_1^{max} - \eta_3)\big)} + \alpha_4 \frac{\tanh(\beta_4\eta_4) + \tanh\big(\beta_4(\epsilon_1 - \eta_4)\big)}{\tanh(\beta_4\eta_4) + \tanh\big(\beta_4(\epsilon_1^{max} - \eta_4)\big)}, \quad (4)$$

where $\epsilon_{max}$is the first principal strain. The other extracted parameters are given as follows:

$$\alpha_1 = 4.0, \beta_1 = 9.60, \eta_1 = 0.0, \alpha_2 = 32.0, \beta_2 = 0.1573, \eta_2 = 20.97, \alpha_3 = 12.4276, \beta_3 = 0.547, \eta_3 = 29.0802, \alpha_4 = 12.0, \beta_4 = 0.2768, \eta_4 = 38.8001, \epsilon_1^{max} = 60.0.$$

The extracted local activation is, then, transformed to the nonlocal activation as shown in Eq. (4).

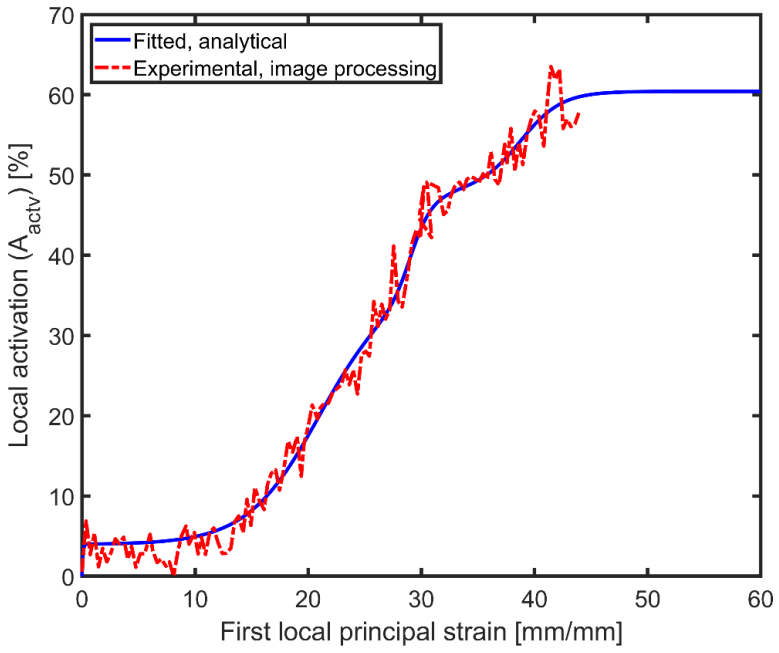

Figure S5.3 Local activation profile for the SP-PCL samples

5.4.4 Hyperelastic modeling of SP-PDMS

For numerical modeling of the SP-PDMS samples, finite strain hyperelasticity is considered. Nonlinear curving fitting algorithm is developed, considering different hyperelastic material models, to extract material parameters from the uniaxial stress-strain test (Fig. S5.4). Comparison of the stress-strain responses for different material models shows that the Mooney-Rivlin hyperelastic material model has the best fit. Under uniaxial loading conditions and Mooney-Rivlin material model, the uniaxial stress can be defined as follows:

$$P_{\text{uniaxial}} = 2(1-\lambda^{-3})\big(\lambda C_{10} + 2C_{20}\lambda(I_1-3) + C_{11}\lambda(I_2-3) + C_{01} + 2C_{02}(I_2-3) + C_{11}(I_1-3)\big), \quad (5)$$

where λ is the principal uniaxial stretch, I_1 is the first strain invariant, and $C_{10} = 93212.2\ Pa$, $C_{01} = 54825.7\ Pa$, $C_{20} = -8829.4\ Pa$, $C_{02} = 80464.9Pa$, and $C_{11} = 83149.6\ Pa$ are Mooney-Rivlin material parameters. The corresponding Young's modulus is $E = 2.8062\ MPa$, and the Poisson's ratio is $\nu = 0.49$. Although, some discrepancies arise at the end stage of the loading, which needs more investigation on the material models and sophisticated material models can be developed to address these discrepancies.

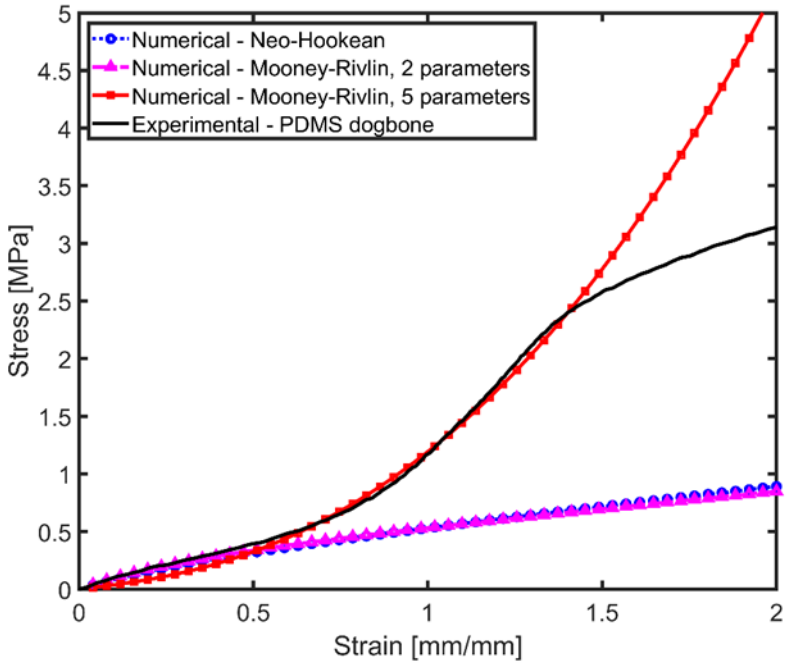

Figure S5.4 Stress-strain response of PDMS dogbone sample for different hyperelastic material models

5.4.5 Elasto-plasticity modeling of SP-PCL

For numerical modeling of the SP-PCL samples, finite strain elasto-plasticity is considered. To extract model and material properties from the uniaxial stress-strain curve, we first smooth the original stress-strain curve using nonlinear curve fitting. This ensures the elimination of the experimental noises and creates a smooth and differentiable stress-strain function used in

numerical modeling, as shown in Figure S5.6. It's important to note that we assume the proportional and elastic yield stress are the same. We also neglect the oscillation in the hardening portion of the experimental stress-strain curve.

For the finite strain elasto-plasticity model, it is important to calculate the effective plastic strain from the true stress-stress curve. To this end, we convert the engineering stress-strain curve to the true stress-strain curve using the following approximation:

$$\text{true strain} = \ln(1.0 + \text{engineering stress}),$$

$$\text{true stress} = (\text{engineering stress}) * \exp(\text{true strain}).$$

Next, the effective plastic strains can be calculated from the uniaxial true stress-strain curve as follows:

1- If the initial yield stress is not given, it can be calculated from the stress-strain curve at which the initial yield occurs. The corresponding effective plastic strain is called the initial plastic strain;
2- At every point on the true stress-strain curve, the trial plastic strain can be calculated as follows:

$$\text{trial plastic strain} = \text{total true strain} - \text{elastic strain}$$

where

$$\text{elastic strain} = \text{true stress}/(\text{Young's modulus}).$$

We note that as the stress increases, the recoverable elastic strain increases proportionally.

3- The calculated trial plastic strain can be adjusted to calculate the final effective plastic strain as follows:

effective plastic strain = trial plastic strain – (initial plastic strain – (initial yield strain)/(Young's modulus))

This adjustment is required to ensure that the effective plastic strain becomes zero when the total stress is equal to the initial yield stress.

4- Finally, for numerical simulation purposes, a nonlinear curve fitting is used to develop a continuous and differentiable function for the nonlinear effective plastic strain function as shown in Fig. S5.7.

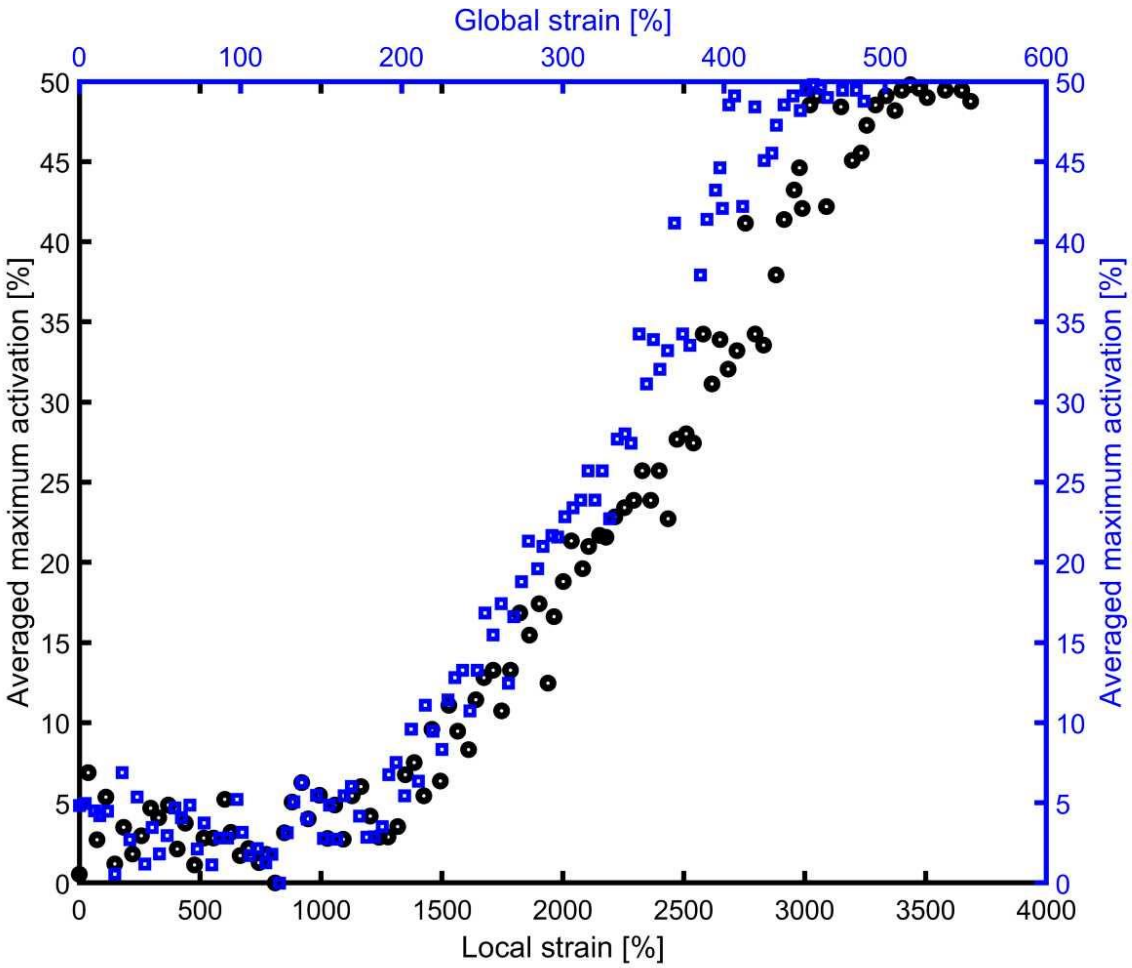

Figure S5.5 Comparison of local and global strain averaged maximum activation profiles.

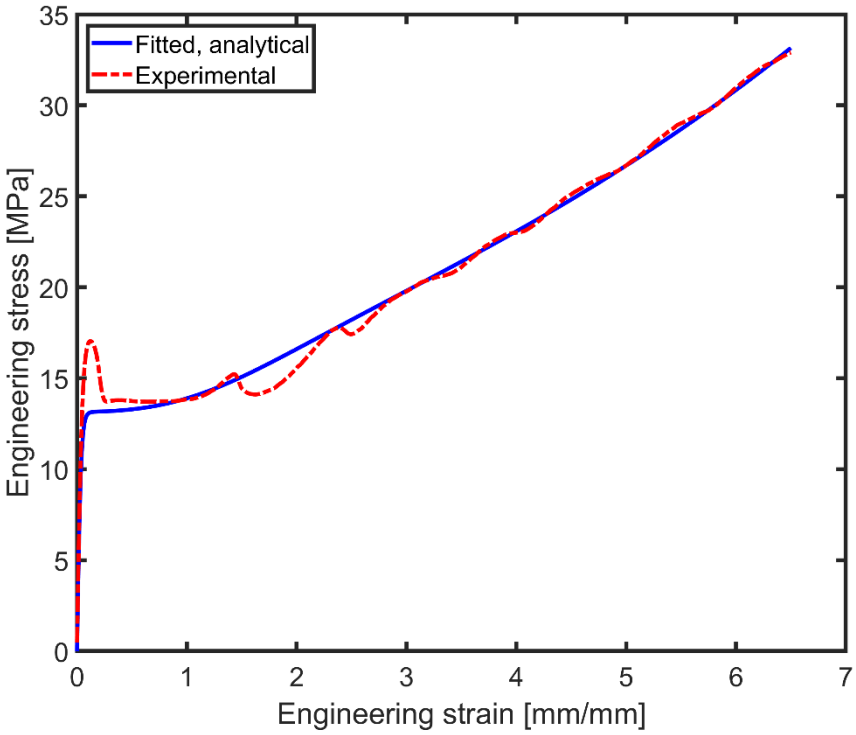

Figure S5.6 The original and fitted engineering stress-strain curve for the SP-PCL dogbone sample

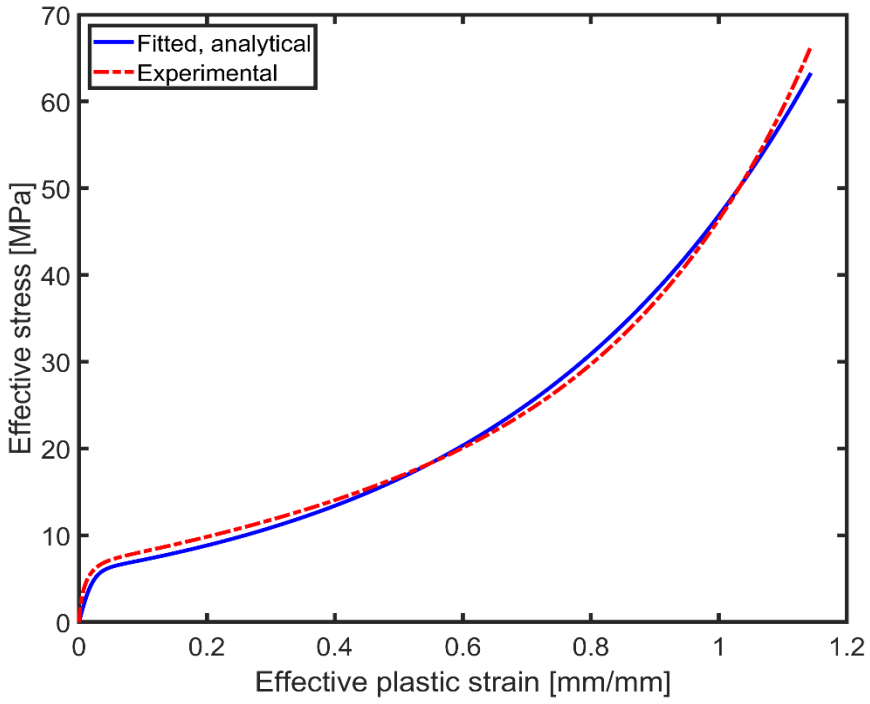

Figure S5.7 Extracted effective plastic strain function for the SP-PCL dogbone sample

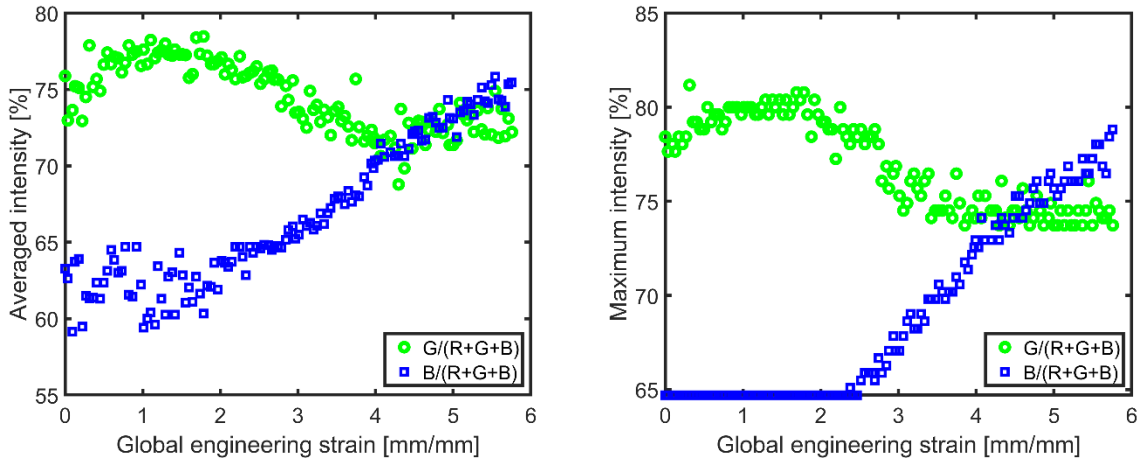

Figure S5.8 Left: Averaged blue and green intensities during elongation of SP-PCL dogbone. Right: Maximum blue and green intensities during elongation of SP-PCL dogbone.

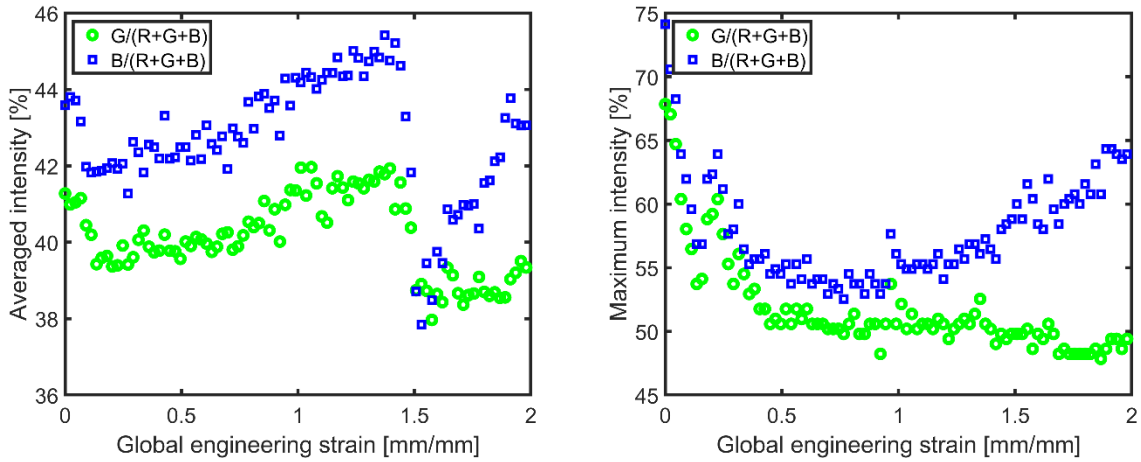

Figure S5.9 Left: Averaged blue and green intensities during elongation of SP-PDMS dogbone. Right: Maximum blue and green intensities during elongation of SP-PDMS dogbone.

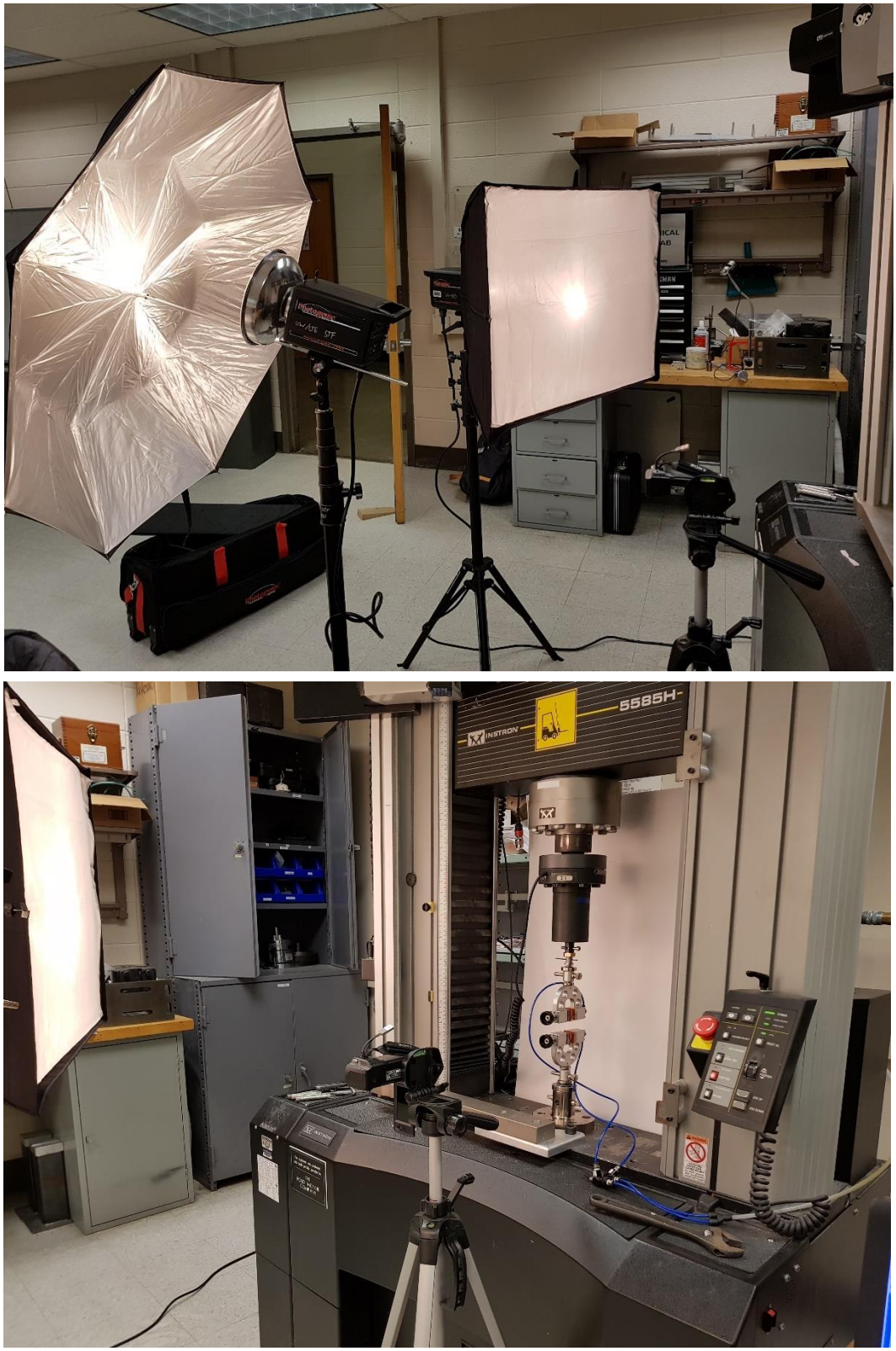

Figure S5.10 Lighting setup for capturing images of SP-PDMS and SP-PCL specimens

5.5 References

(1) Wei, M.; Gao, Y.; Li, X.; Serpe, M. J. Stimuli-Responsive Polymers and Their Applications. *Polymer Chemistry*. **2017**, *8*(1), 127-143**.**

(2) Aguilar, M. R.; Elvira, C.; Gallardo, A.; Vazquez, B.; Roman, J. S. Smart Polymers and Their Applications as Biomaterials. *Topics in Tissue Engineering. Expert issues e-books Biomaterials and tissue engineering group*. **2007**, *3*(6)**.**

(3) Irie, M. Properties and Applications of Photoresponsive Polymers. *Pure Appl. Chem.* **2007**, *62*(8), 1495-1502.

(4) Bertrand, O.; Gohy, J. F. Photo-Responsive Polymers: Synthesis and Applications. *Polymer Chemistry*. **2017**, *8*(1), 52-73**.**

(5) Roy, D.; Brooks, W. L. A.; Sumerlin, B. S. New Directions in Thermoresponsive Polymers. *Chem. Soc. Rev.* **2013**, *42*(17), 7214-7243.

(6) Kim, Y. J.; Matsunaga, Y. T. Thermo-Responsive Polymers and Their Application as Smart Biomaterials. *Journal of Materials Chemistry B*. **2017**, *5*(23), 4307-4321.

(7) Li, J.; Nagamani, C.; Moore, J. S. Polymer Mechanochemistry: From Destructive to Productive. *Acc. Chem. Res.* **2015**, *48*(8), 2181–2190.

(8) Brantley, J. N.; Wiggins, K. M.; Bielawski, C. W. Polymer Mechanochemistry: The Design and Study of Mechanophores. *Polym. Int.* **2013**, *62*(1), 2–12.

(9) Biggs, J.; Danielmeier, K.; Hitzbleck, J.; Krause, J.; Kridl, T.; Nowak, S.; Orselli, E.; Quan, X.; Schapeler, D.; Sutherland, W.; Wagner, J. Electroactive Polymers: Developments of and Perspectives for Dielectric Elastomers. *Angewandte Chemie - International Edition*. **2013**, *52*(36), 9409-9421**.**

(10) Pillay, V.; Tsai, T. S.; Choonara, Y. E.; Du Toit, L. C.; Kumar, P.; Modi, G.; Naidoo, D.; Tomar, L. K.; Tyagi, C.; Ndesendo, V. M. K. A Review of Integrating Electroactive Polymers as Responsive Systems for Specialized Drug Delivery Applications. *Journal of Biomedical Materials Research - Part A*. **2014**, *102*(6), 2039-2054**.**

(11) Ridi, F.; Bonini, M.; Baglioni, P. Magneto-Responsive Nanocomposites: Preparation and Integration of Magnetic Nanoparticles into Films, Capsules, and Gels. *Advances in Colloid and Interface Science*. **2014**, *207*, 3-13**.**

(12) Zhang, W. L.; Choi, H. J. Stimuli-Responsive Polymers and Colloids under Electric and Magnetic Fields. *Polymers*. **2014**, *6*(11), 2803-2818**.**

(13) Kocak, G.; Tuncer, C.; Bütün, V. pH-Responsive Polymers. *Polymer Chemistry*. **2017**, *8*(1), 144-176.

(14) Ramirez, A. L. B.; Kean, Z. S.; Orlicki, J. A.; Champhekar, M.; Elsakr, S. M.; Krause, W. E.; Craig, S. L. Mechanochemical Strengthening of a Synthetic Polymer in Response to Typically Destructive Shear Forces. *Nat. Chem.* **2013**, *5*(9), 757.

(15) Gordon, M. B.; Wang, S.; Knappe, G. A.; Wagner, N. J.; Epps, T. H.; Kloxin, C. J. Force-Induced Cleavage of a Labile Bond for Enhanced Mechanochemical Crosslinking. *Polym. Chem.* **2017**, *8*(42), 6485-6489.

(16) Klukovich, H. M.; Kean, Z. S.; Iacono, S. T.; Craig, S. L. Mechanically Induced Scission and Subsequent Thermal Remending of Perfluorocyclobutane Polymers. *J. Am. Chem. Soc.* **2011**, *133*(44), 17882–17888.

(17) Imato, K.; Kanehara, T.; Nojima, S.; Ohishi, T.; Higaki, Y.; Takahara, A.; Otsuka, H. Repeatable Mechanochemical Activation of Dynamic Covalent Bonds in Thermoplastic Elastomers. *Chem. Commun.* **2016**, *52*(69), 10482-10485.

(18) Jakobs, R. T. M.; Ma, S.; Sijbesma, R. P. Mechanocatalytic Polymerization and Cross-Linking in a Polymeric Matrix. *ACS Macro Lett.* **2013**, *2*(7), 613-616.

(19) Larsen, M. B.; Boydston, A. J. "Flex-Activated" Mechanophores: Using Polymer Mechanochemistry to Direct Bond Bending Activation. *J. Am. Chem. Soc.* **2013**, *135*(22), 8189-8192.

(20) Cao, B.; Boechler, N.; Boydston, A. J. Additive Manufacturing with a Flex Activated Mechanophore for Nondestructive Assessment of Mechanochemical Reactivity in Complex Object Geometries. *Polymer (Guildf).* **2018**, *152*, 4-8.

(21) Diesendruck, C. E.; Steinberg, B. D.; Sugai, N.; Silberstein, M. N.; Sottos, N. R.; White, S. R.; Braun, P. V.; Moore, J. S. Proton-Coupled Mechanochemical Transduction: A Mechanogenerated Acid. *J. Am. Chem. Soc.* **2012**, *134*(30), 12446-12449.

(22) Nagamani, C.; Liu, H.; Moore, J. S. Mechanogeneration of Acid from Oxime Sulfonates. *J. Am. Chem. Soc.* **2016**, *138*(8), 2540-2543.

(23) Diesendruck, C. E.; Peterson, G. I.; Kulik, H. J.; Kaitz, J. A.; Mar, B. D.; May, P. A.; White, S. R.; Martínez, T. J.; Boydston, A. J.; Moore, J. S. Mechanically Triggered Heterolytic Unzipping of a Low-Ceiling-Temperature Polymer. *Nat. Chem.* **2014**, *6*(7), 623.

(24) Piermattei, A.; Karthikeyan, S.; Sijbesma, R. P. Activating Catalysts with Mechanical Force. *Nat. Chem.* **2009**, *1*(2), 133.

(25) Michael, P.; Binder, W. H. A Mechanochemically Triggered "Click" Catalyst. *Angew. Chemie - Int. Ed.* **2015**, *54*(47), 13918-13922.

(26) Chen, Z.; Mercer, J. A. M.; Zhu, X.; Romaniuk, J. A. H.; Pfattner, R.; Cegelski, L.; Martinez, T. J.; Burns, N. Z.; Xia, Y. Mechanochemical Unzipping of Insulating Polyladderene to Semiconducting Polyacetylene. *Science.* **2017**, *357*(6350), 475-479.

(27) Chen, Y.; Sijbesma, R. P. Dioxetanes as Mechanoluminescent Probes in Thermoplastic Elastomers. *Macromolecules* **2014**, *47*(12), 3797-3805.

(28) Gossweiler, G. R.; Hewage, G. B.; Soriano, G.; Wang, Q.; Welshofer, G. W.; Zhao, X.; Craig, S. L. Mechanochemical Activation of Covalent Bonds in Polymers with Full and Repeatable Macroscopic Shape Recovery. *ACS Macro Lett.* **2014**, *3*(3), 216-219.

(29) Peterson, G. I.; Larsen, M. B.; Ganter, M. A.; Storti, D. W.; Boydston, A. J. 3D-Printed

Mechanochromic Materials. *ACS Appl. Mater. Interfaces* **2015**, *7*(1), 577-583.

(30) Barbee, M. H.; Mondal, K.; Deng, J. Z.; Bharambe, V.; Neumann, T. V.; Adams, J. J.; Boechler, N.; Dickey, M. D.; Craig, S. L. Mechanochromic Stretchable Electronics. *ACS Appl. Mater. Interfaces* **2018**, *10*(35), 29918-29924.

(31) Oka, H.; Imato, K.; Sato, T.; Ohishi, T.; Goseki, R.; Otsuka, H. Enhancing Mechanochemical Activation in the Bulk State by Designing Polymer Architectures. *ACS Macro Lett.* **2016**, *5*(10), 1124-1127.

(32) Boydston, A. J.; Cao, B.; Nelson, A.; Ono, R. J.; Saha, A.; Schwartz, J. J.; Thrasher, C. J. Additive Manufacturing with Stimuli-Responsive Materials. *Journal of Materials Chemistry A.* **2018**, *6*(42), 20621-20645**.**

(33) Shafranek, R. T.; Millik, S. C.; Smith, P. T.; Lee, C. U.; Boydston, A. J.; Nelson, A. Stimuli-Responsive Materials in Additive Manufacturing. *Progress in Polymer Science*. **2019.**

(34) Zheng, X.; Lee, H.; Weisgraber, T. H.; Shusteff, M.; DeOtte, J.; Duoss, E. B.; Kuntz, J. D.; Biener, M. M.; Ge, Q.; Jackson, J. A.; Kucheyev, S. O.; Fang, N. X.; Spadaccini, C. M. Ultralight, Ultrastiff Mechanical Metamaterials. *Science.* **2014**, *344*(6190), 1373-1377.

(35) Kingsbury, C. M.; May, P. A.; Davis, D. A.; White, S. R.; Moore, J. S.; Sottos, N. R. Shear Activation of Mechanophore-Crosslinked Polymers. *J. Mater. Chem.* **2011**, *21*(23), 8381-8388.

(36) Degen, C. M.; May, P. A.; Moore, J. S.; White, S. R.; Sottos, N. R. Time-Dependent Mechanochemical Response of SP-Cross-Linked PMMA. *Macromolecules* **2013**, *46*(22), 8917-8921.

(37) Davis, D. A.; Hamilton, A.; Yang, J.; Cremar, L. D.; Van Gough, D.; Potisek, S. L.; Ong, M. T.; Braun, P. V.; Martínez, T. J.; White, S. R.; Moore, J. S.; Sottos, N. R. Force-Induced Activation of Covalent Bonds in Mechanoresponsive Polymeric Materials. *Nature* **2009**, *459*(7243), 68.

(38) Beiermann, B. A.; Kramer, S. L. B.; May, P. A.; Moore, J. S.; White, S. R.; Sottos, N. R. The Effect of Polymer Chain Alignment and Relaxation on Force-Induced Chemical Reactions in an Elastomer. *Adv. Funct. Mater.* **2014**, *24*(11), 1529–1537.

(39) Cho, H.; Mayer, S.; Pöselt, E.; Susoff, M.; Veld, P. J.; Rutledge, G. C.; Boyce, M. C. Deformation Mechanisms of Thermoplastic Elastomers: Stress-Strain Behavior and Constitutive Modeling. *Polymer (Guildf).* **2017**, *128*, 87-99.

(40) Zhang, H.; Chen, Y.; Lin, Y.; Fang, X.; Xu, Y.; Ruan, Y.; Weng, W. Spiropyran as a Mechanochromic Probe in Dual Cross-Linked Elastomers. *Macromolecules* **2014**, *47*(19), 6783-6790.